Identification of Bearing Supports' Force Coefficients from Rotor Responses Due to Imbalances and Impact Loads

by

Oscar de Santiago

May 2002

TRC-RD-1-02, May 2002

IDENTIFICATION OF BEARING SUPPORTS' FORCE COEFFICIENTS FROM ROTOR RESPONSES DUE TO IMBALANCES AND IMPACT LOADS

EXECUTIVE SUMMARY

Experimental identification of fluid film bearing parameters is critical for adequate interpretation of rotating machinery performance and necessary to validate or calibrate predictions from often restrictive computational fluid film bearing models. Parameter identification in the field is also promising for condition monitoring and troubleshooting, and in the near future for self-adapting rotor-bearing control systems. Two procedures for bearing supports parameter identification with potential for in-situ implementation follow.

The analytical bases for the identification of bearing support coefficients derived from measurements of rotor responses to impact loads and due to calibrated imbalances in characteristic planes are thoroughly discussed. Subsequent implementation of the procedures to measurements performed in a (nearly) rigid massive rotor traversing two critical speeds forward force coefficients for a novel bearing support comprising a tilting pad bearing (*TPJB*) in series with an integral squeeze film damper (*SFD*). Compared to conventional bearing configurations, the novel support has the advantage of compactness, integral construction and lightweight; and most importantly, it offers increased rotordynamic stability, control of critical speed positioning, and reduced force transmissibility.

At a constant rotor speed, the first method requires impacts loads exerted along two lateral planes for identification of frequency-dependent force coefficients. Simulation numerical examples show the method is reliable with a reduced sensitivity to noise as the number of impacts increases (frequency averaging). In the experiments, an ad-hoc fixture delivers impacts to the rotor middle disk at speeds of 2,000 and 4,000 rpm, just below and above the system first critical speed (~3,000 rpm). The experimentally identified force coefficients are in close agreement with predicted coefficients for the series support *TPJB-SFD*. In particular, damping coefficients are best identified around the system first natural frequency (~ 52 Hz). Bearing stiffness are correctly identified in the low frequency range (below 30 Hz), but show a marked reduction at higher frequencies apparently due to inertial effects not accounted for in the model (test rig base resonance).

Measurements of rotor response to calibrated imbalances allow identification of speed-dependent force coefficients. The procedure requires a minimum of two different imbalance distributions for identification of force coefficients from the two bearing supports. The rotor responses show minimal cross-coupling effects, as also predicted by the computational analysis. Presently, the identification procedure disregards cross-coupled force coefficients thereby reducing the effect of false cross-correlations that cause ill-conditioning of the identification matrix and pollute the end results. The procedure renders satisfactory force coefficients in the speed range between 1,500 and 3,500 rpm, enclosing the first critical speed. The identified direct force coefficients are in accordance with those derived from the impact load excitations.

The second method identifying bearing support parameters from imbalance response measurements is simpler since it does not rely on direct application (and measurement) of external forces or transmitted bearing reaction forces. However, its adequate implementation requires of accurate measurement of phase angles, which are difficult to assess if the amplitude of rotor response is not large enough (instrumentation and software constraints).

Dr. Luis San Andrés
Principal Investigator

TABLE OF CONTENTS

LIST OF TABLES

LIST OF FIGURES

Page

NOMENCLATURE

$\mathbf{C}$	Rotor-bearing system damping matrix
C	Bearing damping force coefficient (N-s/m)
c	Bearing element radial clearance (m)
D	Bearing element nominal diameter (m)
d	Distance of imbalance or impact plane to rotor CG (m)
$\mathbf{E}$	Transient rotor excitation vector
$\mathbf{F}$	Excitation vector from imbalance
F	Force (N)
f	Imbalance function ($f = mre^{-j\phi}$)
$\mathbf{G}$	Gyroscopic moments matrix
$\mathbf{H}$	System impedance matrix
I_T	Rotor total transverse moment of inertia (kg-m^2)
I_P	Rotor total polar inertia (kg-m^2)
j	$\sqrt{-1}$ Imaginary unit
$\mathbf{K}$	Rotor-bearing system stiffness matrix
K	Bearing stiffness force coefficient (N/m)
$\overline{K}$	Ratio of bearing to shaft stiffness (-)
K_s	Rotor shaft lateral stiffness (N/m)
L	Bearing span, $L = l_1 + l_2$ (m)
L_b, L_d	Bearing and damper elements axial length (m)
l	Distance of bearing location to rotor CG (m)
$\mathbf{M}$	System mass matrix
M	Total rotor mass (kg)
m	Imbalance mass (kg)
$\mathbf{P}$	Vector of system parameters
$\mathbf{q}$	Rotor response vector
$\mathbf{Q}$	Matrix of responses for parameter identification
R	Bearing element nominal radius (m)
r	Radius of disk where imbalance masses are attached (m)
r_p	Dimensionless bearing pad or lobe preload (-)
s	Location of displacement probes from rotor CG (m)
t	Time (s)
$\mathbf{V}$	Generic vibration vector
$\mathbf{X}$	Vector of displacements
(x,y)	Coordinates of rotor motion (m)
Z	Bearing impedance ($Z = (K - \omega^2 M) + j\omega C$)
$\overline{\mathbf{0}}$	Zero vector (1x4)
μ	Viscosity of lubricant (Pa-s)
Ω	Frequency of rotor speed (rad/s)
ω	Frequency of excitation (rad/s)
ω_n	System natural frequency (rad/s)
ξ	System damping ratio ($\xi = C/2m\omega_n$)

ϕ	Angular location of imbalance mass (rad)

Subindexes

1,2	Indicates bearing locations (i.e. drive and free ends)
A,B	Indicates linearly independent experiments
app	Refers to an apparent quantity (apparent mass)
dyn	Refers to a dynamic property
eq	Indicates an equivalent property
m	Indicates a measured magnitude
p1, p2	Indicates original measurements at locations of displacement sensors (s_1, s_2)
b	Refers to bearing dimension
d	Refers to damper dimension
p	Refers to bearing pad dimension

CHAPTER 1

INTRODUCTION

1.1 FOREWORD AND OBJECTIVES

Thin film fluid flow models for journal bearings and seals, as well as advanced computational techniques for rotor modeling, allow predictions of rotordynamic stability and imbalance response of rotating machinery. Often, observations of rotor vibration in real machines show marked discrepancies with theoretical predictions mainly due to inadequate assumptions used in the models. Journal bearings are particularly sensitive to small variations in geometry and operating conditions, thus often being the source of the differences between predictions and observations [1].

Journal bearings (stiffness and damping) force coefficients are important in rotor analysis since they largely determine the rotor dynamic response and stability. There have been many efforts to develop reliable techniques to accurately identify journal bearing coefficients under controlled experimental conditions for verification of the models. However, there is presently the need for proven identification techniques that allow assessing the validity of the predicted bearing force coefficients in their working environment.

Recently, the turbomachinery industry is using novel bearing configurations for control of rotor vibrations. In particular, the combination of tilting pad bearings (*TPJBs*) and squeeze film dampers (*SFDs*) is commonly applied due to its desirable capabilities of inherent stability and low force transmissibility. This bearing configuration requires validation of the steady state and dynamic performance for widespread application. Additionally, there is the need in some cases to verify the dynamic force coefficients of this bearing configuration in machines that are already operating in the field.

The objectives of this research are to forward useful procedures for in-situ bearing parameter identification and to provide the results of identification for a combined *TPJB-SFD* bearing support. The key feature of the proposed methods is the requirement of minimal external equipment, little or no changes to existing hardware, and the use of measuring instruments commonly found in the field for machine protection and monitoring.

Chapter 2 provides an account of past methodologies utilized for identification of parameters in journal bearings and squeeze film dampers. The discussion focuses in frequency domain formulations, highlighting their advantages and pointing out their limitations. Chapter 2 also describes the importance of novel bearing configurations for vibration control, in particular the combined series support composed of a squeeze film damper and a hydrodinamic film bearing. This support has been applied in several compressors and steam turbines for improved stability and imbalance response [2].

Widespread use of this support in turbomachinery requires of validation of predictive tools by means of experimental measurements of the bearing dynamic response and subsequent reliable parameter identification.

Chapter 3 describes an existing experimental facility for testing the series support incorporating squeeze film dampers of the integral type and flexure pivot tilting pad bearings [3]. This bearing combination has speed and frequency-dependent force coefficients due to the series impedance that results of the two lubricant films. Identification of frequency-dependent force coefficients is made using an ad-hoc fixture to deliver impact loads to the rotating shaft at a fixed rotor speed. Special experimental procedures include the development of a time domain-based digital filter for shaft runout subtraction and comparison to alternative frequency domain-based filters. A second test apparatus is also used to identify (speed-dependent) bearing coefficients of rigid (two lobed) fluid film bearings from measurements of the rotor response to calibrated imbalances. The proposed methods for bearing parameter identification are derived from appropriate models of the rotor-bearing system representing the available experimental facilities.

Chapter 4 introduces the first identification method based on impact excitations applied to the rotating shaft. The method is particularly applicable for bearings featuring frequency-dependent force coefficients, such as tilting pad bearings or supports with two fluid films operating in series. The chapter contains the analytical derivation of the method from the equations of conservation of linear and angular momentum, and establishes the experimental conditions that must be met for identification of frequency-dependent bearing parameters. A numerical study shows the robustness of the method to noise and error in the measurements. Finally, the chapter presents an experimental validation of the method by application to the transient response of a rigid rotor supported on series squeeze film dampers and tilting pad bearings. Discussion of results includes an analysis to determine the optimum amount of experiments (repetitions) required to estimate reliable values of bearing force coefficients.

Chapter 5 describes a method for identification of speed-dependent bearing force coefficients from measurements of the imbalance response in a rotor supported on fluid film bearings. The chapter presents the identification method, describes the conditions for parameter identification and forwards all major assumptions. Discussion of the experimental conditions for proper identification is important because it leads to simplifying assumptions that may often improve the results of the identification. This is particularly useful because the identification method derived from a full rigid rotor model supported on two (different) anisotropic bearings is very sensitive to noise, to errors in the measurements and to extraneous dynamic effects (for example, from support resonance or other mechanical elements not accounted for in the model).

The experimental validation includes the identification of the equivalent (speed-dependent) parameters for the combined squeeze-film damper and fluid film bearing support. The major simplifying assumption is that the bearings' crossed-coupled coefficients are negligible. This important observation is supported by the measurements

and identification presented in Chapter 4, and leads to a pair of systems of equations fully uncoupled. The second case presented for validation of the method includes measurements of the imbalance response of a rotor supported on identical (two lobe) fluid film bearings. The experimental rotor configuration simplifies the identification model because the two bearings carry the same static load and have identical nominal operating conditions. The experimental conditions allow estimation of a reduced number of bearing parameters from the dynamic rotor response using only one set of imbalance masses.

Chapter 6 summarizes the methods and results, and forwards conclusions and recommendations for continuation of the work. Appendix A lists the program utilized for data acquisition of the transient response of the rotor to impact excitations, and Appendix B shows the formulation for the equivalent impedance of two fluid films in series, resulting in frequency-dependent force coefficients.

CHAPTER 2

LITERATURE REVIEW ON BEARING PARAMETER IDENTIFICATION AND INTRODUCTION TO MODERN BEARING CONFIGURATIONS FOR CONTROL OF ROTOR VIBRATIONS

2.1 INTRODUCTION

The objectives of the present work are to forward useful procedures for in-situ bearing parameter identification and to provide results of force coefficients for a combined *FPJB-SFD* bearing support. The first part of this chapter presents a review of general techniques for bearing parameter identification, from simple static loading procedures for measurement of fluid film flexibility to more elaborated procedures including noise rejection. The following section details the advantages of the series *FPJB-SFD* bearing support, and states the need for experimental validation of current predictive tools. Finally, the last part outlines common force coefficient identification procedures for squeeze film dampers and tilting pad bearings used in the past, and discusses the quality of results obtained using each method. The discussion focuses on the applicability of the methods for implementation in the field.

2.2 BRIEF REVIEW OF PAST RELEVANT LITERATURE ON BEARING PARAMETER IDENTIFICATION METHODS

In general, bearing reaction forces applied on the rotor due to the shaft displacements about a static equilibrium position are modeled by:

$$\mathbf{F} = -\mathbf{K}\mathbf{X} - \mathbf{C}\dot{\mathbf{X}} - \mathbf{M}\ddot{\mathbf{X}} \tag{1}$$

Where **F** is the external force applied to the rotor, **X** is the vector of displacements (x,y), and **K**, **C** and **M** are the bearing stiffness, damping, and inertia matrices, respectively. The entries of these matrices are the rotordynamic force coefficients known as bearing parameters. In Equation (1), the dot over the variables denotes differentiation with respect to time. The rotordynamic force coefficients are defined as:

$$K_{ik} = -\frac{\partial F_i}{\partial x_k},\ C_{ik} = -\frac{\partial F_i}{\partial \dot{x}_k},\ M_{ik} = -\frac{\partial F_i}{\partial \dot{x}_k} \tag{2}$$

where $\{K, C, M\}_{ik=x,y}$ are the coefficients relating the bearing reaction forces in the i direction to the rotor displacements, velocities and accelerations in the k direction, respectively. F_i in Equation (2) is the force that the fluid film applies on the rotor (journal). Notice that a fluid film bearing develops forces acting in the orthogonal direction to the instantaneous displacement, velocity or acceleration. This so-called cross-

coupling effect is a characteristic of hydrodynamic fluid film bearings. If the cross-coupled stiffness coefficients have reversed signs, a follower force arises that tends to destabilize the rotor.

The general problem of bearing parameter identification requires measurements (or estimates) of the bearing force (excitation) and rotor displacements (response). For bearings operating at low excitation frequencies, inertia forces are not significant with respect to the elastic and viscous (damping) forces. Many squeeze film bearing dampers have a centering spring and do not develop accountable fluid film stiffness, in which case the number of variables for identification is reduced.

There are numerous methods advanced for bearing parameter identification. Kozin and Natke [4] divide the identification methods into two major groups according to the nature of the data used for identification: time domain and frequency domain methods. The authors present a comprehensive study on the advantages and limitations of each group. Time domain methods are usually based on the minimization of an error function integrated over a finite period of motion. These formulations often require the use of numerical schemes for solution of non-linear Equations, rendering in general slow procedures that might suffer from numerical instabilities, for example.

Recently, Diaz and San Andrés [5] forward a "filtered orbit method" for identification of squeeze film damper force coefficients. In this method, a time orbit is reconstructed from the measured synchronous (1X filtered) vibration signals. Damping forces are adjusted to best fit a predicted orbit to the experimental measurements. This method is promising for in-field applications since it uses data acquired with readily available instrumentation. The filtered orbit method can be seen as a combination of time and frequency domain techniques, since the filtering of synchronous amplitudes is performed in the frequency domain.

Bearing parameter identification methodologies in the frequency domain are generally faster, and thus preferred for identification of force coefficients. Many methods use frequency response functions and curve fitting procedures to experimental data in order to estimate the bearing parameters. Usually, curve fitting methods assume that the bearing parameters remain constant over a range of frequencies. This assumption is not justified for certain types of bearings, such as in tilting pad bearings for example.

Goodwin [6] reviews experimental techniques for identification of bearing impedances. Bearing impedances (Z_{ik}) are complex functions, whose real part represent the dynamic stiffness, and whose imaginary part is proportional to the damping coefficients, i.e.:

$$Z_{ik} = (K_{ik} - \omega^2 M_{ik}) + j(\omega C_{ik}) \tag{3}$$

(where $i,k = x,y$ and $j = \sqrt{-1}$). When the inertia forces induced by the fluid film are small, the real part of the bearing impedance is approximated by the stiffness coefficients (K_{ik}). Estimation of bearing impedances at several frequencies renders an over-

determined system of Equations to solve for the bearing parameters. Then, a least squares estimator provides identification of the parameters over the range of frequencies tested.

Bearing impedances have the advantage over flexibilities of being linear functions of the bearing parameters, and are thus used extensively for identification. For example, a simple case of the use of impedance functions for identification of stiffness coefficients is that in which a static load is applied to the test bearing [7]. In this case, the damping forces (proportional to the rotor center velocity) are zero, and measurement of bearing reaction forces to displacements in only one direction render the stiffness coefficients. This method requires simultaneous application of forces in two directions to maintain displacements in only one direction, but the use of influence coefficients (flexibilities in this case) allow identification with only one load applied in each direction. Static methods are relatively simple to carry out, but usually render large errors in the identified coefficients and, as indicated before, only allow for identification of stiffness coefficients.

Other excitation sources allow estimation of the bearing impedance functions using dynamic loading, such as harmonic forces, pseudo-random periodic excitation, rotor imbalance and transient impulse loads, among others. Burrows and Sahinkaya [8] demonstrate that frequency domain estimations reduce bias error as compared to time-domain methods because the frequency transformation naturally filters out high-frequency noise. On the other hand, discrete sampled data introduce other limitations that must be carefully assessed (sampling rate-related aliasing and leakage phenomenon, for example).

Morton [9] uses electromagnetic shakers to apply a sinusoidal excitation to a test journal bearing and measures receptance (displacement over load) frequency response functions from unidirectional loading. The receptance matrix entries correspond to the individual dynamic flexibility functions obtained from excitation to the bearing housing floating on a rigid shaft, first in one direction and then in an orthogonal direction. The inverse of the receptance matrix corresponds to the impedance matrix, from which bearing parameters are estimated from curve fitting of the real and imaginary parts of the impedance function. Identified parameters correlate well with predictions of the bearing force coefficients.

Parkins [10] utilizes sinusoidal excitations in two directions and applied to a floating test bearing on a rigid shaft. The magnitude of the applied forces and the phase angle between them are varied until the bearing orbital motion collapses along one direction of excitation (straight-line orbit). Then, the bearing stiffness and damping coefficients are readily estimated by measuring the instantaneous force (magnitude and phase) at the precise instant of time when the displacements (x, y) or velocities $(\dot{x}, \dot{y})$ of the bearing housing are exactly zero. In this manner, the inversion of the receptance matrix is avoided and the identification is simpler and with less error from the inversion operation. Brockwell et al. [11] use this method for identification of stiffness and damping force coefficients of a five-pad, tilting pad journal bearing, as discussed later.

The procedure outlined in [10] is simple in theory, yet its actual implementation is complicated due to the nature of the expensive experimental facility required (shakers and controllers), and the need to precisely determine the occurrence of the journal position and velocity of interest. Identification of bearing parameters usually shows large variations using this method due to the difficulty in obtaining accurate measurements of the instantaneous force. At times, the appearance of sudden (transitory) changes of short duration in the measured forces and displacements from unaccounted sources adds to the uncertainty of the identification results. In this case, averaging of forces and displacements is mandatory over a large amount of periodic motions, in order to reduce the scattering of the identified coefficients.

Although frequency domain methods reduce the influence of high frequency noise, it may occur that noise with frequency components in the range of interest introduce errors in the estimation of mass, stiffness and damping force coefficients. Fritzen [12] introduces the Instrumental Variable Filter (IVF) as a refinement to the least squares method and that reduces the bias error from the measurements of rotor response used in the identification process. Diaz and San Andrés [13] use the flexibility matrix as a weighing function to improve the minimization procedure in the neighborhood of the system resonance where the dynamic flexibilities are maximums. In this way, the regions in the frequency range containing resonance peaks of response have more weight on the fitted system parameters, improving the identification with the Instrumental Variable Filter.

Uncorrelated noise in the measurements of vibration with respect to the input force appears during identification of bearing and seal parameters operating in turbulent regime (high Reynolds numbers). The random noise caused by the turbulence in the flow has frequency components within the range of the parameter identification. Rouvas and Childs [14] demonstrate that if the bearing is excited with a pseudo-random periodic excitation of several frequencies, then, the cross power spectral density between the applied force and the noise from the turbulent flow is zero. Using the definition of the spectral densities, the Equations of motion can be solved for the bearing impedances, and then a standard least squares (LS) estimator or IVF may render the parameter identification. In this case, the authors use least squares fitting of the analytical impedances to the identified impedance functions. The identification method presented in [14] is useful when noise exists in the same frequency range as the test signals, eliminating the possibility of rejection through filtering. On the other hand, it requires vast instrumentation and a more elaborated signal processing procedure that includes generation of the pseudo-random signals and calculation of power spectral densities, among others.

One of the simplest excitation methods to generate an (apparent) excitation load is to apply calibrated imbalances to the rotating shaft, so that the centrifugal force excites the system. Woodcock and Holmes [15] present results of parameter identification of a fluid film bearing in a turborotor using imbalance response measurements. In this case, only four coefficients are determined from the Equations of motion due to the nature of the excitation forces being 90° out of phase at all times. Sahinkaya and Burrows [16] identify

bearing coefficients from imbalance responses in the time domain using minimization of a cost function integrated over a period of vibration. But, as before, only four coefficients are identified if a planar model is used for describing the motion of the rotor supported on the fluid film bearing. Goodwin [17] overcomes this shortcoming by using a complicated test rig that uses a second internal shaft to generate imbalances at frequencies independent from the rotor speed. In this case, excitations at two different frequencies render the required set of Equations for identification of all bearing parameters at a single speed. However, the test bearing must have frequency-independent force coefficients for this approach to render satisfactory results.

In general, the system of Equations of motion generated by imbalance excitations tend to be ill-conditioned, and most experimental identifications show considerable scatter of results [6]. However, despite the limitations, this method is appealing for in-situ identification of bearing parameters due to the minimal requirements of external excitation systems and easiness of implementation in the field.

In addition to the methods discussed above, transient loading of rotor-bearing systems (from impact loads, for example) represents yet another option for bearing parameter identification. This method has the advantage of exciting a broad range of frequencies in a single experiment, considerably reducing the experimental effort and identification time. Besides, repetition of the experiment is extremely simple, allowing for economical averaging and variability studies.

Robison et al.[18] use cross-spectral densities to minimize noise and to identify dynamic force coefficients of a squeeze film damper from transient excitations (impacts) applied to the bearing housing in a vertical test rig. The bearing housing is suspended by four steel rods that provide structural stiffness for centering of the damper within its clearance. In this case, damping and inertia force coefficients are identified from the impedance functions since the stiffness of the bars are known a-priori. Correlation with theoretical predictions of force coefficients is good for a large range of static eccentricities, up to 50% of the damper radial clearance.

Nordmann and Shollhorn [19] present a method for identification of eight bearing parameters of a symmetric rotor supported on identical bearings using impact excitations directly applied to the rotating shaft. As indicated before, the main advantage of this method is the simplified experimental effort by exciting a large range of frequencies at once. Nordmann and Shollhorn assume that the bearing parameters are constant over a frequency range and use curve fitting of the frequency response (mobility) function amplitudes determined from the Fourier transform of the measured displacements and force. The method renders excellent correlation with theoretical predictions in the range of Sommerfeld numbers tested (0.75 to 2.3) for cylindrical journal bearings.

Despite the good results obtained with the identification from impact response measurements, there is still an obvious limitation for field application of this method, namely the difficulty in accessing the rotor shaft while the machine is in operation. Several methods are devised to overcome this shortcoming, including the use of support

and casing excitations. However, this procedure requires an appropriate model of the support structure, therefore producing a more elaborated method.

Morton [20] applies a slowly incremental lateral load to a rotating turborotor shaft from outside the machine through a calibrated link that breaks under a predetermined load magnitude. When the link breaks, the rotor suffers a sudden acceleration that dies out with time. The transient dynamic load has a broad range of frequency components that excite the rotor, and the measurement of the response allows calculation of the bearing impedances for identification of stiffness and damping coefficients.

Actual rotating machinery often features journal bearings, which are different on each end of the rotor. Furthermore, most turbo rotors are not symmetrical, and the bearings on both ends usually support different static loads. In some extreme cases, as in overhung rotors, the ratio of carrying loads between the two bearings can be of up to two. In these cases, bearing coefficients largely differ between the drive and free ends (even in the case of identical bearings) of the rotor. Note that many methods follow from the equations of motion for a point mass (rigid) rotor. If methods are to be developed for in-situ identification of bearing coefficients (without means to measure the transmitted forces through the bearings), then it is necessary to expand the previously presented methods as to include the effect of rotor dynamics.

A major consequence of including the rotor dynamics in the equations of motion is that the inertia matrix must include additional terms for estimating the rotor inertia and gyroscopic moments at the bearing locations. An additional benefit of the expanded models is that identification of all 8 force coefficients for each one of the two supporting bearings is feasible at a single speed or frequency because of the increased number of independent Equations of motion. However, note that the complications due to more comprehensive rotor dynamics modeling is totally overcome if the bearing transmitted forces are directly measured, although this task requires additional instrumentation and bearing housing design modifications.

Lee and Hong [1] estimate speed-dependent synchronous bearing coefficients of two different bearings supporting a rigid rotor by separating the forward and backward whirl responses resultant of the gyroscopic moments. However, this procedure is not necessary since the measured vibration already contains the forward and backward whirl components, thus filtered synchronous vibration data is just suitable to be used, making the identification procedure very easy to implement from running machine data. Force coefficients from isotropic bearings will cause numerical singularities during the inversion of the response matrix. Thus, the procedure is not able to identify the force coefficients in this case.

Tieu and Qiu [21] also identify sixteen synchronous coefficients of two different bearings supporting a rigid rotor from two or more imbalance response measurements. The authors utilize unfiltered responses and forward a numerical procedure to minimize noise influence. The experimental results show good correlation with theoretical predictions of force coefficients for a cylindrical journal bearing. However, the method

can be easily modified to use filtered synchronous responses, and thus not be affected by high frequency noise introduced in the measurements, as described in Chapter 5.

The importance of the works by Lee and Hong [1] and Tieu and Qiu [21] is that identification of parameters of two different bearings at different axial locations has the potential for application as an in-situ method. These procedures pave the way for improved modeling of fluid film bearings, verification of predicted force coefficients, and ultimately real-time bearing parameters monitoring and troubleshooting.

2.3 NOVEL BEARING CONFIGURATIONS FOR ENHANCED VIBRATION CONTROL OF TURBOMACHINERY

Tilting pad journal bearings (*TPJBs*) are commonly used in turbo-compressors and other high-speed machinery due to their ability to suppress instabilities commonly found in other rigid fluid film bearing geometries. However, *TPJBs* are very sensitive to small variations in the geometry of the convergent clearance between the journal and the pads, say due to static or thermal deformations. *TPJBs* are also very sensitive to stacking of manufacturing tolerances and pivot wear and fretting, which can severely deteriorate their performance.

The Flexure Pivot tilting pad bearing design (*FPJB*) alleviates most drawbacks of *TPJBs* associated with tolerance stacking and pivot wear because the pivot is integrally machined with the bearing outer ring. The pivot consists of a cantilevered thin beam (web) attaching the bearing pad with the outer ring and manufactured with the Electro-Discharge Machining (*EDM*) process. De Choudhury et al. [22] present an early application of *FPJBs* to a high speed centrifugal compressor. Comparisons with similar sized conventional *TPJBs* show that the *FPJB* gives a reduced temperature raise and power loss. Also, the rotor bearing system remains stable for the entire speed range of operation. Several geometric factors affect the performance of *FPJBs*, namely pad circumferential position with respect to the load, pad preload and pivot offset, among others. Zeidan and Paquette [23] discuss the effects of these parameters on the performance of conventional *TPJBs* and *FPJBs*. *FPJBs* can provide a very wide range of stiffness and damping coefficients. For example, the pivot beam rotational stiffness modifies the direct bearing stiffness coefficients, thus becoming an additional factor to be accounted for in the design of *FPJBs*.

TPJBs exhibit large stiffness coefficients that often locate the critical speeds very close to the machine operating speed. In such cases, it is desirable to soften the support in order to move the critical speeds away from the operating speed. It is also necessary to provide an additional source of damping because the large values of stiffness in the *TPJB* prevent the damping forces from the lubricant film to effectively attenuate rotor vibrations and forces transmitted to the support structure. Operating the machine above the critical speed (resonance) allows for much lower transmissibility and requires small amounts of damping for adequate vibration control at the operating speed. Safe passage through the critical speeds, however, demands adequate damping forces from the bearing

supports. Zeidan [2] incorporates squeeze film dampers (*SFDs*) in series with *FPJBs* to stabilize marginally stable rotors operating on *TPJBs*. Squeeze film dampers provide the required amount of damping to cross the critical speed resonance, maintain rotor stability and keep low force transmissibility to the bearing housing.

A squeeze film damper (*SFD*) consists mainly of a cylindrical journal and an outer ring separated by a thin annular lubricant film. A ball or roller bearing typically connects the damper journal with the shaft, and a radial spring centers the journal within the outer ring and prevents it from rotation. The journal motion (whirling) caused by external forces applied to the rotor squeezes the lubricant that fills the clearance between the journal and the outer ring. The lubricant then develops hydrodynamic pressure that generates the damping forces. A number of geometry factors such as diameter, length and clearance, as well as operating conditions such as supply pressure, feeding and discharge mechanisms, among others, determine the performance of *SFDs* in real applications. All these factors must be properly addressed for successful application of the damper.

Most gas turbines for aerospace applications feature squeeze film dampers with a centering spring in the shape of a squirrel cage. This spring often requires up to four times the axial length of the hydrodynamic land itself and thus represents a costly solution for vibration control in terms of weight and space. Recently, the *EDM* process enables also the manufacturing of integral squeeze film dampers (*ISFDs*). In this case, the damper journal and the outer ring are machined of a single steel piece connected with thin S-shaped springs that substitute the old squirrel cage-type spring. The springs divide the hydrodynamic land into four arc segments. The spring webs can be manufactured at any desired stiffness value for control of critical speed location. Also, the clearance around the damper journal can be made uneven to compensate for static deflection of the springs once the damper takes the rotor weight. Additionally, the damper can be split for easiness of installation and retrofit. Zeidan [2] discusses successful applications of *ISFDs* in the petrochemical industry.

Several applications of the combined support *TPJB-SFD* are in use today. However, there is currently the need for experiments to provide design guidelines and to validate predictive tools. The Turbomachinery Laboratory at Texas A&M University has several instrumented test rigs available for study of the dynamic characteristics of novel bearing configurations. The experimental programs aim to characterize the steady state and dynamic properties of the new bearing designs and provide reliable databases for calibration of predictive tools.

2.4 COMMON PARAMETER IDENTIFICATION TECHNIQUES IN SQUEEZE FILM DAMPERS AND TILTING PAD BEARINGS.

Bearing parameter identification plays an important role for model validation, design development and troubleshooting of high-speed machinery [24], [25]. This section focuses on the methods most commonly employed for identification of force coefficients in squeeze film dampers and tilting pad bearings. It is important to notice that the

definition of the bearing reaction forces in Equation (1) is basically a useful representation of bearing forces linearized about a journal equilibrium position. Force coefficients from squeeze film dampers are not strictly rotordynamic force coefficients as defined by Equation (2). Hydrodynamic fluid film forces in the damper arise from the instantaneous position and velocity of the journal, and are proportional to the orbit size. However, damper forces can still be represented by force coefficients as used in Equation (1), so that the parameter identification procedures for journal bearings can be used all the same in this case.

Thomsen and Andersen [26] and Tonnessen [27] identify damper coefficients by direct measurement of damper reaction forces to calibrated imbalances. The experimental facility consists of a vertical test rig featuring a squeeze film damper supported by load cells measuring the reaction forces in one axial plane and in two directions. Direct damping coefficients are determined simply as the proportionality constant between the journal instantaneous velocity and the viscous force. This viscous force is estimated as the difference between the total measured reaction force and the estimated elastic force from the centering spring. This method of identification is very reliable because it directly measures the reaction force transmitted through the bearings but is difficult to implement in practice because the load cells must support the bearings.

San Andrés and Vance [28] present a test rig for measurements of the lubricant dynamic pressure in a squeeze film damper whose journal is constrained to describe centered circular orbits (CCOs). Integration of the pressure field around the damper journal renders radial and tangential forces from where damping coefficients are readily determined. This test rig is extensively used to study details of the fluid flow and lubricant inertia effects. Although the use of circular centered orbits allows the study of many damper parameters, CCOs are hardly seen in practice mainly due to support asymmetry. Thus, there is still the need of developing adequate identification procedures for dampers operating under real operating conditions.

As mentioned before, Robison et al. [18] use cross-spectral densities to minimize noise and to identify dynamic force coefficients of a squeeze film damper from impulse load excitations applied to the bearing housing in a vertical test rig. Rouvas and Childs [14] first use spectral densities to reduce noise from undesired excitation sources created by turbulent flow in hydrostatic bearings. With this advanced identification method, Robison et al. find that correlation of identified (inertia and damping) force coefficients with theoretical predictions is good for a large range of static eccentricities, up to 50% of the damper radial clearance.

San Andrés et al. [29] compare damping coefficients of a squeeze film damper instrumented in a small rotor kit operating with a bubbly mixture of oil and air. The experimental set-up allows applying external excitation loads on the flexibly supported damper housing. In one case, damping coefficients are estimated from measurements of the steady state response of the damper housing to unidirectional sinusoidal excitations applied with an electromagnetic shaker. In the second method, impact guns deliver a calibrated force impulse to the damper housing, and proximity probes measure its

transient response. In both cases damping coefficients are estimated as a function of the air volume content in the mixture at zero rotational speed. The identified bearing coefficients show different trends according to the excitation method employed, thus showing that the fluid forces developed in the film are motion dependent. The major shortcoming of the experimental set-up for in-situ applications is that it is difficult to access the damper housing because it is usually contained within a bearing housing (pedestal).

San Andrés and Lubell [30], and De Santiago et al. [3] estimate viscous damping coefficients from squeeze film dampers supporting a rigid rotor from measurements of the rotor response to calibrated imbalances. Damping coefficients are estimated at a single point corresponding to the first critical speed of a simplified 1 DOF system. The measurements reveal that damping coefficients increase with the rotor orbit size, but not as much as predicted by theory. Kudzal et al. [25] also utilize imbalance response measurements to estimate the logarithmic decrement and damping force coefficients of flexible rotors in turbo-compressors for petrochemical applications. Diaz and San Andrés [5] use experimental orbits to determine damping coefficients as a function of the rotor speed in a rigid rotor subjected to calibrated imbalance loads, as described in a previous section. The main advantage of these methods is that they allow direct use of field-measured vibration to determine the equivalent viscous damping from the bearing supports.

Parameter identification techniques for journal bearings are equally applicable for identification of parameters of tilting pad bearings. The main difference (in terms of dynamic properties) between tilting pad bearings and fixed-geometry (rigid) fluid film bearings is that *TPJBs* have frequency-dependent force coefficients. Thus, suitable techniques must allow for estimation of synchronous and asynchronous bearing parameters of *TPJBs*. This is important also for the case of the combined support *SFD-FPJB* presented earlier.

One of the most common test rigs for identification of bearing parameters is one in which a rigid shaft spins but is prevented from whirling by precision ball or roller bearings. The test bearing is installed at midspan and is free to whirl about the shaft center. Special mechanisms apply static loads in any direction desired. Dynamic loading comes from hydraulic or electromagnetic shakers attached to the test bearing outer shell in two orthogonal directions. This allows to conveniently vary the force field applied to the bearing, and to control the eccentricity of the response. Independent adjustment of the shaker frequency also allows studying the frequency dependence of bearing force coefficients.

Brockwell and Kleinbub [31] and Brockwell et al. [11] present experimentally identified synchronous bearing coefficients of a five pad *TPJB* using electromagnetic shakers inducing bearing motions along a single direction (line orbits). The measurements show that bearing stiffness can be overpredicted even if considering pad and pivot deformations which usually reduce the overall bearing stiffness. The source of the discrepancy in this case is the inadequate modeling of the pivot flexibility. A common

result in identification of *TPJB* force coefficients is that damping is largely overpredicted, the experimental identification yielding force coefficient magnitudes less than one half of the predicted values for heavily loaded bearings. In general, the experiments show that *TPJBs* are sensitive to small changes in geometry due to pivot flexibility and thermoelastic pad deformations, among others.

Someya [32] presents a summary of design curves validated by experimental identification of bearing coefficients in a group of experimental facilities, most of them very similar with two vibrators in two orthogonal directions for direct bearing housing excitation. Design curves are presented for *TPJBs* as well as for other (rigid wall) fluid film bearings of different geometry, and under different load and operating conditions. In general, *TPJBs* with larger dimensions and larger loads present larger differences with predictions than smaller bearings.

Ha and Yang [33] also utilize the same test rig configuration to study the dependence of force coefficients of a 5 pad tilting pad bearing on the frequency of excitation. The authors identify all 8 stiffness and damping coefficients from the test bearing. The results of the identification show that rotordynamic force coefficients are less frequency-dependent than predicted. Pettinato et al. [34] identify non-synchronous force coefficients of a highly preloaded, 3 lobe bearing using sinusoidal excitations applied in two directions. The experiments confirm also in this case that the force coefficients of rigid bearings are not in general a strong function of the excitation frequency.

The test rig configurations described above is appropriate for model validation, but falls short to simulate actual operating conditions. Recently, Pettinato and De Choudhury [35] utilize an imbalanced (horizontal) rotor supported on a tilting pad bearing in one of its ends to identify stiffness and damping coefficients in the main directions. The test rotor is idealized as a point mass rotor, and the stiffness coefficients are identified from static response measurements. Imbalance response measurements serve only to identify damping coefficients as a function of the rotor speed. The test results indicate that identified force coefficients correlate well with predictions from an elastohydrodynamic model that considers most of the *TPJBs* variables such as pad and pivot flexibility, etc.

This chapter reviews several experimental techniques currently available for identification of bearing parameters. The main difference among them is the type of excitation force applied to the test element. Some methods are more appealing for field application, namely harmonic excitations from imbalance as well as impact excitations. These methods are the easiest methods to implement and involving the least experimental effort. These procedures are also suited for identification of speed dependent and frequency dependent force coefficients, typical of the modern bearing designs for enhanced control of rotor vibration, such as the combined *SFD-FPJB* support.

Presently, the objectives are to develop and test methods for identification of the combined support *SFD-FPJB* and to demonstrate their potential for application in industry. The application of the identification methods is carried out in a test rig featuring a rigid rotor supported by a pair of *SFD-FPJBs*. The following chapter describes the

experimental facilities and experimental procedures for identification of bearings dynamic force coefficients.

CHAPTER 3

DESCRIPTION OF EXPERIMENTAL FACILITIES AND TEST PROCEDURES

3.1 INTRODUCTION

This section presents the test facilities and particular measurement procedures developed for testing novel bearing configurations and to experimentally verify the proposed methods for bearing parameter identification. The test rigs described are located in the Turbomachinery Laboratory of Texas A&M University.

Figure 1 shows a fully operational test rig for study of steady state and transient response of a three disk rigid rotor supported on squeeze film dampers and hydrodynamic bearings [36]. This rotor has the size and inertia properties similar to those found in small aircraft gas turbines, and is part of an important experimental facility that closely resembles actual dynamic operating conditions. Figure 1 includes the major dimensions and rotor characteristics.

Currently, the test rig features the novel bearing configuration consisting of a flexible pivot tilting pad journal bearing installed in series with a squeeze film damper of the integral type. The damper soft centering spring determines the location of the critical speeds while the squeeze film provides damping forces for vibration control. The tilting pad bearing allows operation of the test rotor with small viscous drag and enhances system stability, as compared to rigid fluid film bearings.

Figure 2 shows a second test rig recently installed in the laboratory[1], and allowing similar measurements of rotor response as the test rig described above. The rig features a lighter test rotor that allows for thick disks to be installed in different configurations. The test rig has a pair of identical two-lobe fluid film bearings supporting the rotor shaft and eddy current sensors for measurements of imbalance response at the bearing locations. The rotor disks have threaded holes for attachment of calibrated imbalance masses to generate the dynamic excitation. The small size of the test rig allows for quick ramping of rotor speed and minimal experimental preparation effort.

3.2 DESCRIPTION OF TEST RIG FOR IDENTIFICATION OF EQUIVALENT BEARING FORCE COEFFICIENTS

This section describes the experimental apparatus for parameter identification of the combined support tilting pad bearing in series with an integral squeeze film damper. As mentioned earlier, this support has many advantages over other types of bearings. It shows small cross coupling force coefficients for increased rotor stability, reduced stiffness for low force transmissibility and large tolerance to rotor imbalance. The

[1]The rig is a donation by the rotating equipment group at AMOCO Corp. and is gratefully acknowledged.

integral construction of both bearing elements considerably reduces the axial space required and allows much simpler assembly procedure. Figure 3 shows a schematic of the bearing support, and Table 1 presents its main dimensions and geometry characteristics. This bearing configuration has equivalent bearing coefficients that are a function of both the running speed and the frequency of excitation, and requires two different techniques for parameter identification. As described in a later section, identification of frequency-dependent coefficients is achieved by delivering impulse loads (impacts) to the rotor while it spins. On the other hand, imbalance response measurements allow identification of speed-dependent, synchronous force coefficients.

The test damper consists of two (outer and inner) rings connected with four pairs of S-shaped structural springs machined with EDM process. A small clearance of 229 microns (~ 9 mils) separates the two rings and forms the damper land where the lubricant film creates the damping forces. The damper land is thus sectioned by the springs into four pads with an arc extent of 52°. Lubricant enters the film lands through four radial holes (1.6 mm in diameter) located around the damper outer ring, and a groove machined on the outer face of the ring forms a plenum for lubricant supply once the damper seats in its housing.

The damper inner ring (also called damper journal) accommodates the tilting pad bearing and provides a lateral orifice for independent bearing lubricant supply. An inner groove machined on the damper inner ring also forms a plenum from where the lubricant enters the bearing radially at locations between the pads. The test bearing has four pads (70° in extent) flexibly attached to an outer ring through integrally machined thin elastic beams (pivots). The bearing material is steel with a soft material liner (babbitt) in the pad inner surface. During the current experiments, the rotor weight (load) is directed between pads to minimize cross-coupled forces [37].

The test rig used is the same experimental facility described in [36] for earlier experiments on the imbalance response of the combined *ISFD-FPJB* support. The rig consists of a three disk rigid rotor supported on a pair of identical bearings housed in bearing pedestals resting on a steel plate. This plate is attached to a concrete table isolated from the laboratory floor by a bottom steel plate and elastomeric material. Figure 1 depicts the test rig and Figure 4 shows details of the test rotor and main dimensions. Table 2 presents a summary of the rotor inertia properties and geometry characteristics. The drive end and middle disks have a diameter of 279 mm (11 in) and the free end disk has a diameter of 229 mm (9 in). Each disk has 12 threaded holes where imbalance masses are attached at 114 mm (4.5 in) radius in the large disks, and 95.3 mm (3.75 in) radius in the small disk. Notice that imbalance masses are attached only for identification of speed-dependent, synchronous force coefficients.

A DC motor (7.5 kW, 10 HP) drives the test rotor up to a top speed of 4,000 rpm for the current experiments through a flexible coupling and an unidirectional drawn-cup clutch. Rotor speed is maintained manually through a variable-voltage power supply.

The bearing pedestals are split elements with a machined groove to accommodate the damper outer ring. Lubricant for the squeeze film dampers enters the pedestals from lubricant ports located at one side of the pedestals, and for the journal bearings through flexible connections attached to the damper outboard face. The pedestals have plexiglass transparent covers in the outboard face that allow visual inspection of the bearing elements, and custom-made hose seals on the inboard faces to prevent lubricant spill.

The lubrication system consists of a 150 lt main reservoir and gear pump with lines for independent supply to the damper and the journal bearing. Figure 2-12 shows a diagram of the lubrication system with valves and instrumentation for the experiments. An electric heater/cooler and automatic control keeps the lubricant to a predetermined temperature. The lubricant for the squeeze film dampers goes directly to the bearing pedestals and the lubricant to tilting pad bearings is directed through flexible hoses to the damper journal form where it goes to the bearing. The lubricant returns to the main reservoir through drain ducts machined in the bearing pedestals suctioned by an auxiliary return pump.

For identification of frequency dependent force coefficients, an ad-hoc fixture delivers impact loads to the rotor middle disk while the rotor spins. The impact force is transmitted through a tandem arrangement of (four) miniature ball bearings whose axis is aligned with the rotor main axis, as shown in Figure 5. A medium-hardness rubber hammer impacts an aluminum rod which slides in a bronze guide supported on a metallic structure attached to the test rig base plate. A coil spring returns the rod assembly to the initial position and an elastomeric material over-dampens the assembly motion. The aluminum rod transmits the load through a calibrated load cell that measures the total applied load to the rotor. The opposite end of the load cell features a special yoke mechanism upon which the miniature bearings are installed. In all experiments, special care is taken to ensure that the axis of the impact mechanism is always aligned in the corresponding radial direction (x,y) and perpendicular to the rotor axis of rotation. The resting position of the ball bearings is no more than 0.5 mm from the rotor disk surface to minimize inertia effects and undesirable signal noise arising from bouncing after the shock. After installation of the impact delivery fixture on the test rig, a detailed calibration of all mechanical components and the instrumentation followed.

The rig instrumentation consists of two pairs of eddy current transducers located in the inboard side of the bearing housings that measure the rotor vibration in the two orthogonal directions (x,y) resulting from the impact or calibrated imbalances. An analog conditioner removes the DC component from the sensor signals and amplifies rotor displacements for display in oscilloscopes and for the acquisition system. An optical tachometer provides a reference signal to the acquisition system for further signal filtering and to a digital display of rotor speed. A pair of piezoelectric load cells also provides time signals of the applied load to the rotor as described before. Table 3 summarizes the instrumentation sensors and the corresponding sensitivities. Additionally, K-type thermocouples and displays indicate the lubricant temperature in the tank and at the exits of the bearing elements. Turbine type flow meters measure the lubricant flow rate to the damper and bearing components.

3.3. DESCRIPTION OF TEST RIG FOR IDENTIFICATION OF SYNCHRONOUS FORCE COEFFICIENTS FROM IMBALANCE RESPONSE MEASUREMENTS

The second test rig used for identification of synchronous bearing coefficients from imbalance response measurements consists mainly of a two-disk steel rotor supported on a pair of two-lobe rigid journal bearings, as shown in Figure 2. Aluminum housings accommodate the test bearings and are bolted to a 50.4 mm (2 in) thick aluminum table. A 0.74 kW (1 HP), DC motor provides power to the shaft through a multiplier belt and pulley mechanism, and is able to drive the rotor up to 8,000 rpm. An electronic controller built-in to the rig allows for speed and torque control. A hinged plate covering the test rotor and bearing housings provides safety during the rig operation. The rig is bolted to a steel plate laying on padding material for isolation from the laboratory floor.

The test elements are identical, two-lobe, lightly preloaded, fluid film bearings and are split horizontally, as shown in Figure 6. The bearing back material is bronze and the liner material in contact with the shaft is soft babbitt metal. The free end bearing features a pair of thrust collars integral to the radial bearing. Close examination of the bearing surfaces reveals that the bearings have uneven wear around the inner diameter from previous experiments in which the bearings operated with pressurized air as the working fluid. Wear makes it difficult to precisely determine the original preload of the bearing lobes, and a small nominal value of 0.05 dimensionless preload is used in the calculations. Table 4 summarizes the bearing geometry and operating clearance. The bearings receive the lubricant from the housings through rectangular slots machined at the partition line of the bronze metal section. The slots end at the lobes on either side of the bearings where the fluid forms a recess for appropriate land lubricant supply.

The test rotor consists of a shaft, 25.4 mm (1.0 in) of main diameter and 640 mm (25.2 in) long, with a bearing span of 532 mm (20.95 in), as shown in Figure 7. The shaft has three annular inserts mounted along the shaft within the bearing span. Massive disks can be fitted onto the annular inserts rendering different rotor configurations. For the experiments presented here, the rotor features two disks attached to the shaft, 280 mm (11.0 in) apart from each other and centered in the bearing span. The shaft has rectified surfaces at the bearing locations and a notched groove at one end where a flexible coupling drives the shaft. Table 5 summarizes the rotor main dimensions and measured inertia properties.

The rotor disks are made of steel with a diameter of 165 mm (6.50 in). Each disk has an axial length of 31.9 mm (1.26 in) and weighs 3.86 kg (8.5 lbs). There are 24 equally spaced threaded holes in each disk for attachment of imbalance weights at a radius of 69.9 mm (2.75 in). The disks are attached to the shaft by means of clamping through-bolts and semi-circular lateral plates. The shaft (press-fitted) annular inserts provide support for the removable disks and locate them axially.

The bearing housings are split in the horizontal direction at the bearing centerline, and have a circumferential groove for radial oil delivery to the bearings. Split lateral covers made of aluminum provide an enclosure to avoid spills and incorporate grooves for custom stopper seals. The lubricant enters the bearings radially through slots in the partition across the horizontal direction, passes through the film lands; then falls to the bottom of the bearing housings to finally return to the main tank by gravity through the return ducts.

The lubrication system consists of a 25-lt (6.6 gal) oil tank, a submerged gear pump, pressure control valves and ducts. The oil tank is built integral with the test rig and is located at its lowest level. The gear pump delivers the lubricant (ISO VG 10 turbine oil) to the bearing housings at a supply pressure of 60 kPa (10 psig). Rigid pipelines conduct the lubricant to the bearing pedestals and a pressure gauge indicates the main inlet pressure. Lubricant temperature in the tank is measured with a handheld thermometer and recorded at the beginning and at the end of each test.

Measurements of the test rotor displacements are taken with two pairs of eddy current sensors located very close to the bearing locations. The bearing housings have threaded holes for installation of the sensors in two orthogonal directions, and located at 45° away from the vertical line, as shown in Figure 8. An additional eddy-current sensor aligned in the vertical direction and facing the rotor shaft (downwards) provides a reference signal for measurement of the phase angle and rotor speed.

Vibration signals from the eddy current sensors connect directly into a commercial data acquisition system for industrial machinery monitoring and diagnostic (Bently Nevada, Adre DAQ system). A personal computer hosts the acquisition system and runs the signal processing and analysis software. A two-channel dynamic signal analyzer displays the frequency content of the selected signals, and an analog oscilloscope displays the unfiltered rotor orbit in real time. The acquisition system displays the rotor speed in the computer monitor and records it for further processing.

3.4 EXPERIMENTAL PROCEDURES FOR IMPACT RESPONSE MEASUREMENTS

As mentioned earlier, the identification method developed for frequency-dependent force coefficients is based on measurements of the rotor-bearing system response to impulse load excitations. This section describes the special instrumentation and experimental procedures for data acquisition and processing of the recorded signals.

The data acquisition system consists of a Zonic 7000 series, high-speed acquisition unit interfaced with a Pentium II personal computer through an Ethernet board, as shown in Figure 9. The system configuration includes 6 channels for simultaneous acquisition of four displacement signals (two signals at each axial plane), one force signal and the tachometer reference signal. Appendix A lists the acquisition routine programmed for the experiments and including user-defined inputs for adequate file management. The program records six time varying signals and stores them in ASCII files. The main

advantage of the acquisition system is that it allows simultaneous sampling with a high time-resolution rate required for capturing the time history of the applied load. The program includes a pre-triggering function to ensure that the impact force signal is completely acquired within the time record. When the triggering condition is met (increasing voltage level at the load cell channel), the system begins acquisition of all six signals including the reference pick-up, which is essential to the filtering process, as explained below.

3.4.1 Development of a digital filter for shaft runout subtraction

Parameter identification of bearing coefficients at frequencies different from the running speed (synchronous) require the time signal of response to impact loads to be free from shaft runout. This section describes the development of the required filter in the time domain from experimental measurements of rotor response of the test rig featuring the series support *ISFD-FPJB*, but the procedure is applicable to any rotor and bearing configuration. The most challenging task when subtracting the shaft runout and remnant imbalance vibration signature is to adequately time the recorded signal with such signature. Recall that since the remnant rotor imbalance creates a synchronous excitation force, shaft runout and remnant imbalance response are indistinguishable from each other. However, this is not a limitation because the filter subtracts the two effects at once.

The filtering procedure is as follows. First, identify the experimental period of rotor speed using the tachometer signal. Figure 10 shows a typical tachometer signal. A programmed algorithm identifies the period of time elapsed between two consecutive pulses from the tachometer signal. Notice that depending on the rotor speed, the number of cycles in the time register varies and is usually not an entire number.

Once the experimental period of the rotor speed is identified and the number of samples per period is known, the next step is to create a runout vector for each channel (x_1, x_2, y_1, y_2). The acquisition system must have a pre-trigger time long enough so as to record a full period of pseudo-vibration (shaft runout) before the impact. Figures 11 and 12 show raw displacement signals as recorded by the data acquisition system for an impact in the horizontal (x) direction and the identified runout signals prior to the impact. Runout signatures are also identified at the end of the time record after the dynamic motion due to the impact has already died out.

Next, the vibration signatures are subtracted from the time register of the overall vibration point by point. The subtraction procedure runs forward in time for the vibration signatures identified at the beginning of the register, and backward in time for the signatures recorded at the end. This procedure continues until the subtractions meet at the middle of the register. The final time signal is smooth at the point of encounter at the center of the register because the rotor speed remains essentially constant and there are many points sampled in each rotor revolution (i.e. there is little error accumulated during the subtraction).

Figure 13 shows the filtered signals in the direction of the impact and in the orthogonal direction. The initial straight line is the result of the perfect subtraction (filtering) at the beginning of the register. Notice that the signal in the orthogonal direction of impact is very small and the filter does only a regular job due to the accumulation of error along the time register.

Figure 14 shows a comparison between the signals before and after the filtering. Notice the large levels of rotor vibration which include shaft runout and remnant imbalance (stationary vibration at the running speed).

The filtered signal is now suitable for transformation into the frequency domain using the discrete fast Fourier transform algorithm. Figure 15 shows the resultant spectra at each measurement location, along with the spectrum from the applied load in the interval between 0-200 Hz. Notice that this is only a small fraction of the total spectrum whose maximum frequency is 6.4 kHz. However, most of the frequencies of interest are only within a small fraction of this band (running speed: 2,000 cpm = 33.3 Hz). Note that the scales in the same direction of impact are different from the scales for the crossed-coupled direction. Notice that, as expected, the frequency spectra of the signals in the direction of impact (horizontal) is much smoother than the spectra in the vertical direction, which are only due to the cross-coupled forces (small in this case). Also, notice that the main peak occurs at the rotor natural frequencies (52-56 Hz). The running speed is also present as a small protuberance at 33 Hz. An averaging procedure in the frequency domain of consecutive impacts should smoothen the experimental spectra if the system behaves linearly.

3.4.2 Comparison of transient vibration signal filtering in time and frequency domains

This section shows a comparison between the filter presented in the section above and a filter implementation in the frequency domain. The basic idea for the new filter is to record a runout time signal of the same length as the original time register presented in the previous section, and then obtain the FFT of this signal. The runout time signal is generated from the identified period of rotor speed using the portion of the original time register prior to the impact. Figure 16 shows a typical time record (overall vibration at x_2 location) for an impact in the horizontal direction.

The impact begins at ~ 38 ms in the time register. This pre-trigger time is enough to capture at least one complete cycle of shaft runout. Figure 17 shows the identified period of remnant vibration (runout). For the frequency domain filter, the vibration signature is copied forward in time until completing a full time register (0.320 sec). Figure 18 shows the corresponding synchronized vibration trace from shaft runout. The Fourier transform of this signal can now be used for filtering by direct subtraction point by point in the frequency domain from the FFT of the signal shown in Figure 16 (original time record).

Figure 19 shows a comparison of the FFT of the vibration records for the original signal, the runout vibration signal and the filtered signal. Figure 20 shows the resultant

filtered frequency spectrum in a different scale to better appreciate the effect of the subtraction process. Notice the large synchronous component of the original signal at 33.3 Hz. Also, note that the filtered signal still shows a small peak at the running speed.

The filtered signal shown in Figure 20 coincides almost perfectly with the FFT of the filtered signal in the time domain. Figure 21 compares the complex (real and imaginary) spectra of the filtered signals in the time and frequency domains. There is virtually no difference in the range between 0 and 200 Hz. However, Figure 22 reveals only a small difference at the synchronous frequency between the amplitudes of the spectra for the two filter methods. The spectrum of the frequency-filtered signal shows a slightly smaller peak than the spectrum of the signal treated with the time-based filter.

Rotor vibration in directions orthogonal to the impact shows a nearly identical spectrum derived from both filters, as in the cases presented above. Noticeable differences occur only at frequencies higher than the range of interest (200 Hz).

The frequency-filtered data can be converted into time domain for comparison with the time-filtered time record. Figure 23 shows the recovered time signal for vibration in the direction of impact and in an orthogonal direction. Vibration signals in the direction of the impact show virtually no difference between the two methods. However, the signals in the direction orthogonal to the impact do show differences, in particular at the end of the record. This noise at the end of the record is largely of high-frequency content, and unlikely to be true vibration. In this case, the time trace compensated in the time domain shows much less disruption at the end of the record because of the way the subtraction is performed (runout subtracted from left to right and from right to left).

The observed differences are not as important for the parameter identification in the frequency domain because the useful frequency range for parameter identification is well below the observed noise frequencies. Alternatively, another method may record two different time traces of each channel, one containing the impact and a second one containing the shaft runout immediately before or after the impact. The same procedure described above would then be applied to the recorded signals. The main difficulty of this method is to synchronize the acquisition of the two time records in order to carry out the subtraction (complex numbers) in the frequency domain. Failure to synchronize the two signals renders erroneous results because the reference for the phase angle in the complex spectrum is not the same for the two traces. The presented methodology, on the other hand, requires only one time trace with a pre-trigger time long enough to capture a full period of shaft runout prior to the impact and then estimates the rest of the record, thus simplifying the experimental and programming effort.

3.5 EXPERIMENTAL PROCEDURES FOR IMBALANCE RESPONSE MEASUREMENTS

Imbalance response measurements are useful for identification of synchronous force coefficients, as described in Chapter 5. The first procedure prior to conduct imbalance

response measurements is rotor balancing. Rotor balancing is important because it provides a baseline for measurement of rotor response to calibrated imbalance masses. This is particularly important for sensitive systems because large orbital motions of the rotor at the bearings might compromise the estimation of linearized force coefficients. For the test rotors presented above, a standard influence coefficient method for two-plane balancing substantially reduces the original rotor synchronous response to satisfactory small levels of vibration.

Imbalance response tests consist of taking the rotor to a top speed and then coasting it down by shutting the power off from the driving motor. Measurements of rotor response are taken while the rotor coasts downs freely at a slow deceleration rate. The measured synchronous vibration vector (amplitude and phase, $\mathbf{V}_m$) at each speed is the sum of the remnant imbalance vector ($\mathbf{V}_r$), the dynamic rotor response to the calibrated imbalance ($\mathbf{V}$) and the shaft runout vector (also called slow-roll vector, $\mathbf{V}_s$). Thus, at each rotor speed (Ω):

$$\mathbf{V} = \mathbf{V}_m - \mathbf{V}_r - \mathbf{V}_s \qquad (4)$$

Equation (4) renders the desired dynamic response to use in the identification procedure. Shaft runout is represented as a constant vector ($\mathbf{V}_s$) that acts in all tests and for the entire speed range. If the remnant imbalance vector is not slow-roll compensated from shaft runout, (this is, if $\overline{\mathbf{V}}_r = \mathbf{V}_r + \mathbf{V}_s$) then the true dynamic response to calibrated imbalance is simply:

$$\mathbf{V} = \mathbf{V}_m - \overline{\mathbf{V}}_r \qquad (5)$$

Equation (5) does not require apriori knowledge of the slow roll vector, and is the form used in the compensated responses implemented for the identification of synchronous force coefficients.

CHAPTER 4

IDENTIFICATION OF FREQUENCY-DEPENDENT FORCE COEFFICIENTS

4.1 INTRODUCTION

As described in Chapter 2, a combined bearing support consisting of squeeze film dampers and tilting pad bearings (*SFD-TPJB*) shows frequency-dependent force coefficients resulting from its series impedance action. Incidentally, tilting pad bearings possess linearized rotordynamic force coefficients that are dependent upon the frequency of rotor vibration [38]. Thus, suitable procedures for parameter identification should render synchronous and non-synchronous bearing coefficients.

Non-synchronous rotordynamic coefficients are of paramount importance for rotor-bearing stability studies when asynchronous sources of excitation are known to be present in the system. Parsell et al. [39] demonstrate that asynchronous rotordynamic force coefficients of *TPJBs* remain nearly constant at any frequency ratio (frequency/running speed) for the case of heavily preloaded bearings. Unpreloaded bearings, however, present non-synchronous coefficients that can be substantially different from synchronous ones. The general trend shows that stiffness coefficients slightly decrease as the frequency of excitation increases. On the other hand, bearing damping coefficients slightly increase as the excitation frequency increases. Ha and Yang [33] present experimental force coefficients of a null-preload, five pad *TPJB* using steady sinusoidal excitations from hydraulic shakers. Ha and Yang find that the frequency of excitation has little effect on the rotordynamic force coefficients for the test bearing considered. Stiffness coefficients slightly decrease as the excitation frequency ratio increases while damping coefficients increase, according to the predictions in [39].

Non-synchronous bearing stiffness and damping coefficients at any rotor speed can also be identified from the rotor response to transient excitations, say due to impacts for example. This method has the advantage of exciting a whole range of frequencies in a single experiment, thus considerably shortening the experimentation effort as compared with steady state sinusoidal excitations. Additionally, impact excitations have the potential for in-situ identification of frequency-dependent bearing force coefficients.

4.2 IDENTIFICATION METHOD FOR FREQUENCY DEPENDENT FORCE COEFFICIENTS

The dynamics of the test rotor supported on series *ISFD-FPJB* described in Chapter 3 are satisfactorily modeled by a four-degree of freedom system where the cylindrical and conical modes of vibration are excited in the frequency range of interest (0-10,000 cpm). The recorded critical speeds of the rotor-bearing system [36] equal 2,900 cpm and 6,100 cpm, corresponding to cylindrical and conical rotor motions, respectively. The first rotor bending mode is estimated at 17,000 cpm from a transfer matrix model, well above the

maximum frequency of interest. Figure 24 shows the test rotor and coordinate system used in the analysis presented below.

The derivation of the identification procedure begins with the Equations of motion of the rotor-bearing system establishing the conservation of linear and angular momentum for a perfectly balanced rotor:

$$\mathbf{M}\ddot{\mathbf{q}}+\mathbf{C}\dot{\mathbf{q}}+\Omega\mathbf{G}\dot{\mathbf{q}}+\mathbf{K}\mathbf{q}=\mathbf{E}(t) \qquad (6)$$

where **M**, **C**, and **K** are the (4x4) inertia, damping and stiffness matrices and **G** is the gyroscopic moments matrix given below. **q** is a vector containing the lateral response of the rotor at the bearing locations (*1,2*) and in two orthogonal directions (*x, y*), Ω is the rotor speed and *t* is time. **E***(t)* is the transient rotor excitation (impact load) given by the generalized vector:

$$\mathbf{E}(t)=\begin{bmatrix}\sum_i F_{ix}\\ \sum_i d_i F_{ix}\\ \sum_i F_{iy}\\ \sum_i d_i F_{iy}\end{bmatrix}=\begin{bmatrix}F_{1x}+F_{2x}+\ldots\\ d_1F_{1x}+d_2F_{2x}+\ldots\\ F_{1y}+F_{2y}+\ldots\\ d_1F_{1y}+d_2F_{2y}+\ldots\end{bmatrix} \qquad (7)$$

where $F_{1x}(t),F_{2x},\ldots,F_{1y},F_{2y},\ldots$ are the excitation forces (impacts) applied at the *i*-th location along the rotor and at a distance d_i from the rotor center of mass. The simplest form of the excitation vector corresponds to the case in which only one impact is applied to the rotor in one direction. If the load is delivered at the center of gravity (i.e. $d_1 = d_2 = \ldots = 0$), then the excitation vector has only one row entry different from zero.

The mass (**M**), damping (**C**), stiffness (**K**) and gyroscopic (**G**) matrices are given by:

$$\mathbf{M}=\begin{bmatrix}Ml_2 & Ml_1 & 0 & 0\\ -I_T & I_T & 0 & 0\\ 0 & 0 & Ml_2 & Ml_1\\ 0 & 0 & I_T & -I_T\end{bmatrix},\quad \mathbf{C}=\begin{bmatrix}C_{xx1} & C_{xx2} & C_{xy1} & C_{xy2}\\ -C_{xx1}l_1 & C_{xx2}l_2 & -C_{xy1}l_1 & C_{xy2}l_2\\ C_{yx1} & C_{yx2} & C_{yy1} & C_{yy2}\\ C_{yx1}l_1 & -C_{yx2}l_2 & C_{yy1}l_1 & -C_{yy2}l_2\end{bmatrix} \qquad (8)$$

$$\mathbf{K}=\begin{bmatrix}K_{xx1} & K_{xx2} & K_{xy1} & K_{xy2}\\ -K_{xx1}l_1 & K_{xx2}l_2 & -K_{xy1}l_1 & K_{xy2}l_2\\ K_{yx1} & K_{yx2} & K_{yy1} & K_{yy2}\\ K_{yx1}l_1 & -K_{yx2}l_2 & K_{yy1}l_1 & -K_{yy2}l_2\end{bmatrix}\quad \mathbf{G}=\frac{I}{L}\begin{bmatrix}0 & 0 & 0 & 0\\ 0 & 0 & -I_P & I_P\\ 0 & 0 & 0 & 0\\ -I_P & I_P & 0 & 0\end{bmatrix}$$

where M is the rotor mass, I_T and I_P are the rotor transverse and polar inertia respectively, $l_{1,2}$ are the axial distances from the rotor c.g. to each bearing location, L is the bearing span. $\{K, C\}_{ik=x,y)1,2}$ are the bearing support damping and stiffness coefficients at the two bearing locations. Notice that the bearing stiffness and damping force coefficients are rotor speed and frequency dependent. Thus the matrices are dependent on these variables, i.e. $\mathbf{C}, \mathbf{K} = f(\Omega, \omega)$.

Finally, the response vector ($\mathbf{q}$) in Equation (6) is given as:

$$\mathbf{q} = [x_1, x_2, y_1, y_2]^T \tag{9}$$

Equation (9) is written in the frequency domain as

$$\mathbf{M}\ddot{\mathbf{q}}(\omega) + \mathbf{C}\dot{\mathbf{q}}(\omega) + \Omega\mathbf{G}\dot{\mathbf{q}}(\omega) + \mathbf{K}\mathbf{q}(\omega) = \mathbf{E}(\omega) \tag{10}$$

At any given frequency ω, the excitation vector can be written as $E(\omega) = E_o(\omega)e^{j\omega t}$, ($j = \sqrt{-1}$) and the response vector is then $\mathbf{q}(\omega) = \mathbf{q}_o e^{j\omega t}$. Thus, at a selected frequency ω, Equation (10) reduces to

$$-\omega^2\mathbf{M}\mathbf{q}_o + j\omega\Omega\mathbf{G}\mathbf{q}_o + j\omega\mathbf{C}\mathbf{q}_o + \mathbf{K}\mathbf{q}_o = \mathbf{E}_o \tag{11}$$

Do note that Equation (11) holds at any constant rotor speed Ω and at any particular frequency ω. At the rotor speed Ω, the steady state response is of the form $\mathbf{q} = \mathbf{q}_o e^{j\Omega t}$ with the components of $\mathbf{q}_o$ being complex numbers. This response at $\omega = \Omega$ defines the synchronous rotor response solely due to the impact excitation. In practice, it is difficult to subtract the remnant unbalance and synchronous noise components (due say to shaft eccentricity). An adequate data acquisition procedure must then filter out these components for adequate identification of synchronous force coefficients, as described in Chapter 3.

The bearing support reaction forces in the left hand side of Equation (11) can be expressed as the product of a (4x16) response matrix $\mathbf{Q}$, composed of linear combinations of the response vector ($\mathbf{q}_o$), and a vector of system (synchronous stiffness and damping) parameters $\mathbf{P}$ (16x1) as:

$$\mathbf{Q}\mathbf{P} = j\omega\mathbf{C}\mathbf{q}_o + \mathbf{K}\mathbf{q}_o \tag{12}$$

where:

$$\mathbf{Q}=\begin{bmatrix} \mathbf{q}_o^T & \bar{0} & j\mathbf{q}_o^T & \bar{0} \\ \mathbf{q}_o^T\mathbf{l} & \bar{0} & j\mathbf{q}_o^T\mathbf{l} & \bar{0} \\ \bar{0} & \mathbf{q}_o^T & \bar{0} & j\mathbf{q}_o^T \\ \bar{0} & -\mathbf{q}_o^T\mathbf{l} & \bar{0} & -j\mathbf{q}_o^T\mathbf{l} \end{bmatrix}_{4x16}, \quad \mathbf{l}=\begin{bmatrix} -l_1 & 0 & 0 & 0 \\ 0 & l_2 & 0 & 0 \\ 0 & 0 & -l_1 & 0 \\ 0 & 0 & 0 & l_2 \end{bmatrix}, \tag{13}$$

and

$$\begin{aligned} P=[&K_{xx1},K_{xx2},K_{xy1},K_{xy2},K_{yx1},K_{yx2},K_{yy1},K_{yy2},\\ &\omega C_{xx1},\omega C_{xx2},\omega C_{xy1},\omega C_{xy2},\omega C_{yx1},\omega C_{yx2},\omega C_{yy1},\omega C_{yy2}]^T{}_{16x1} \end{aligned} \tag{14}$$

The symbol $\bar{0}$ in Equation (13) represents a (1x4) zero vector. Equation (11) is rewritten as

$$Q\,P=E_o+[\omega^2 M-j\omega\Omega G]q_o \tag{15}$$

Separating real and imaginary parts, a system of 8 (real) algebraic linear Equations can be written to identify 16 (frequency dependent) rotordynamic force coefficients representing the two anisotropic support bearings. A second set (B) of excitations generating linearly independent responses then completes the required number of Equations to solve for the parameters vector **P**, i.e.

$$\mathbf{P}=\overline{\overline{\mathbf{Q}}}^{-1}\,\overline{\overline{\mathbf{E}}}_T\,; \tag{16}$$

where $\overline{\overline{\mathbf{Q}}}=\begin{bmatrix}\overline{\mathbf{Q}}_A\\ \overline{\mathbf{Q}}_B\end{bmatrix}$, $\overline{\mathbf{Q}}=\begin{bmatrix}Re[\mathbf{Q}]\\ Im[\mathbf{Q}]\end{bmatrix}$, $\overline{\overline{\mathbf{E}}}_T=\begin{bmatrix}\overline{\mathbf{E}}_{TA}\\ \overline{\mathbf{E}}_{TB}\end{bmatrix}$, $\overline{\mathbf{E}}_T=\begin{bmatrix}Re[\mathbf{E}_T]\\ Im[\mathbf{E}_T]\end{bmatrix}$ (17a)

and $$E_T=E_o+[\omega^2 M-j\omega\Omega G]q_o \tag{17b}$$

The conditions for the linear independence of the transient responses are easily inferred from the solution of Equation (11) for $\mathbf{q}_o$ as:

$$q_o=H^{-1}(\Omega,\omega)E_o \tag{18}$$

where $$H(\Omega,\omega)=-\omega^2 M+j\omega\Omega G+j\omega C+K \tag{19}$$

Two linearly independent excitations $\mathbf{E}_{oA}$ and $\mathbf{E}_{oB}$ thus generate linearly independent responses $\mathbf{q}_{oA}$ and $\mathbf{q}_{oB}$, respectively. The conditions for linearly independent excitations can be stated from the definition of the excitation vector in Equation (7), i.e.:

$$\mathbf{E}(t)=\begin{bmatrix}\sum_i F_{ix}\\ \sum_i d_i F_{ix}\\ \sum_i F_{iy}\\ \sum_i d_i F_{iy}\end{bmatrix}=\begin{bmatrix}F_{1x}+F_{2x}+\ldots\\ d_1F_{1x}+d_2F_{2x}+\ldots\\ F_{1y}+F_{2y}+\ldots\\ d_1F_{1y}+d_2F_{2y}+\ldots\end{bmatrix} \qquad (7)$$

Recall that $F_{i(x,y)}(t)$ represent impact loads applied in directions x,y on the rotor. Consider the case of a single impact applied at a time. The excitation in test B is linearly independent from the one applied in test A by simply shifting the excitation location along the rotor, even if the impact is applied in the same direction, i.e.

$$\mathbf{E}_A(t)=\begin{bmatrix}F_{1x}\\ d_1F_{1x}\\ 0\\ 0\end{bmatrix}, \quad \mathbf{E}_A(t)=\begin{bmatrix}F_{1x}\\ d_2F_{1x}\\ 0\\ 0\end{bmatrix} \qquad (20)$$

$\mathbf{E}_A$ is linearly independent from $\mathbf{E}_B$ if $d_1 \neq d_2$. Applying impacts first in one direction and then in an orthogonal direction also yields linearly independent excitation vectors, even if the axial location of the impacts is the same:

$$\mathbf{E}_A(t)=\begin{bmatrix}F_{1x}\\ d_1F_{1x}\\ 0\\ 0\end{bmatrix}, \quad \mathbf{E}_B(t)=\begin{bmatrix}0\\ 0\\ F_{1y}\\ d_1F_{1y}\end{bmatrix} \qquad (21)$$

Clearly, $\mathbf{E}_A$ is linearly independent from $\mathbf{E}_B$ in (21). Impact loads may be applied at the rotor center of gravity ($d_1 = 0$) or away from it. Applying the load at the rotor center of mass is obviously difficult to accomplish in a real machine, however note that this condition works at advantage for experimental identification in the laboratory.

Assuming the bearings coefficients to be identical on both sides of the rotor reduces the number of unknowns to eight, and the identification becomes possible with only one impact excitation[2]. In all cases, several consecutive impacts at the same rotor speed provide redundant data for error minimization.

Equation (16) is in a suitable form for programming the identification method. However, the use of bearing impedances ($Z = K + j\omega C$) considerably simplifies the programming effort and renders simpler identification Equations. Redefine the parameter vector $\mathbf{P}$ in complex form as:

[2] This condition assumes exactly the same static load, identical bearing geometry and lubricant operating conditions.

$$P=[K_{xx1}+j\omega C_{xx1},K_{xx2}+j\omega C_{xx2},K_{xy1}+j\omega C_{xy1},K_{xy2}+j\omega C_{xy2},$$
$$K_{yx1}+j\omega C_{yx1},K_{yx2}+j\omega C_{yx2},K_{yy1}+j\omega C_{yy1},K_{yy2}+j\omega C_{yy2}]^T{}_{8x1} \quad (22)$$
$$=\left[Z_{xx1},Z_{xx2},Z_{xy1},Z_{xy2},Z_{yx1},Z_{yx2},Z_{yy1},Z_{yy2}\right]^T$$

The system response matrix **Q** can then be easily decomposed into two submatrices as:

$$\mathbf{Q}^x=\begin{bmatrix}\mathbf{q}_o^T\\ \mathbf{q}_o^T\mathbf{I}\end{bmatrix}_{2x4},\ \mathbf{Q}^y=\begin{bmatrix}\mathbf{q}_o^T\\ -\mathbf{q}_o^T\mathbf{I}\end{bmatrix}_{2x4} \quad (23)$$

The superindeces *x* and *y* in Equation (4.18) are meaningful in the sense that these two matrices define the identification Equations for the bearing coefficients that affect the forces in the corresponding direction, as follows. Divide the parameter vector **P** into:

$$\mathbf{P}^x=\left[Z_{xx1},Z_{xx2},Z_{xy1},Z_{xy2}\right]^T,\ \mathbf{P}^y=\left[Z_{yx1},Z_{yx2},Z_{yy1},Z_{yy2}\right]^T \quad (24)$$

Then, the identification Equations in complex form can easily be derived from the balance of forces and moments:

$$Q^x P^x=\left[E_o+[\omega^2 M-j\omega\Omega G]q_o\right]^x \quad (25a)$$
$$Q^y P^y=\left[E_o+[\omega^2 M-j\omega\Omega G]q_o\right]^y \quad (25b)$$

Two linearly independent tests (*A*,*B*) are still required to form the response matrices and perform the identification from the two sets of Equations as:

$$\mathbf{P}^x=\overline{\mathbf{Q}}^{x^{-1}}\overline{\mathbf{E}}_T{}^x \quad (26a)$$
$$\mathbf{P}^y=\overline{\mathbf{Q}}^{y^{-1}}\overline{\mathbf{E}}_T{}^y \quad (26b)$$

where $\overline{\mathbf{Q}}^x=\begin{bmatrix}\mathbf{Q}^x{}_A\\ \mathbf{Q}^x{}_B\end{bmatrix}$, $\overline{\mathbf{Q}}^y=\begin{bmatrix}\mathbf{Q}^y{}_A\\ \mathbf{Q}^y{}_B\end{bmatrix}$, $\overline{\mathbf{E}}_T{}^x=\begin{bmatrix}\mathbf{E}_T{}^x{}_A\\ \mathbf{E}_T{}^x{}_B\end{bmatrix}$, $\overline{\mathbf{E}}_T{}^y=\begin{bmatrix}\mathbf{E}_T{}^y{}_A\\ \mathbf{E}_T{}^y{}_B\end{bmatrix}$ (27)

and

$$E_T{}^x=\left[E_o+[\omega^2 M-j\omega\Omega G]q_o\right]^x \quad (28a)$$
$$E_T{}^y=\left[E_o+[\omega^2 M-j\omega\Omega G]q_o\right]^y \quad (28b)$$

The identification Equations (26) are two sets of four Equations with four unknown impedances. Although the mathematical development is lengthier, the programming of

Equations (26) is much simpler with current mathematical software able to handle inversion operations with complex matrices.

Finally, if measurements of the rotor response are not taken at the bearing locations l_1 and l_2, a simple geometrical transformation using the assumption of rigid rotor motion allows the use of imbalance responses x_{p1}, x_{p2} at locations s_1 and s_2 away from the rotor center of gravity (see Figure 24):

$$\begin{bmatrix} x_1 \\ x_2 \end{bmatrix} = \frac{1}{(s_1+s_2)} \begin{bmatrix} (l_1+s_2) & (s_1-l_1) \\ (s_2-l_2) & (l_2+s_1) \end{bmatrix} \begin{bmatrix} x_{p1} \\ x_{p2} \end{bmatrix} \tag{29}$$

4.3 NUMERICAL EXPERIMENTS AND ASSESSMENT OF METHOD ROBUSTNESS TO NOISE

As demonstrated in the previous section, rotor response to impact excitations allows identification of frequency-dependent bearing rotordynamic coefficients at a fixed rotor speed. This section presents a numerical study with predictions obtained for the test rotor with the characteristics listed in Table 2. This rotor is of interest for the present study because it is supported on fluid film bearing that have frequency-dependent force coefficients. For the first part of this numerical study, the rotordynamic coefficients are held constant in the frequency range from 2 to 200 Hz (120-12,000 cpm) to cover an operating range of speeds (0-10,000 rpm). The choice of constant force coefficients is useful to assess the accuracy and robustness of the identification procedure. The rotor speed is set to 1,000 rpm (17 Hz) to demonstrate that the identification method provides good results for synchronous force coefficients even at low rotor speeds.

Figure 25 shows the time trace of a typical impact applied to the test rotor in the (x) horizontal direction. The particular impact shown has a duration of 2.0 ms (typical of medium-hardness rubber impact tips). One impact along the vertical direction and one impact along the horizontal direction are applied to the test rotor at the center of gravity. The impacts have also different magnitudes, 980 N in the (x) direction and 890 N in the (y) direction. These impacts represent the simplest (linearly independent) combination applied at a single axial location in the horizontal and vertical directions. The delivered impact renders a force to rotor weight ratio of ~ 2.0 in time. Figure 26 shows the frequency domain representation of the impact shown in Figure 4-2. The impact has a frequency spectrum which is usually broader than the frequency range of physical interest. Figure 26 shows a "zoom" of the excitation impact spectrum in the low frequency range (0-230 Hz) and which remains with nearly constant amplitude. The amplitude of the excitation is 3.8 N at 0 Hz, and 2.68 N at the cut-off frequency of 230 Hz. This amplitude represents the 70.7% of the amplitude at 0 Hz. Shorter impact times (harder tips), raise the cut-off frequency above 230 Hz but require larger load magnitudes to deliver similar force amplitudes in the frequency domain.

Table 6 presents the rotordynamic bearing force coefficients used to generate the numerical system response (depicted below) for the current study. Notice that the

coefficients are constant throughout the frequency range to better illustrate the goodness of the identification procedure. The magnitude of the bearing coefficients represents realistic values predicted for the tilting pad journal bearing in series with the squeeze film damper described in Chapter 3.

Table 7 shows the resulting (synchronous) damped natural frequencies and damping ratios of the rotor-bearing system as calculated from an eigenanalysis considering constant bearing stiffness and damping force coefficients. Gyroscopic effects are included in the analysis. Notice that the two rigid-body modes (cylindrical and conical) of vibration fall within the rotor operating speed range. Also note that the conical motions (second natural frequency) are more damped than the cylindrical modes.

Figure 27 shows the numerical responses (frequency response functions) at the bearing locations and for the two impacts delivered in both directions. Note that impacts in the (x) horizontal direction produce larger motions in this direction with vertical motions only due to the cross-coupled forces. The same holds for the vertical direction (y). In this example, the impacts excite only one natural frequency (translation mode) since the impacts are delivered at the rotor center of gravity. The difference in amplitude between the peaks reflects that the two bearings in the drive and free ends have different force coefficients (say due to uneven distribution of rotor load). This is usually the case in real turbomachinery.

The phase angles of the rotor response shown in Figure 28 are necessary for parameter identification since the procedure uses always the complex magnitude of the rotor response Fourier transform. Notice that the phase angle of rotor response is only meaningful when referred to the phase angle of the excitation force (relative angle of response). The phase angle of response in the orthogonal direction to the impact presents large shifts even though the impact barely excites the conical mode in the main directions. Thus, it is expected that the phase angle will have a strong influence in the identification of cross coupled force coefficients.

Finally, note that the effect of rotor speed on the response is null since the model example assumes a perfectly balanced rotor, i.e. the dynamic response at the synchronous speed is solely determined by the value of the synchronous coefficients and the magnitude of the impact force. In practice, both remnant unbalance and shaft run-out have a strong influence on the dynamic response at the running speed, and the filter described in Chapter 3 is necessary for adequate identification.

Figure 29 shows the bearing reaction forces and moments acting on and about the rotor center of gravity (CG) and calculated using Equation (4.23) for the impact in the x direction. The net force transmitted through the bearings is the sum of the forces depicted in Figure 29 plus the forces at the bearing locations created by the moments applied to the rotor CG. Thus, the load transmitted through each bearing depends on the location of the rotor CG within the bearing span. At low frequencies, the bearing transmitted dynamic force balances the impact load (small inertial terms). Bearing forces

peak at the natural frequency because the amplitudes of motion are largest, and then decrease steadily towards zero at higher frequencies (smallest transmissibility).

Before carrying out the identification of bearing parameters, it is convenient to calculate the condition number of the response matrix $\overline{Q}$ presented in Equation (4.21). The condition number (CN), defined as the product of the euclidian norm of the matrices $\overline{Q}$ and $\overline{Q}^{-1}$, provides a measure of the sensitivity of the linear system of Equations (Equations 26) to variations in the elements of the response matrix, say due to noise or uncertainty in the measurements [40]. Condition numbers close to 1 indicate that the matrix is robust and easily invertible. On the other hand, CNs grow rapidly for ill-conditioned matrices. The condition number gives also the ratio between the largest and smallest singular values of matrix $\overline{Q}$. If this ratio of singular values is so large that the smallest value can be regarded as zero, then the rank of the matrix is smaller than the dimension of its column space and thus the matrix is ill-conditioned and direct inversion is not possible.

Recall that Equation (26) is solved at each frequency considered, and thus a system of equations results. The response matrix changes as a function of frequency and so does the condition number. Figure 30 shows the condition number of the two systems of Equations in (26) as a function of the frequency of excitation. The CN remains almost constant through the frequency range, with a small peak at the resonance frequency, indicating that the method is more sensitive to small changes of response at this frequency. The value of the condition number remains around 10 for the rest of the frequencies, but at this time it is still not possible to declare the robustness of the matrix. A numerical example shown later allows a better appreciation on this result when the predicted rotor response used in the identification is contaminated by random noise.

Also, in order to better appreciate the advantages of the more elaborated construction of matrices in Equations (26), consider the condition number of the response matrix from Equation (16) for the same mechanical system. Figure 31 shows a comparison between the condition numbers in such formulations, and clearly depicts that the so-called "uni-directional" identification in Equation (26) is more robust than the initial methodology. This fact alone should pay the additional effort, but considering that the final programming is even simpler than required by the initial method, the second method is clearly superior.

Figure 32 shows the identified force coefficients of the bearing elements at a constant rotor speed of 1,000 rpm for the numerical example described above. All coefficients are perfectly identified throughout the frequency range, with deviations from the theoretical values due to numerical rounding. Excellent coefficient identification in the low frequency range in Figure 32 is explained by noting that that the amplitudes of response at low frequencies in the main directions (Figure 27) are sufficiently large (as opposed to the amplitudes of response at low speed for the case of unbalance excitations, as shown later). Notice also that the amplitudes of vibration in the orthogonal direction to the impacts are very small, and thus it is likely that these measurements will be affected

by noise in real applications, resulting in poor identification of cross-coupled force coefficients.

A second numerical example with the same test rotor but frequency-dependent force coefficients aims to demonstrate the ability of the method to identify non-constant force coefficients and also to show the effect of random noise from the measurements. The frequency dependent force coefficients used to generate the predicted response correspond to representative values of equivalent stiffness and damping coefficients for a generic bearing, but different from the experimental support described in Chapter 3. Table 8 lists the bearing coefficients used for the current predictions of response.

Figure 33 depicts the identified and original bearing coefficients as function of the frequency of excitation. Notice that the identification is also perfect in this case, with minute differences only due to numerical rounding error. This example demonstrates the ability of the method to identify bearing coefficients strongly dependent on the frequency. The next example with the same bearing coefficients serves to test the sensitivity of the identification to noise in the measurements of response.

Figure 34 shows the rotor response affected by (uniformly distributed) random noise whose magnitude is 2 percent of the magnitude of the original vibration. Although Figure 34 shows only the amplitude of response, the noise is added to the original signal as a complex number and thus affects both amplitude and phase angle of the rotor response. Figure 35 shows the identified bearing coefficients and the coefficients used to generate the numerical response. Notice that the identified coefficients follow closely the original coefficients, indicating that the identification is robust for the noise magnitudes used in the example (2 percent of original signal in this case).

Finally, notice from Equations (28) that the rotor speed affects only the gyroscopic moments. In practice, small variations in rotor speed between two consecutive impacts (x and y directions) forming a complete experiment have negligible influence on the measured response and parameter identification. Variations of speed during the data acquisition are also negligible since this would require a large rotor (angular) acceleration (a time record of ~ 0.3 seconds takes approximately 10 revolutions). Also in practice, the synchronous component filtering contributes more to variations in the response than actual changes in rotor speed.

4.4 MEASUREMENTS OF TRANSIENT RESPONSE AND RESULTS OF BEARING PARAMETER IDENTIFICATION

This section presents the measurements of applied force and rotor response, as well as the identification of frequency-dependent stiffness and damping coefficients of the combined *ISFD-FPJB* support described in Chapter 3. Identification of bearing coefficients is performed at two rotor speeds, namely 2,000 and 4,000 rpm. Impacts are delivered at the rotor middle disk and eddy current sensors at two axial locations measure

the rotor displacements. The identification Equations used in all tests are given by Equation (24).

Notice that the test rotor is identical to the rotor used in the numerical experiment presented earlier. Note also that orientation of the coordinate axes is determined by the direction of rotation (around positive z direction). The final coordinate orientation designates the free end bearing as location 1 and the drive end bearing as location 2.

The test procedure includes five repetitions of the impact excitation along each direction (x,y, horizontal and vertical). An average process in the frequency domain is performed to each group of measurements (x,y) after the runout filter is applied to each recorded time response. The use of averaging assumes that the system response is linear with respect to the applied load, an observation supported by the measurements. The averaged frequency responses and forces are then used for identification of the bearing coefficients at each frequency about the synchronous frequency of running speed.

Figure 36 shows typical impacts in the two orthogonal directions (x,y) in the time domain performed on the rotor at 2,000 rpm. Notice that the fast acquisition rate programmed is able to capture over 15 points of data during the impact, which renders a remarkably good spectrum, the time resolution being 0.078 ms. Typical experimental impact duration is about 1.2 ms, and the total time record taken is 0.32 sec, which corresponds to 4096 samples.

Figure 37 shows the frequency spectrum (amplitude) of the impacts presented in Figure 36. The highest frequency in the spectrum is 6,402 Hz, and the resolution is 3.12 Hz. Typical roll off lobes appear up to 3,000 Hz in the force spectrum, and then it remains flat indicating the softness of the impact. However, the spectrum amplitude remains essentially flat in the range between 0 to 200 Hz, spanning the range of frequencies of interest. Keep in mind that the experiment consists of 10 impacts (5 impacts along each direction) that are averaged in the frequency domain, as shown in Figure 38.These spectra are then used in the parameter identification. Notice that the amplitude of the averaged impacts in Figure 38 is smaller than the amplitudes in Figure 4-14 due to the averaging, because there is large variability between the magnitude of the impacts.

Figures 39 show time traces of the recorded rotor responses in the two axial planes and at the two directions after filtering of the shaft runout for impacts in both directions (x,y), as described in a previous section. Motions in the directions orthogonal to the direction of impact are due only to the cross-coupled effects, which are known to be small. Consequently, time traces along these directions present considerable amounts of noise. The time traces in the main direction of impact show that the rotor vibration dies out completely within the record time. Typical magnitudes of rotor motion (in time) after the release of the load are in the order of 25 microns (~ 1 mil) 0-pk for the first peak of rotor vibration. The time decay of the peak amplitudes denotes viscous damping with some amount of Coulomb damping, probably from the structural components of the bearing (i.e. S-shaped springs in the dampers, for example). Notice that the natural period

of motion of ~ 20 ms renders a ratio with respect to the impact duration in excess of 16 times; that is, the impact is considerably shorter than the first natural period of rotor vibration.

The averaging process in the frequency domain of a series of five independent impacts along each direction renders the response and load spectra to be used in the identification procedure. Figure 40 shows the averaged spectra of rotor response at 2,000 and 4,000 rpm to the impact excitations. Notice that the synchronous peak is almost perfectly filtered out in the direction of impact, but it is still present in the direction orthogonal to the impact mainly due to the smallness of the response and the cross-coupled coefficients, as discussed earlier.

Identification of the parameters is carried out in the frequency span between 0 and 200 Hz, but results are presented only for frequencies enclosing the synchronous and natural frequencies (10 – 60 Hz), because these are the frequencies of most interest from a practical point of view. Figure 41 shows the identified equivalent stiffness and damping coefficients of the two bearings for the rotor spinning at 2,000 rpm (33.3 Hz). Stiffness coefficients are very similar for the two bearings and in the two directions (x,y). The vertical stiffness (y direction, K_{yy}) of the drive end bearing is slightly larger than the vertical stiffness of the free end bearing throughout the frequency range, as a result of the larger load supported by the bearing at the drive end. Stiffness coefficients remain almost constant up to a frequency of 40 Hz (~ 1.2 times the running speed frequency) and then decrease sharply until 60 Hz, above the first system natural frequency. At this point, there is a clear distinction between the stiffness of the drive end and free end bearings, the drive end bearing presenting a larger stiffness (approximately 70 % larger than the free end bearing). At this frequency of 60 Hz, the equivalent stiffness in the vertical and horizontal directions are practically identical.

Figure 41 also shows the identified equivalent bearing damping coefficients in the main directions (x,y). Experimental identification of damping coefficients at low frequencies is not accurate due to the smallness of the damping forces developed ($j\omega C$ term in the Equations of motion). Damping coefficients about the synchronous frequency do not present a definite trend, and are more sensitive to small variations in the response than stiffness coefficients. The identified coefficients above 37 Hz take a definite trend remaining almost constant until 53 Hz and then show a sharp increase, in particular the damping coefficients of the free end bearing in the vertical direction (C_{yy}). In general, bearing damping coefficients in the vertical direction are larger than damping coefficients in the horizontal direction. This observation is consistent with the averaged amplitudes of rotor response at the natural frequency (Figure 40).

San Andres and De Santiago [36] report system damping ratios ($\xi = C/2m\omega_n$) estimated from measurements of the imbalance response of the same rotor-bearing system at the first critical speed. The system damping ratios are equal to 0.141 in the vertical direction and 0.173 in the horizontal direction. These values are in contrast with the system damping ratios identified from the current impact tests (including damping from the two bearings averaged in the range of frequencies tested) of 0.151 in the vertical

direction and 0.101 in the horizontal direction. Chapter 5 presents damping coefficients estimated from imbalance response measurements that are in close agreement with the damping coefficient reported before in [36]. Thus, it is apparent that the type of rotor motion (steady state or transient vibration) largely influences the damping forces of the bearing support.

The values of identified cross-coupled coefficients remain small for the entire range of frequencies as shown in Figure 41. Specifically, cross-coupled damping coefficients remain nearly zero with some perturbations at the running speed. Cross-coupled stiffness coefficients remain bounded and their magnitude is about 10 to 20 % the magnitude of the main stiffness coefficients. Furthermore, cross-coupled stiffness coefficients have the same sign among them in the entire frequency range. The destabilizing effect appears when the difference between the cross coupled coefficients ($K_{xy} - K_{yx}$) is less than zero. In the current case, the difference is small and the rotor bearing system remains stable for the entire range of frequencies.

Predictions for the equivalent bearing support coefficients involve estimation of the equivalent impedance from the damper and tilting pad bearing elements. The damper structural stiffness and damping coefficients are assumed to remain constant in the range of frequencies tested (see Table 9). Viscous damping coefficient calculations are based on the solution of the Reynolds Equation for an isoviscous, incompressible and isothermal fluid film [41]. On the other hand, tilting pad bearing rotordynamic force coefficients present dependence on the frequency of excitation, as shown in Table 9. Appendix B shows the formulation for the equivalent impedance of the combined support including the attachment mass, which in this case comprises the damper journal and tilting pad bearing masses (~ 1.2 kg per bearing). The equivalent stiffness and damping coefficients of the combined support listed in Table 9 present only a modest dependency on the frequency of rotor excitation. This effect on the equivalent stiffness is due to the large amounts of predicted damping from the tilting pad bearing which increases the equivalent stiffness of the series impedance as a linear function of the frequency.

Figure 42 shows a comparison between the predicted equivalent bearing force coefficients and the experimentally estimated bearing parameters in a frequency range enclosing the rotor speed and the first natural frequency. Notice the different scales used in for the direct and cross-coupled stiffness coefficients. The experiments reveal that predictions resemble very closely the stiffness coefficients and slightly over-predict equivalent main damping coefficients. Cross coupled damping coefficients are also closely predicted (nearly zero values), whereas cross coupled stiffness coefficients are of the same magnitude but of opposite sign as those derived experimentally.

The results obtained at the rotor speed of 2,000 rpm encourage the application of the impact method at higher speeds. Figure 43 shows the identified equivalent bearing coefficients at 4,000 rpm and compares them with predicted values. Notice that the running speed frequency of 66 Hz (4,000 rpm) is located just above the first rotor natural frequency (~ 60 Hz, average vertical and horizontal). Figure 43 confirms the excellent results obtained by the identification method presented in this chapter.

The sharp decrease in identified stiffness coefficients suggests that inertial effects from other components not considered in the rotordynamic model are present in the measured response. The identified stiffness presented in Figure 41 can be thought of as a dynamic stiffness (K_{dyn}) given by:

$$K_{dyn} = K - \omega^2 M_{app} \tag{30}$$

where (K) is the bearing stiffness and (M_{app}) is an apparent mass from an unidentified source, probably from the support or as a result of table resonances. In the current experiments, the stiffness identified at low frequencies can be regarded as the true bearing stiffness, and the stiffness identified at higher frequencies as the dynamic stiffness. The apparent additional mass estimated from Equation (30) is 22.6 kg in the horizontal direction and 24.0 kg in the vertical direction. This value is about 19 times larger than the mass of the attachment between the damper and the hydrodynamic bearing (i.e. damper journal and *TPJB* masses together, ~ 1.2 kg). Thus, the identified dynamic stiffness calls for a more accurate model of the bearing support (table and other components) that may be influencing the rotor response.

4.4.1 Effect of response averaging on parameter identification from impact response measurements

The purpose of this study is to confirm that increasing the number of impacts reduces the variability of the identified parameters. It also aims to find (if that is the case) the number of averages that leads to the smallest variability range. The issue arises from the nature of the identification procedure, since it requires measurements of force and displacements of linearly independent impacts applied in two orthogonal directions (the minimum requirement is along impact in one direction and another impact along the orthogonal direction). If the rotor is impacted several times in both directions, there is an increased number of possible combinations of paired responses for which the procedure can identify the bearing coefficients. For example, impact 1 in direction (x) can be grouped with impact 3 in direction (y), then impact 1 in direction (x) with impact 4 in direction (y), and so on.

The first task is to group all recorded independent impacts in the two directions to form impact pairs $(x_i, y_j)_{i,j=1\ldots5}$. The pairs formed this way are all independent experiments themselves. There are currently 5 available impacts in each direction (x, horizontal, y, vertical), rendering a total of 25 independent experiments (pairs). These pairs of impacts form a pool of experimental data from which combinations can be used for parameter identification after being averaged. For example, the pair (x_1, y_3) can be averaged with the pair (x_2,y_4). For this study, only 16 pairs are considered (resulting from 4 impacts in the horizontal directions and 4 impacts in the vertical direction) to reduce the number of possible combinations since taking all 25 combination is excessively time consuming. For example, the averaging procedure can take sets of 2 pairs. There are a total of 120 possible combinations of 2 pairs out from the original pool of 16 pairs. The

number of possible combinations increases to 560 if taking sets of 3 pairs for averaging, and continues growing for larger sets until the trend is reversed at the midpoint (sets of 8). Then, the number of possible combinations for averaging starts to decrease back to 16 combinations for sets of 15 pairs. There is only 1 combination if all 16 impact pairs are taken in one set for averaging.

Since it is still not practical to perform the identification for all possible combinations, a random sample of 16 sets is taken at each set size. For example, only 16 sets are used out of the 120 possible combinations of 2 pairs of impacts. Likewise, only 16 sets are used out of the 560 possible sets resulting of combining 3 pairs in one set. Hopefully, the random samples help to identify trends in the identified coefficients.

The identification procedure renders bearing coefficients as functions of the frequency of excitation. Even though the impact may excite a broad spectrum, usually there is a limited range of frequencies that are of interest (low frequencies, running speed and first natural frequency of the rotor-bearing system). The range of identification extends from ~ 20 Hz to 60 Hz for the current experiments at 2,000 rpm (33.3 Hz), and the measured natural frequency is ~ 52 Hz. This section presents results of identification at 25.0, 34.4 and 50.0 Hz.

Figure 44 shows the direct stiffness in the horizontal direction of bearing 1 (K_{xx1}) identified as a function of the number of pairs included in the averaging. The figure includes the case in which all 16 pairs are used in the identification (single point to the right of the horizontal scale). Figure 44 shows three graphs corresponding to the identification frequencies (low, mid and high within the chosen range). Identification at low frequencies makes evident the beneficial effect of increasing the number of pairs of impacts in the averaging. In fact, Figure 44 shows that increasing the number of pairs in the averaging beyond 9 pairs does little to improve the coefficient variability range. Thus, three impacts in each direction may suffice for a satisfactory identification of bearing coefficients.

Figure 44 also shows that the identified stiffness has larger variability at the synchronous frequency (34.4 Hz) than at low frequencies due to spurious rotor imbalance effects. Identification at higher frequencies shows that the scattering is almost unperceivable and thus only a few impacts should be needed for identification. In general, the value of stiffness rendered with the maximum available number of averages agrees with the accumulated trend from smaller number of averages.

Figure 45 shows the identified direct damping coefficient (C_{xx1}) and cross-coupled stiffness (K_{yx1}) identified also as a function of the number of averages used in the identification and at two excitation frequencies (low, 25 Hz, and mid ~ synchronous, 34 Hz). The bearing coefficients at the highest frequency considered (50 Hz) show a similar trend to that of the main stiffness (K_{xx1}), i.e. almost no scattering with respect to the number of averages used, thus not shown here for brevity.

The damping coefficient (C_{xx1}) shows large variability scattering at the two frequencies, spread in a range of up to two times its mean value. However, the tendency is clear. Increased number of averages does bring the identification process to converge towards a mean value of damping coefficient. For the two frequencies shown, all 16 impacts are necessary to provide a reliable value of damping. The cross-coupled stiffness coefficient (K_{yx1}) also shown in Figure 45 has a similar trend to that of the direct damping coefficient (C_{xx1}), but with a less variability with respect to the number of averages. In this case, 10 averages suffice to converge to a unique value.

4.4.2 Variability of identified parameters

The bearing parameters identified from impact excitations show variability depending on the experimental pair of impacts considered. As mentioned above, there are originally 25 independent experiments (pairs) available in the current study. Figures 46 show the bearing coefficients identified using the 25 pairs and as a function of the excitation frequency. Figure 46 includes vertical bars at each frequency point of identification representing the 95% confidence interval estimated from the standard deviation and the number of experiments considered.

Figure 46 (b) shows that maximum variability corresponds to the direct damping coefficients as well as to the cross coupled force coefficients in general, and close to the rotor speed synchronous frequency. In some cases, the confidence interval is so broad that coefficients might fall in a region of reversed sign. Notice that variability of direct damping coefficients at the natural frequency is small. This is particularly good because this is the frequency at which adequate identification of damping is most needed.

In order to validate the identified average bearing parameters, the rigid rotor model of Equation (6) is used to predict the rotor response at the locations of measurement (two axial planes) under known experimental excitations. A correlation factor measures the goodness of the predicted response when compared to the experimental records. The experimental responses used for comparison are additional responses not included in the averaged responses for bearing parameter identification, and thus constitute actual independent experiments. Figure 47 shows the predicted and measured rotor response as a result of experimental impacts applied in two orthogonal directions. Figure 47 also includes predictions of response based on the analytically derived equivalent bearing force coefficients given in Table 9. The predicted rotor displacements (from identified parameters) in the directions of impact follow closely the experimental responses (amplitude and phase, as shown in Figure 48), thus indicating that the identified coefficients accurately represent the bearing support characteristics.

Table 10 shows the correlation factors found for the four responses (x_1, x_2, y_1 and y_2) in the main direction of impacts. Notice that all correlation factors are greater than 0.75. Specifically, the predicted responses in the horizontal direction show correlation factors above 0.90. Predicted rotor responses in the directions orthogonal to the impact have correlation factors that are in general smaller than those responses predicted in the

direction of impact. However, the amplitude of response is much smaller than in the main directions, and the predicted responses are not at all too different from the measurements.

CHAPTER 5

IDENTIFICATION OF SPEED-DEPENDENT DYNAMIC BEARING FORCE COEFFICIENTS

5.1 INTRODUCTION

Rotordynamic force coefficients of fluid film bearings largely determine the dynamic response of a rotor-bearing system to excitation forces applied upon the rotating structure supported by the bearings. The bearing dynamic linear reaction forces result from perturbations of the rotor journal about an equilibrium position in response to external forces, such as rotor imbalance. The reaction fluid film forces are proportional to the instantaneous journal displacements (elastic forces) and velocities of the journal center (damping forces). For small motions of the rotor (journal) about a steady-state equilibrium position, rotordynamic force coefficients are defined as functions of this position within the bearing clearance. The equilibrium position is in turn a function of the bearing geometry, the static load, the lubricant viscosity and the rotor speed. In actual machinery, the equilibrium position of the bearing journal center changes as the rotor accelerates to reach the operating speed. Thus, the effective rotordynamic force coefficients of the bearing change accordingly.

Modern predictive tools allow calculation of bearing force coefficients during the design stage of high-speed turbomachinery. However, it is desirable to verify the predictions of dynamic force coefficients once the machine is running during the commissioning period and performance tests. Often, a change in operating conditions (say due to altered fluid properties, enlargement of bearing clearance and others) determines a substantial change in the dynamic response of the rotor. It is therefore necessary to have a useful identification procedure to verify the dynamic properties of bearings after machine assembly or even after years of satisfactory operation [1].

This Chapter describes a method for identification of fluid film bearing speed dependent force coefficients. The method is validated with measurements of the imbalance response of two test rotors supported on different bearing configurations. The first bearing design is the combined support Integral Squeeze Film Damper in series with a Flexure Pivot Tilting Pad Bearing, as described in Chapter 3. The second bearing design is a two-lobe, cylindrical fluid film bearing featured in a second test rig also introduced in Chapter 3.

5.2 DESCRIPTION OF METHOD FOR IDENTIFICATION OF SPEED-DEPENDENT BEARING FORCE COEFFICIENTS

Bearing parameter identification from imbalance response measurements resembles closely the procedure developed earlier for identification from transient rotor responses.

The Equations of motion of the rigid rotor are identical to those presented in Chapter 4, (Equation 6). In this case, the excitation term is a stationary, periodic excitation from rotor imbalance, with a circular frequency equal to the rotor speed. The amplitude of the applied force is proportional to the square of the rotor speed, which means that the excitation is very small at low speeds. There is inherently a phase angle of 90° between the excitation applied along the (x) and (y) directions.

Figure 24 represents the experimental rotor-bearing system described in Section 3.4 of Chapter 3 (rotor supported on *ISFD-FPJB* bearings). The only difference with the current analysis is that the planes where the impact excitation was applied now become the planes where calibrated imbalance masses are attached. As described in Chapter 4, the dynamics of the rotor supported on two anisotropic bearings are modeled as a four-degree of freedom system as the rotor traverses the first and second critical speeds corresponding to the cylindrical and conical modes of vibration, respectively. The Equations of motion are:

$$\mathbf{M}\ddot{\mathbf{q}}+\mathbf{C}\dot{\mathbf{q}}+\Omega\mathbf{G}\dot{\mathbf{q}}+\mathbf{K}\mathbf{q}=\mathbf{F}_o\, e^{j\Omega t} \tag{31}$$

where **M**, **C**, and **K** are the (4x4) inertia, damping and stiffness matrices and **G** is the gyroscopic moments matrix given by Equation (8). As before, Ω is the rotor speed, $j=\sqrt{-1}$, and t is time. $\mathbf{F}=\mathbf{F}_o\, e^{j\Omega t}$ is the excitation force vector derived from the imbalance masses attached at axial two planes on the rotor, and **q** is a vector containing the response of the rotor at the bearing locations ($1,2$) and in two orthogonal directions (x, y) i.e.

$$\mathbf{q}=[x_1, x_2, y_1, y_2]^T \tag{32}$$

Equation (31) represents a system of four Equations of motion, two of them corresponding to conservation of linear momentum, and the other two relating to conservation of angular momentum.

The generalized imbalance vector ($\mathbf{F}_o$) in Equation (31) is defined as:

$$\mathbf{F}_o=\begin{bmatrix} f_1+f_2 \\ -j(f_1+f_2) \\ -f_1d_1+f_2d_2 \\ -j(f_1d_1-f_2d_2) \end{bmatrix}\Omega^2 \tag{33}$$

where the imbalance functions f_1 and f_2 are

$$f_1=m_1r_1e^{-j\phi_1} \text{ and } f_2=m_2r_2e^{-j\phi_2} \tag{34}$$

with m_1 and m_2 as the imbalance masses attached at radii r_1 and r_2 and at circumferential locations ϕ_1 and ϕ_2, respectively, measured from the key-phasor mark on the rotor, and

positive in a direction opposite to its rotation. The key-phasor mark provides also a reference for measurement of the phase angle of rotor response. In Equations (33) and (34) the subindexes (*1,2*) represent different axial planes on the rotor. Notice that due to the nature of the excitation vector, the applied force cannot be measured but only estimated.

At steady state, the rotor response is of the form $\mathbf{q} = \mathbf{q}_o\, e^{j\Omega t}$, with the components of $\mathbf{q}_o$ being complex numbers (amplitude and phase). Thus, Equation (31) becomes:

$$j\Omega\,\mathbf{C}\,\mathbf{q}_o + \mathbf{K}\,\mathbf{q}_o = \mathbf{F}_o + [\Omega^2\mathbf{M} - j\Omega^2\mathbf{G}]\,\mathbf{q}_o \tag{35}$$

The bearing support reaction forces in the left hand side of Equation (35) are expressed as the product of a (4x16) response matrix **Q** and a vector of system parameters **P** (16x1), i.e. as in Equations (12) to (14). The response matrix **Q** is composed of linear combinations of the response vector ($\mathbf{q}_o$) and the vector of parameters which includes all bearing synchronous stiffness and damping force coefficients. Equation (35) is rewritten as:

$$\mathbf{Q}\,\mathbf{P} = \mathbf{F}_o + [\Omega^2\mathbf{M} - j\Omega^2\mathbf{G}]\,\mathbf{q}_o \tag{36}$$

Separating real and imaginary parts of the complex Equation (36) renders an undetermined system of 8 (real) linear algebraic Equations to identify 16 rotordynamic coefficients representing the two anisotropic bearing supports. A second set of imbalances (set *B*) generating linearly independent responses then completes the required number of Equations to solve (36) to determine the vector of parameters **P**.

Once again, the use of bearing impedances ($\mathbf{Z} = \mathbf{K} + j\omega\mathbf{C}$), where $\omega = \Omega$, considerably simplifies the programming effort and renders simpler identification Equations. Introducing Equations (22) to (24), a pair of identification Equations in complex form is derived from the balance of forces and moments:

$$\mathbf{Q}^x\,\mathbf{P}^x = \left[\mathbf{F}_o + \Omega^2\,[\mathbf{M} - j\,\mathbf{G}]\,\mathbf{q}_o\right]^x \tag{37a}$$

$$\mathbf{Q}^y\,\mathbf{P}^y = \left[\mathbf{F}_o + \Omega^2\,[\mathbf{M} - j\,\mathbf{G}]\,\mathbf{q}_o\right]^y \tag{37b}$$

Equations (37) are analogous in form to Equations (25). Two linearly independent tests (*A,B*) are still required to form the response matrices and perform the identification, i.e.:

$$\mathbf{P}^x = \overline{\mathbf{Q}}^{x\,-1}\,\overline{\mathbf{F}}_T^{\,x} \tag{38.a}$$

$$\mathbf{P}^y = \overline{\mathbf{Q}}^{y\,-1}\,\overline{\mathbf{F}}_T^{\,y} \tag{38b}$$

Where $\overline{\mathbf{Q}}^{x} = \begin{bmatrix} \mathbf{Q}^{x}{}_{A} \\ \mathbf{Q}^{x}{}_{B} \end{bmatrix}$, $\overline{\mathbf{Q}}^{y} = \begin{bmatrix} \mathbf{Q}^{y}{}_{A} \\ \mathbf{Q}^{y}{}_{B} \end{bmatrix}$, $\overline{\mathbf{F}}_{T}{}^{x} = \begin{bmatrix} \mathbf{F}_{T}{}^{x}{}_{A} \\ \mathbf{F}_{T}{}^{x}{}_{B} \end{bmatrix}$, $\overline{\mathbf{F}}_{T}{}^{y} = \begin{bmatrix} \mathbf{F}_{T}{}^{y}{}_{A} \\ \mathbf{F}_{T}{}^{y}{}_{B} \end{bmatrix}$ (39)

and

$$\mathbf{F}_{T}{}^{x} = \left[\mathbf{F}_{o} + \Omega^{2}\,[\mathbf{M} - j\,\mathbf{G}]\mathbf{q}_{o}\right]^{x} \tag{40a}$$

$$\mathbf{F}_{T}{}^{y} = \left[\mathbf{F}_{o} + \Omega^{2}\,[\mathbf{M} - j\,\mathbf{G}]\mathbf{q}_{o}\right]^{y} \tag{40b}$$

The condition for linear independence of the row vectors in the response matrix $\overline{\mathbf{Q}}^{x,y}$ is obtained from the solution of Equation (35). For the response vector $\mathbf{q}_o$:

$$\mathbf{q}_{o} = \mathbf{H}^{-1}(\Omega)\mathbf{F}_{o} \tag{41}$$

where

$$\mathbf{H}(\Omega) = -\Omega^{2}\mathbf{M} + j\Omega^{2}\mathbf{G} + j\Omega\mathbf{C} + \mathbf{K} \tag{42}$$

Equation (41) shows that, since the inverse of matrix $\mathbf{H}$ is a linear transformation, two linearly independent (l.i.) excitations $\mathbf{F}_{oA}$ and $\mathbf{F}_{oB}$ generate linearly independent responses $\mathbf{q}_{oA}$ and $\mathbf{q}_{oB}$. The conditions for linearly independent excitations can be stated from the definition of the excitation vector $\mathbf{F}_o$, Equation (43).

$$\mathbf{F}_{o} = \begin{bmatrix} f_1 + f_2 \\ -j(f_1 + f_2) \\ -f_1 d_1 + f_2 d_2 \\ -j(f_1 d_1 - f_2 d_2) \end{bmatrix} \Omega^{2} \tag{33}$$

The excitation in test B is linearly independent from that of test A by shifting the location and/or magnitude of the imbalance masses (m_1, m_2) at the two imbalance locations and such that the resultant vector $\mathbf{F}_{oB}$ is not a (complex) multiple of the original vector $\mathbf{F}_{oA}$. Equations 43a and 43b below show an example of imbalance functions that render linearly independent force vectors exciting the cylindrical and conical modes of vibration, respectively:

$$f_{1A} = m_1 r e^{-j\phi} \text{ and } f_{2A} = m_1 r e^{-j\phi} \tag{43a}$$

$$f_{1B} = m_1 r e^{-j\phi} \text{ and } f_{2B} = m_1 r e^{-j(\phi+\pi)} \tag{43b}$$

Notice that excitations in only one imbalance plane could not render linearly independent excitation vectors since the force vector $\mathbf{F}_{oB}$ can always be expressed as a multiple of $\mathbf{F}_{oA}$ in this case. Thus, two imbalance planes are mandatory for identification of all sixteen bearing parameters. However, imbalance masses applied at one plane different from the imbalance planes located at d_1 and d_2 from the center of gravity can

always be resolved for the original imbalance planes at d_1 and d_2. In this case, a second response at a different imbalance plane, or a response to imbalance masses at planes d_1 and d_2 is needed to complete the information for identification.

Lee and Hong [1] estimate speed-dependent synchronous bearing coefficients from Equation (36) by separating the forward and backward whirl vibration response resultant of the gyroscopic moments, but fail to provide experimental evidence on the robustness of the identification method. The elaborated procedure is not necessary since the measured vibration $\mathbf{q}_o$ already contains the forward and backward whirl components. Thus, filtered synchronous vibration data is perfectly suitable, making the identification procedure easy to implement from running machine data in the field. Note that the analysis shows that two imbalance runs (A and B) are necessary in order to identify all force coefficients from two anisotropic bearings.

Incidentally, force coefficients from perfectly isotropic bearings will cause numerical singularities during the inversion of the response matrices $\overline{\mathbf{Q}}$. The stated procedure is not able to identify the force coefficients in this case. However, assuming identical bearings on each end (for example, when the bearings support the same static load) or neglecting cross-coupled force coefficients (if they are known to be small) reduces the number of unknowns and simplifies the experimental requirements. Furthermore, these two cases are of more practical interest than the case of isotropic bearings because most bearings are anisotropic in practice (i.e. $K_{xx} \neq K_{yy}$, etc).

Tieu and Qiu [21] also identify sixteen synchronous coefficients of two different bearings supporting a rigid rotor from two or more imbalance response measurements. Tieu and Qiu utilize unfiltered responses and forward a numerical procedure to minimize noise influence. The experimental results show good correlation with theoretical predictions of force coefficients for a cylindrical journal bearing. The current identification procedure, on the other hand, can use filtered synchronous responses, and is therefore not affected by (high frequency) noise from the measurements. Modern data acquisition systems typically remove shaft run out from the measured signals using the tachometer reference. Thus this false vibration synchronous magnitude is not likely to perturb the method either.

Finally, if measurements of the rotor response are not taken at the bearing locations l_1 and l_2, the transformation shown in Equation (29) also allows the use of imbalance responses x_{p1}, x_{p2} at locations s_1 and s_2 away from the rotor center of gravity, as shown in Figure 24.

5.3 NUMERICAL EXPERIMENTS AND ASSESSMENT OF METHOD SENSITIVITY TO NOISE

To verify the method described above, numerical predictions for the imbalance response of an example rotor allow estimation of synchronous bearing coefficients over a range of operating speeds. For this numerical experiment, the rotor used is the same test

rotor introduced in Chapter 3 (see Table 2 for details of mass, inertia and geometry characteristics). Table 11 summarizes the distribution of masses of two imbalance sets *A* and *B* used to generate dynamic responses. Note that the imbalance combinations are linearly independent from each other as required by the identification procedure.

Table 6 shows (assumed) bearing synchronous stiffness and damping coefficients that remain constant throughout the identification speed range. The magnitude of these coefficients is identical to the magnitudes presented for the numerical experiment in Chapter 4 in order to allow direct comparison of the described identification methods. Table 7 presents the resulting damped natural frequencies and damping ratios of the rotor-bearing system from an eigenanalysis. Notice that the two rigid-body modes (cylindrical and conical) of vibration lie within the rotor operating range.

Figure 49 shows numerical predictions of the rotor response (amplitude and phase) at the bearing locations, i.e. $s_1 = l_1$ and $s_2 = l_2$ using Equation (41). Note that the imbalance distribution *A* excites the first mode of vibration (cylindrical), whereas the imbalance distribution *B* excites both modes of vibration (cylindrical and conical). Thus, for the imbalance response *B*, two phase shifts are clearly observed. Conical motion is evident by examining the phase angle between x_1 and x_2 locations at 7,000 rpm which is ~ 180°.

The imbalance rotor responses *A* and *B* are supplied to the developed identification algorithm (Equation 38). Figure 50 depicts the identified synchronous bearing force coefficients. The identification procedure renders poor results at low speed ratios ($\omega/\omega_{n1} < 0.6$, i.e speeds lower than 2,000 rpm for this example) mainly due to the smallness of the predicted rotor response (see Figure 49). Amplitudes of vibration below 2,000 rpm are less than 15 % (20 microns) of the maximum amplitude of vibration at the first critical speed (~ 150 microns).

Below the system first critical speed (between 2,000 and 3,000 rpm) there is a region in which the identification procedure renders improved results. The phase angle of the response begins a rapid change though relatively small amplitudes or motion are apparent, and which may contribute to the distortion of the identified cross-coupled parameters. Past 3,000 rpm and up to 6,000 rpm, the identification is satisfactory in estimating all sixteen parameters. It is then clear that the most suitable speed identification lies between the critical speeds. Identification of parameters is distorted above 6,000 rpm, mainly for the cross-coupled stiffness coefficients due to their small magnitude compared with the direct stiffness coefficients.

The identification method of this section appears to be more sensitive than the method for identification presented in Chapter 4. As mentioned earlier, the use of the same system (rotor and constant bearing coefficients) for the numerical example allows direct comparison of the identification methods. Figure 51 shows the condition number of identification matrix ($\overline{\mathbf{Q}}^{x}$) composed by the response to imbalance and to impact excitations. The frequency of excitation for the imbalance response corresponds to the rotating speed. Notice that the condition number of the matrix ($\overline{\mathbf{Q}}^{x}$) for identification from imbalance responses varies broadly, with largest values at low speeds. Identification

of parameters is not satisfactory in this region of speeds, as shown in Figure 50 since the response matrix is nearly ill-conditioned. The speed region of best identification of parameters lies between the two critical speeds corresponding with the lowest values of the condition number of the response matrix (~ at 5,500 rpm, CN ~ 100). Condition numbers above 200 make the identification procedure fail in giving satisfactory results.

Figure 51 shows also that the matrix ($\overline{\mathbf{Q}}^{x}$) for the case of identification from response to impacts is much more robust. The condition numbers are at least 10 times smaller than the minimum condition numbers for the current identification method. As in Chapter 4, a second imbalance response calculation is aimed to verify the negative effect of noise in the measurements by adding (uniformly distributed) random noise to the predicted response. In this case, the rotor is supported on bearings with speed-dependent force coefficients (these coefficients are shown in a following figure for comparison with the identified parameters). The bearing coefficients are arbitrary functions of speed that resemble actual predictions of stiffness and damping coefficients. Figure 52 shows the calculated responses with the same imbalance distribution presented above and with 2% noise in amplitude and phase (only amplitudes are shown here for brevity). Notice that this level of noise is identical to the level used in the previous numerical experiment presented in Chapter 4.

Figure 53 shows the identified bearing coefficients in the principal directions as a function of rotor speed as determined from imbalance responses including noise. The identification procedure renders satisfactory values only in the range between 2,000 and 5,000 rpm. Above this speed, the identified coefficients show scatter without a definite trend. Identification of cross-coupled coefficients (not shown) is quite poor over the entire range of speeds.

The numerical experiment presented above confirms that the identification method is sensitive to noise and extraneous effects that affect the ideal behavior of the rotor. However, the next section shows that, under adequate assumptions, identification of speed-dependent parameters is possible for a limited number of conditions.

5.4 MEASUREMENTS OF IMBALANCE RESPONSE AND RESULTS OF BEARING PARAMETER IDENTIFICATION

This section describes the experimental identification of bearing parameters from the measured imbalance response of the test rotors described in Chapter 3. The combined support *ISFD-FPJB* featured in the first test rig has also speed-dependent force coefficients due to the tilting pad bearing. Table 12 shows predicted equivalent bearing coefficients as a function of the rotor speed. Equivalent bearing coefficients change more as a function of rotor speed than as a function of the frequency of excitation (see Table 8). Furthermore, dynamic force coefficients of the two-lobe bearings featured in the second test rig presented in Chapter 3 are solely a function of the rotating speed. Thus, it is important to forward a practical method of identification by proposing adequate assumptions to circumvent the limitations presented in the previous section.

5.4.1 Identification of speed-dependent bearing coefficients without cross-coupling

Many small turbomachines operating at moderate speeds feature rigid fluid film bearings operating below the threshold speed of instability, determined by the cross-coupled coefficients developed in the lubricant film. In many cases, the cross-coupled coefficients are small over a broad range of speeds. At times, these machines require softer supports for reduced load transmissibility at the running speed or to better control the amplitudes of response when traversing the critical speeds. Retrofitting of these machines with tilting pad bearings is not justified in this case, but the use of squeeze film dampers is still appealing for control of vibration and transmitted forces.

The test rig described in Chapter 3 is modified with an *ISFD-FPJB* bearing on one end (drive) and a cylindrical fluid film bearing in series with a cylindrical squeeze film damper on the opposite end (free)[3]. Recall that this type of damper is the most popular design in use to date. The original objective of the experiments was to verify the rotor performance on the combined supports operating with a bubbly mixture of air and lubricant [42]. The recorded measurements of rotor vibration are used in this section for bearing parameter identification.

Figure 54 shows the test rig featuring the new support on its free end. The rotor properties remain unchanged as well as the lubricant operating conditions (i.e. no air is purposely added to the lubricant for the case of parameter identification shown here). Table 13 shows the characteristics of the new bearing support installed in the free end of the rotor including the cylindrical bearing and damper. The design of the cylindrical bearing produces fluid film stiffness coefficients that are similar to the coefficients from the tilting pad bearing, so that the critical speeds are expected not to be affected by the new support. Equivalent cross-coupled force coefficients are also small for the speed range of identification.

As demonstrated by the identification of frequency-dependent force coefficients in Chapter 4, equivalent cross-coupled force coefficients of the *ISFD-FPJB* support are about one order of magnitude smaller than the force coefficients in the principal directions. Furthermore, measurements of rotor response to imbalance with the modified series support show no trace of subsynchronous rotor vibration. Thus, a reasonable assumption in this case is that the cross-coupled forces are small, and the identification procedure thus ignores the cross-coupled coefficients to provide satisfactory identification of coefficients along the principal directions.

The identification procedure requires only small changes for the case of negligible cross-coupling force coefficients. The mathematical development is identical to the one described by Equations (31) to (37). However, the identification matrix ($\overline{\mathbf{Q}}^{x}$) is now a

[3] The rationale for the modification obeys an unfortunate accident which destroyed the babbitt liner in one of the TPJBs. Repairs took several weeks.

square (2x2) matrix since the motions in the horizontal direction are completely decoupled from the motions in the vertical direction. The simpler identification matrices are:

$$\mathbf{Q}^x = \begin{bmatrix} x_1 & x_2 \\ -l_1 x_1 & l_2 x_1 \end{bmatrix} \tag{44a}$$

$$\mathbf{Q}^y = \begin{bmatrix} y_1 & y_2 \\ l_1 y_1 & -l_2 y_1 \end{bmatrix} \tag{44b}$$

Equations (37) are still used for identification of parameters. The new force vectors and vector of identified impedances are:

$$\mathbf{F_d}^x = \begin{bmatrix} \mathbf{F}_1 \\ \mathbf{F}_3 \end{bmatrix}, \quad \mathbf{F_d}^y = \begin{bmatrix} \mathbf{F}_2 \\ \mathbf{F}_4 \end{bmatrix} \tag{45}$$

$$\mathbf{P}^x = \begin{bmatrix} \mathbf{Z}_{xx1} \\ \mathbf{Z}_{xx2} \end{bmatrix}, \quad \mathbf{P}^y = \begin{bmatrix} \mathbf{Z}_{yy1} \\ \mathbf{Z}_{yy2} \end{bmatrix} \tag{46}$$

and the response vector $\mathbf{q}_o$ includes only the motions in the desired identification direction:

$$\mathbf{q_o}^x = \begin{bmatrix} x_1 \\ x_2 \end{bmatrix}, \quad \mathbf{q_o}^y = \begin{bmatrix} y_1 \\ y_2 \end{bmatrix} \tag{47}$$

Notice that only one imbalance response is required for the identification since the number of parameters is reduced by half.

Figure 55 shows the synchronous test rotor responses at the bearing locations due to the imbalance condition described in Table 14. Figure 54 corresponds to responses compensated for the slow roll and remnant imbalance vectors, as described in Section 3.5. Note that the amplitudes of motion at the critical speed at location 2 (drive end bearing) are larger than the amplitudes at location 1. Figure 55 shows only the phase angles of response in the horizontal direction, with a clear shift occurring around 2,500 rpm.

Figure 56 shows the estimated amplitudes of the dynamic forces and moments applied to the rotor by the imbalance (Equations 45). Notice that these forces are comparable in magnitude with the impact forces delivered in the previous experiments with impulse excitations at the frequency equal to the system natural frequency (see Figure 29). At higher frequencies, the forces developed by the imbalance are much larger than those from impact excitations.

Figure 57 shows the condition number of the reduced identification matrices (with experimental responses) as given by Equations (49). Notice that the magnitude of the condition number as a function of the rotor speed is dramatically smaller than that of the full-formulation described in Section 5-3. Thus, identification of bearing parameters in this simplified case is more tolerant to noise.

Figure 58 shows the identified (synchronous) bearing force coefficients as a function of the rotor speed. Equivalent stiffness coefficients remain almost constant for speeds up to 3,000 rpm, and then show a sharp decrease, very similar to the trend presented by frequency-dependent force coefficients identified above 40 Hz (2,400 cpm, see Figure 45). Notice that the magnitudes of stiffness at location 1 (free end) are slightly lower than the magnitudes at location 2 (drive end), probably due to the difference of the *SFD* elastic support used. Most importantly, note that the free end bearing stiffness is reduced more sharply than the stiffness of the drive end bearing. It appears then that the table dynamics affects more the free end bearing.

Identified synchronous damping coefficients remain constant for the entire range of identification speeds. Also, damping coefficients at location 1 (free end) are larger than the damping coefficients at location 2 (drive end). This is a result of the cylindrical damper that provides larger damping forces to the free end bearing, as evidenced by the smaller magnitude of response at this location, see Figure 55.

The predicted rotor response with the identified parameters is identical to the measured rotor response because the parameters are identified at discrete speeds. On the other hand, equivalent bearing coefficients seem to have a small dependency on the rotor speed for the range of identification speeds. Thus, it is desirable to compare the values of the identified coefficients using the method presented here with coefficients identified using a simple least squares error minimization procedure for identification of constant coefficients over a range of frequencies.

The proposed identification using least squares also considers that the system cross-coupled forces are small and thus neglects cross-coupled force coefficients. The least squares estimation results of stacking all experimental responses at different rotor speeds to form an over-determined system of Equations (from Equations 44) and then solve it using the pseudo inverse of the response matrix. Fritzen [12] introduces a refinement to the least squares method that reduces the bias error in the measurements. The method is known as the Instrumental Variable Filter (IVF). The operations performed during the pseudo-inverse on the response matrix and that are affected by the bias error are corrected by a noise-free auxiliary model, noticeable improving the results.

Table 15 shows the results of the identification from the least squares error minimization and the instrumental variable filter. The values represent the equivalent bearing parameters over the speed range from 1,500 to 3,050 rpm. Note that the magnitudes of stiffness resemble the values obtained for the speed-dependent equivalent bearing coefficients shown in Figure 58. Magnitudes of direct damping coefficients in the

vertical direction are similar to the identified values from the speed-dependent identification method. However, damping coefficients identified in the horizontal direction are substantially smaller than the values previously identified. These damping values are quite sensitive to the range of identification speeds used.

Predictions of rotor response from the identified coefficients presented in Table 15 aid to assess the reliability of the identification procedure. Figure 59 depicts the predicted synchronous rotor response amplitude at the drive end in the horizontal direction (x_2) using the coefficients identified from the least square method. Note that the difference is large between the predicted and the experimental response. Figure 60 shows the predicted rotor response (magnitude and phase) at the same location (x_2) using the bearing coefficients identified with the Instrumental Variable Filter. Note that the predicted response follows closely the test measurements, showing an appreciable improvement from the least squares method. Thus, the equivalent coefficients identified with the IVF scheme render more representative bearing characteristics. Nonetheless, the bearing synchronous force coefficients obtained with Equations (44) are the values of the bearing parameters that exactly produce the measured rotor response.

5.4.2 Identification of speed-dependent bearing coefficients for the case of identical bearing supports.

The AMOCO test rig described in Chapter 3 has identical, two-lobed fluid film bearings that support a symmetric rotor. It is thus reasonable to expect that the bearings have similar dynamic coefficients since both of them carry similar static loads and should operate at similar static journal eccentricities.

Assuming that the bearings have identical dynamic force coefficients also reduces the number of unknown impedances from eight to just four. The identification matrix in this case is given by:

$$\mathbf{Q}^x = \begin{bmatrix} x_1 + x_2 & y_1 + y_2 \\ -l_1 x_1 + l_2 x_2 & -l_1 y_1 + l_2 y_2 \end{bmatrix} \tag{48a}$$

$$\mathbf{Q}^y = \begin{bmatrix} x_1 + x_2 & y_1 + y_2 \\ l_1 x_1 - l_2 x_2 & l_1 y_1 - l_2 y_2 \end{bmatrix} \tag{48b}$$

and the corresponding vectors of parameters are:

$$\mathbf{P}^x = \begin{bmatrix} \mathbf{Z}_{xx} \\ \mathbf{Z}_{xy} \end{bmatrix}, \quad \mathbf{P}^y = \begin{bmatrix} \mathbf{Z}_{yx} \\ \mathbf{Z}_{yy} \end{bmatrix} \tag{49}$$

Equations (37) are used again to identify the bearing parameters, with the vectors of response given by Equation (47). Note that only one imbalance response is required for identification of all coefficients because the identification matrices (Equations 48) are

square, and the row vectors are linearly independent. Even for the case of a symmetric rotor ($l_1 = l_2 = l$), the response matrix in the horizontal (x) direction is:

$$\mathbf{Q}^x = \begin{bmatrix} x_1 + x_2 & y_1 + y_2 \\ l(-x_1 + x_2) & l(-y_1 + y_2) \end{bmatrix} \tag{50}$$

Note that:

$$(x_1 + x_2) \neq (-x_1 + x_2) \tag{51}$$

and thus the rows of the matrix in Equation (50) are always linearly independent and the matrix is invertible for proper identification.

Table 16 shows predictions of the bearing force coefficients based on an isoviscous, isothermal fluid model [41]. As mentioned earlier, close examination of the bearing surfaces reveals that the bearings have uneven wear around the inner diameter from previous experiments in which the bearings operated with pressurized air as the working fluid. Wear makes it difficult to precisely determine the original preload of the bearing lobes. A small nominal value of 0.05 dimensionless preload is used for the predictions of dynamic force coefficients presented in Figure 16.

Note that the predicted direct stiffness coefficients in directions (x) and (y) are different. The magnitude of the stiffness in the vertical (y) direction is about twice the magnitude of the stiffness in the (x) direction. Increased stiffness of the fluid film in the direction of the lobe pad is typical of preloaded bearings and usually aims to increase the threshold speed of instability. Cross-coupled stiffness coefficients are of opposite sign in almost all the operating speed range. Table 16 shows that the bearing damping force coefficients are in general strong functions of the running speed. Note that the magnitude of the cross-coupled damping coefficients is of the same order of magnitude as the direct damping coefficients in the (x) direction.

The eigenanalysis of the rotor-bearing system from a finite-element model indicates that the rotor does not cross a natural frequency in the speed range to 4,000 rpm. However, note that the rotor shaft is very slender as compared to the rotor span (ratio of bearing span to rotor shaft diameter is ~ 21). The calculated shaft lateral stiffness (K_s) is only 2.5 MN/m, rendering a pin-pin natural frequency of 4,575 cpm. Figure 61 shows the ratio of bearing stiffness to shaft stiffness $\overline{K} = \dfrac{K_{xx} + K_{yy}}{K_s}$ [37] as a function of rotor speed. The values of the stiffness ratio indicate that the shaft is considerably less rigid than the predicted lubricant film stiffness ($\overline{K} \approx 1.4$). Thus, the current identification procedure is reliable only for speeds below the pin-pin natural frequency. Identification of bearing coefficients is dependable as long as the magnitude of the rotor motions are large enough to allow for accurate measurement of the phase angle. The current study shows results of the parameter identification from 1,000 to 3,000 rpm (25% to 75% of the first natural frequency).

Figure 62 shows the test synchronous (slow roll and baseline compensated) imbalance response at the bearing locations resulting from the imbalance masses attached at the rotor disk locations. See Table 17 for a summary of the imbalance conditions. Note that the measured rotor responses are at different axial planes from the bearing planes and at different radial planes, thus a suitable coordinate transformation is required from the measurements to obtain the responses presented in Figure 62. Note that the largest values of rotor dynamic response correspond to more than 50% of the bearing total clearance as the rotor approaches the critical speed. The experimental responses show different amplitudes of vibration at the two bearing locations as a result of the uneven imbalance distribution. In fact, amplitudes of motion at location 1 (drive end) are larger than the amplitudes of motion at location 2 (free end) because the drive end disk carries the imbalance mass.

Figure 63 shows the identified bearing coefficients using Equations (37) and response matrices from Equation (49). The direct stiffness coefficients remain almost constant throughout the speed range, with vertical stiffnesses (K_{yy}) being almost twice the values of the horizontal stiffnesses (K_{xx}). At low speeds damping coefficients are larger in the horizontal direction (C_{xx}) than in the vertical direction (C_{yy}), approaching similar values at higher speeds (~ 3,000 rpm).

Cross coupled stiffness coefficients are nearly constant for the speed range of identification and much smaller in magnitude than the direct stiffness coefficients. Note that the cross-coupled stiffness coefficients are of opposite sign, revealing the follower force created by the fluid film in the rigid (2-lobe) bearings. Cross coupled damping coefficients are also small and of opposite sign, and almost null at 2,000 rpm. These results indicate the possible contribution of the shaft flexibility on the dynamic response.

The identification procedure thus renders the equivalent stiffness and damping force coefficients of the journal bearing in series with the shaft stiffness. Considering the flexibility of the shaft, the equivalent impedances of the rotor-bearing system are the entries of the impedance matrix $\mathbf{H}_{eq}$, where:

$$\mathbf{H}_{eq} = \mathbf{H}_s - \mathbf{H}_s (\mathbf{H}_s + \mathbf{H}_b)^{-1} \mathbf{H}_s \tag{52}$$

and

$$\mathbf{H}_s = \begin{bmatrix} K_s & 0 \\ 0 & K_s \end{bmatrix}, \quad \mathbf{H}_s = \begin{bmatrix} K_{xx} + j\Omega C_{xx} & K_{xy} + j\Omega C_{xy} \\ K_{yx} + j\Omega C_{yx} & K_{yy} + j\Omega C_{yy} \end{bmatrix} \tag{53}$$

Figure 64 shows comparisons of the identified bearing coefficients and the predicted coefficients considering shaft flexibility. The shaft flexibility has an important effect on the equivalent force coefficients rendering values which are very close to the identified coefficients. The identification procedure is unable to estimate the bearing force coefficients due to the flexibility of the shaft, but renders accurate values of the equivalent impedance in this case. In-situ identification of bearing coefficients would then be difficult to assess unless the equations of motion include a more elaborated rotor model.

CHAPTER 6

CONCLUSIONS AND RECOMMENDATIONS

This report details the procedures (along with experimental validation) for identification of rotordynamic force coefficients of a series bearing support (*ISFD-FPJB*) as function of the frequency of excitation or as function of the rotor speed. Bearing parameters as functions of the frequency of excitation are useful for stability analyses and transient response calculations. On the other hand, speed-dependent bearing force coefficients are necessary for predictions of rotor response to imbalance.

Appropriate experimental procedures are forwarded for identification of the bearing force coefficients based on the configuration of the available test rigs. The identification methods have the potential for application in the field with the intent of verifying predictions of bearing dynamic force coefficients. The methods are based on measurements of the rotor response to transient (impact) excitations and on measurements of the rotor response to imbalance. Transient responses allow identification of frequency-dependent bearing force coefficients, whereas imbalance response measurements allow identification of speed-dependent bearing parameters. It is important to note that the use of two axial planes for rotor excitation allows identification of all bearing coefficients from two bearings supporting a rotor.

Identification from impact excitations of the *ISFD-FPJB* series support indicates that the equivalent stiffness and damping force coefficients are not strong functions of the frequency of excitation, but rather remain nearly constant in the frequency range of identification (20 to 60 Hz). An inertial effect attributed to the support causes a reduction in the direct dynamic stiffness coefficients at frequencies higher than the first rotor-bearing system natural frequency (52-56 Hz). In general, predicted bearing coefficients show good agreement with the experimentally derived coefficients within the frequency range of identification.

Numerical experiments demonstrate that the identification method based on measurements of the rotor transient response is less sensitive to noise than the identification from rotor imbalance responses. In general, identification of bearing parameters from imbalance responses is least sensitive to noise at the rotor critical speeds because the amplitudes of rotor motion are largest at these speeds and the signal to noise ratio is a maximum.

The use of tilting pad bearings (confirmed by predictions of the bearing coefficients) justifies assuming that cross-coupled forces of the series support are small. Experimental identification of frequency-dependent direct force coefficients confirms the predictions and strengthens the argument favoring a reduction in the number of unknowns. The assumption reduces the number of unknowns by effectively decoupling the rotor motions in the vertical and horizontal planes. The identification procedure is more robust than the

full formulation and renders satisfactory values of the bearing dynamic force coefficients as functions of the rotor speed.

Identification from measurements of the rotor imbalance response renders experimentally derived parameters of the series support that agree well with predictions. In general, equivalent stiffness and damping force coefficients remain almost constant for the range of speeds tested (1,000 to 4,000 rpm). The experimentally derived dynamic support stiffness also shows an important reduction as in the case of identification from impact excitations at similar frequencies (above the first critical speed, ~3,000 rpm).

A second validation of the procedure developed for identification of speed-dependent bearing parameters is performed on a test rig featuring two-lobe fluid film journal bearings. In this case, the experimental arrangement justifies assuming two identical bearings on each end of the rotor and a subsequent reduction in the total number of identified parameters. The identification from imbalance response measurements is largely influenced in this case by the flexibility of the shaft, as confirmed by predictions of the equivalent bearing-rotor impedances that agree well with the identified parameters.

One of the original objectives of the research project is to confirm the benefits of the combined *ISFD-FPJB* support and to assess its dynamic properties. The measurements of rotor response to impacts and to imbalance forces confirm that the bearing support is effective in controlling the rotor amplitudes of motion. The experimentally derived equivalent force coefficients also validate the computational tools currently available for prediction of the bearing parameters.

A second objective of the experimental program is to forward identification methods that have the potential for in-situ implementation. The identification procedures described in Chapters 4 and 5 are suitable for use in the field, although special mechanical arrangements must be devised in one case, namely identification from transient responses. This is due to the difficulty to access the rotor shaft for delivering the needed load while the rotor spins. On the other hand, using imbalances to generate rotor response requires accurate measurement of the phase angle, which is difficult at low speeds. Furthermore, this last procedure is inherently more sensitive to noise than the identification from transient responses.

The identification procedures developed are limited to the case of nearly rigid rotors. Many turbomachines in the field have flexible rotors that operate super-critically for increased power to weight ratios. Thus, it is necessary to extend the procedures for identification of bearing force coefficients supporting flexible rotors. The major change with respect to the presented methods is in the inertia matrices of Equation (15) that must include the effect of the shaft flexibility. Yang and Chaung [42] utilize the inertia matrices from a finite element model to estimate the contributions of the discrete masses on the bearing supports. Modern rotordynamic predictive codes based on finite elements represent an option for quick shaft modeling and may provide the required inertia and elastic properties.

The identification method based on transient excitations of the rotor is more robust than the identification method from imbalance response measurements. However, the obvious difficulty of directly exciting the shaft while spinning calls for an alternative procedure that takes advantage of the robustness of the method to noise. A viable alternative is to impact the machine casing instead of the rotating structure. Relative rotor motions with respect to the bearing housing as well and absolute support motions (accelerations) provide the necessary information for bearing parameter identification. However, an appropriate model of the support structure is necessary in this case. Feng and Hahn [43] have developed several experimental methods for modeling of turbomachinery foundations that might be useful for bearing parameter identification.

Acknowledgements

The support of the Turbomachinery Research Consortium and the partial support of the National Science Foundation are gratefully acknowledged. Also, the assistance from undergraduate students Fernando Romero, Dario Rubio, and Adolfo Delgado to carry out the experiments described is greatly appreciated.

REFERENCES

[1] Lee, C. W., and S. W. Hong, 1989, "Identification of Bearing Dynamic Coefficients By Imbalance Response Measurements", *Proc. Instn. Mech. Engrs.*, Vol. 203, pp. 93-101.

[2] Zeidan, F., 1995, "Application of Squeeze Film Dampers", *Turbomachinery International*, Vol. 11, September/October, pp. 50-53.

[3] De Santiago, O., J. Oliveras, and L. San Andrés, 1999, "Imbalance Response of a Rotor Supported on Open-Ends Integral Squeeze Film Dampers", *ASME Journal of Gas Turbines and Power*, Vol. 121, 4, pp. 718-724.

[4] Kozin, F., and H. G. Natke, 1986, "System Identification Techniques", Structural Safety, The Netherlands, Vol. 3, pp. 269-316.

[5] Diaz, S., and L. San Andrés, 2000, "Orbit-Based Identification of Damping Coefficients For a Rotor Mounted on Off-Centered Squeeze Film Dampers and Including Support Flexibility", ASME Paper GT-2000-.

[6] Goodwin, M. J., 1991, "Experimental Techniques for Bearing Impedance Measurement", Transactions of the ASME, *Journal of Engineering for Industry*, Vol. 113, Aug., pp. 335-342.

[7] Mitchell J. R., R. Holmes, and H. Van Bellegooyen, 1966, "Experimental Determination of a Bearing Oil Film Stiffness", *Proc. Inst. Mech. Engrs.*, Vol. 180, Pt. 3k. pp. 45-53

[8] Burrows, C. R., and M. N. Sahinkaya, 1982, "Frequency-Domain Estimation of Linearized Oil-Film Coefficients", Transactions of the ASME, Journal of Lubrication Technology, Vol. 104, April, pp. 210-215.

[9] Morton, P. G., 1971, "Measurement of the Dynamic Characteristics of a Large Sleeve Bearing," *Journal of Lubrication Technololgy*, Jan. pp. 143-149.

[10] Parkins, D. W., 1979, "Theoretical and Experimental Determination of the Dynamic Characteristics of a Hydrodynamic Journal Bearing", *Journal of Lubrication Technology*, Vol. 101, April, pp. 62-68.

[11] Brockwell, K., D. Kleinbub, and W. Dmochowski, 1990, "Measurement and Calculation of the Dynamic Operating Characteristics of the Five Shoe, Tilting Pad Journal Bearing", *Tribology Transactions*, No. 4, pp. 481-492.

[12] Fritzen, C., 1986, "Identification of Mass, Damping and Stiffness Matrices of Mechanical Systems", *Journal of Vibration, Acoustics, Stress and Reliablitly in Design*, Vol. 108, No. 1, pp. 9-16.

[13] Diaz, S. E., and L. A. San Andrés, 1999, "A Method for Identification of Bearing Force Coefficients and Its Application to a Squeeze Film Damper with a Bubbly Lubricant", *Tribology Transactions*, Vol. 42, No. 4, pp. 739-746.

[14] Rouvas, C., and D. W. Childs, 1993, "A Parameter Identification Method for the Rotordynamic Coefficients of a High Reynolds Number Hydrostatic Bearing", Transactions of the ASME, *Journal of Vibration and Acoustic*, Vol. 115, July, pp. 264-270.

[15] Woodcock, J. S., and R. Holmes, 1970, "Determination and Application of the Dynamic Properties of a Turbo-Rotor Bearing Oil Film", *Proc. Inst. Mech. Engrs*, Vol. 184, pt 3l, pp. 223-231.

[16] Sahinkaya, M. N., and Burrows, C. R., 1984, "Estimation of Linearized Oil Film Parameters from the Out-of-Balance Response," *Proc. Inst. Mech. Engrs.*, Vol. 198c, No. 8, p. 131-139.

[17] Goodwin, M. J., 1981, "Variable Impedance Bearings for Large Rotating Machinery," Ph D Thesis, Aston University, United Kingdom.

[18] Robison, M., G. Arauz, and L. San Andrés, "A Test Rig for the Identification of Rotordynamic Coefficients of Fluid Film Bearings," ASME Turbo-Expo'95 Conference, Houston, June 1995 (ASME Paper 95-GT-431).

[19] Nordmann, R. and K. Shollhorn, 1980, "Identification of Stiffness and Damping Coefficients of Journal Bearings by Means of the Impact Method", International Conference on Vibration in Rotating Machinery (ISROMAC), IMechE, Cambridge, England, pp. 231-238.

[20] Morton, P. G., 1975, "Dynamic Characteristics of Bearings-Measurement Under Operating Conditions", *GEC Journal of Science and Technology*, Vol. 42, No. 1, pp. 31-37.

[21] Tieu, A. K., and Z. L. Qiu, 1994, "Identification of Sixteen Dynamic coefficients of Two Journal Bearings From Experimental Imbalance Responses", *Wear*, Vol. 177, pp. 63-69.

[22] De Choudhury, P., Hill, M. R., and Paquette, D. J., 1992, "A Flexible Pad Bearing System for a High Speed Centrifugal Compressor", *Proceedings of the 21st Turbomachinery Symposium*, Dallas, Tx, pp 57-64.

[23] Zeidan, F. Y., and Paquette, D. J., 1994, "Application of High Speed and High Performance Fluid Film Bearings in Rotating Machinery", *Proceedings of the 23st Turbomachinery Symposium*, Dallas, Tx, pp 57-64.

[24] Edney, S. L., and Nicholas, J. C., 1999, "Retrofitting a Large Steam Turbine with a Mechanically Centered Squeeze Film Damper", *Proceedings of the 28th Turbomachinery Symposium*, Houston, TX, pp 29-40.

[25] Kuzdzal, M. J., and J. F. Hustak, 1996, "Squeeze Film Damper Bearing Experimental vs. Analytical Results For Various Damper Configurations", *Proceedings of the 25th Turbomachinery Symposium*, Texas A&M University, Houston, TX, pp. 57-70.

[26] Thomsen, K. K., and H. Andersen, 1974, "Experimental Investigation of a Simple Squeeze Film Damper", Transactions of the ASME, *Journal of Engineering for Industry*, Vol. 96, pp. 427-430, May.

[27] Tonnesen, J., 1975, "Experimental Parametric Study of a Squeeze Film Bearing", Transactions of the ASME, *Journal of Lubrication Technology*, Vol. 98, pp. 206-213, April.

[28] San Andrés, L. A., and J. M. Vance, 1988, "Effects of Fluid Inertia on Finite-Length Squeeze-Film Dampers", *ASLE Transactions*, Vol. 30, pp. 384-393.

[29] San Andrés, L., Díaz, S., and Rodríguez, L., 2001, "Sine Sweep Load Versus Impact Excitations and their Influence on the Damping Coefficients of a Bubbly Oil Squeeze Film Damper", 56th STLE Annual Meeting, Orlando, Fl. May. Paper STLE 01-NP-18.

[30] San Andrés, L., and D. Lubell, 1998, "Imbalance Response of a Test Rotor Supported on Squeeze Film Dampers", ASME *Journal of Engineering for Gas Turbines and Power*, Vol. 120, pp. 397-404, April.

[31] Brockwell, K. R. and D. Kleinbub, 1989, "Measurement of the Steady State Operating Characteristics of the Five Shoe, Tilting Pad Journal Bearing", *Tribology Transactions*, Vol. 32, No. 2, pp. 267-275.

[32] Someya, O. J., 1988, "Journal Bearing Data Book", Springer Verlag, Berlin.

[33] Ha, H. C., and S. H. Yang, 1998, "Excitation Frequency Effects on the Stiffness and Damping Coefficients of a Five-Pad Tilting Pad Journal Bearing" ASME paper No. 98-TRIB-44.

[34] Pettinato, B. C., R. D. Flack, and L. E. Barrett, 2001, "Effects of Excitation Frequency and orbit Magnitude on the Dynamic Characteristics of a Highly Preloaded Three-Lobe Journal Bearing", *Tribology Transactions*, Vol. 44, pp. 575-582.

[35] Pettinato, B. and P. De Choudhury, 1998, "Test Results of Key and Spherical Pivot Five-Shoe Tilt Pad Journal Bearings –Part II: Dynamic Measurements", STLE Preprint No. 98-TC-3B-2.

[36] L. San Andrés, and O. De Santiago, 2001, "Imbalance Response of a Rotor Supported on Flexure Pivot Tilting Pad Journal Bearings in Series With Integral Squeeze Film Dampers," ASME Paper 2001-GT-0257.

[37] Nicholas, J. C., and Kirk, R. G., 1979, "Selection and Design of Tilting Pad and Fixed Lobe Journal Bearings For Optimum Turborotor Dynamics", *Proceedings of the 8th Turboamchinery Symposium*, Texas A&M University, Houston TX, pp.43-57.

[38] Lund, J. W., 1964, "Spring and Damping Coefficients for the Tilting-Pad Journal Bearing", *ASLE Transactions*, Vol. 7, pp. 342-352.

[39] Parsell, J. K., P. E. Allaire, and Barrett, L. E., 1983, "Frequency Effects in Tilting Pad Journal Bearing Dynamic Coefficients", *ASLE Transactions*, Vol. 26, April, pp. 222-227.

[40] Davis, H. T., and K. T. Thomson, 2000, "Linear Algebra and Linear Operators in Engineering With Applications in Mathematica", Academic Press, San Diego, pp. 87-95.

[41] San Andrés, 1996, "Turbulent Flow, Flexure-Pivot Hybrid Bearing for Cryogenic Applications," *ASME Journal of Tribology*, Vol. 118, 1, pp. 190-200.

[42] Yang, T., and Chaung, W.C., 2000, "Identification of Bearing Coefficients of Flexible Rotor-Bearing Systems," ASME Paper 2000-GT-400.

[43] Feng, N. S., and Hahn, E. J., 1997, "Identification of the Modal Parameters of a Flexibly Supported Casing", ASME Paper 97-GT-447.

Table 1. Integral squeeze film damper and flexure pivot tilting pad bearing main dimensions and operating conditions.

Squeeze film damper:		
Damper land radius (R_d)	48.26 mm	1.900 in
Land radial clearance (c_d)	0.229 mm	0.009 in
(after static deflection under rotor weight)		
Damper axial length (L_d)	23.00 mm	0.910 in
Land arc extent (in circumferential direction, nom.)		52°
Flexure pivot tilting pad bearing: 4 pads (70°)		
Bearing nominal diameter:	30.15 mm	1.187 in
Bearing axial length: (L_b)	22.9 mm	0.902 in
Pad radial clearance: (c_p)	0.127 mm ± 0.005 mm	0.0050 in ± 0.00013 in
Pad preload: 0.405 (r_p)	0.0508 mm	2 mils
Pivot offset:	0.50	
Bearing radial clearance: (c_b)	0.076 mm	3 mils
Pad rotational stiffness:	40 N-m/rad	354 lb-in/rad
Clearance on back of pads:	0.178 mm (typ)	0.007 in (typ)
Average inlet lubricant viscosity (μ)	15.76 cP	at 24.4° C (76° F)
Operating speed range:	0-10,000 rpm	
Static load between pads		
Drive end bearing	247.3 N	55.53 lb (51.90 psi - specific load)
Free end bearing	198.2 N	44.50 lb (41.56 psi - specific load)

Table 2. Summary of rotor geometry characteristics and inertia properties of test rig for identification of equivalent bearing parameters.

Units	*ISO*		*English*	
Rotor mass	41.7 kg		91.8 lb	
Rotor total mass (including half of flexible coupling) (m)	45.3 kg		99.8 lb	
Rotor total transverse moment of inertia (I_T)	0.704 kg-m^2		2406 lb-in^2	
Rotor total polar inertia (I_P)	0.299 kg-m^2		1022 lb-in^2	
	mm		in	
Shaft diameter	76.2		3.00	
Shaft diameter at bearing locations	29.99		1.181	
Total length	673.1		26.50	
Bearing span	406.4		16.0	
Rotor cg location from left end	285.0		11.2	
Distances from cg to bearing locations (l_1,l_2)	0.189	0.217	7.44	8.54
Distances from cg to planes of impact excitation (d_1,d_2)	0	0	0	0
Distances from cg to location of proximity probes (s_1,s_2)	0.119	0.146	4.69	5.75

Table 3. Instrumentation for impact response measurements.

Measured magnitude	Instrument	Gain
Force, (x) horizontal	Dynamic load cell	11.4 mV/N (50.73 mV/lb)
Force, (y) vertical	Dynamic load cell	12.7 mV/N (56.65 mV/lb)
Displacement (x_1), *Free end horizontal*	Proximity probe	8.07 mV/micron (204.5 mV/mil)
Displacement (x_2), *Drive end horizontal*	Proximity probe	7.91 mV/micron (200.2 mV/mil)
Displacement (y_1), *Free end vertical*	Proximity probe	7.64 mV/micron (193.5 mV/mil)
Displacement (y_2), *Drive end vertical*	Proximity probe	8.11 mV/micron (205.3 mV/mil)

Table 4. Summary of test rotor geometry characteristics and inertia properties for unbalance response measurements.

Units	*ISO*		*English*	
Rotor mass	11.8 kg		26.0 lb	
Rotor total transverse moment of inertia (I_T)	0.234 kg-m^2		800 lb-in^2	
Rotor total polar inertia (I_P)	0.030 kg-m^2		102 lb-in^2	
	mm		in	
Shaft diameter	25.4		1.00	
Shaft diameter at bearing locations	25.4		1.00	
Total length	640.0		25.20	
Bearing span	532.0		20.94	
Rotor cg location from left end	342.0		13.46	
Distances from cg to bearing locations (l_1,l_2)	263	269	10.4	10.6
Distances from cg to planes of unbalance excitation (d_1,d_2)	137	143	5.39	5.63
Radii of unbalance locations (r_1,r_2)	70.0	70.0	2.76	2.76
Distances from cg to location of proximity probes (s_1,s_2)	302	308	11.9	12.1

Table 5. Two-lobe bearing main dimensions and operating conditions.

Bearing nominal diameter (D)	25.4 mm	1.000 in
Bearing axial length (L_b)	28.6 mm	1.126 in
Bearing radial clearance (c_b)	0.089 mm	3.5 mils
Estimated pad preload (r_p)	0.05 (dimensionless)	
Average inlet lubricant viscosity (μ)	15.76 cP	at 24.4° C (76° F)
Operating speed range:	0-4,000 rpm	
Static load between pads		
Drive end bearing	57.9 N	13.0 lb (11.55 psi - specific load)
Free end bearing	57.9 N	13.0 lb (11.55 psi - specific load)

Table 6. Bearing parameters used to generate (synchronous) imbalance response (constant over the speed range) and response to ideal impacts (constant over a frequency range).

Bearing 1 = Bearing 2:

Stiffness coefficients (N/m)	Damping coefficients (N-s/m)
$K_{xx} = 3.0 \times 10^6$	$C_{xx} = 2{,}000$
$K_{yy} = 3.5 \times 10^6$	$C_{yy} = 2{,}200$
$K_{xy} = 5.0 \times 10^4$	$C_{xy} = 250$
$K_{yx} = 3.0 \times 10^4$	$C_{yx} = 800$

Table 7. Calculated damped natural frequencies and damping ratios of test rotor-bearing system with constant stiffness and damping coefficients (gyroscopic effects included).

Mode of vibration:

Cylindrical	
$\omega_1 = 57.8$ Hz, 61.3 Hz (3467, 3676 cpm)	$\xi_1 = 0.114, 0.131$
Conical	
$\omega_2 = 83.3$ Hz (4997 cpm, backwards)	$\xi_2 = 0.201$
$\omega_2 = 123$ Hz (7360 cpm, forward)	$\xi_4 = 0.199$

Table 8. Frequency-dependent bearing coefficients used for numerical example.

Freq.	K_{xx}	K_{yy}	K_{xy}	K_{yx}	C_{xx}	C_{yy}	C_{xy}	C_{yx}
Hz	N/m				N-s/m			
18	2.946	3.257	0.049	0.029	2.036	2.240	0.259	0.815
38	2.888	3.006	0.048	0.028	2.077	2.285	0.270	0.831
58	2.831	2.775	0.047	0.027	2.119	2.331	0.281	0.848
78	2.775	2.562	0.046	0.026	2.162	2.378	0.292	0.865
98	2.720	2.365	0.045	0.025	2.206	2.427	0.304	0.882
118	2.666	2.183	0.044	0.024	2.250	2.476	0.317	0.900
138	2.613	2.015	0.044	0.023	2.296	2.526	0.329	0.918
158	2.562	1.860	0.043	0.022	2.342	2.577	0.343	0.937
178	2.511	1.717	0.042	0.021	2.390	2.629	0.357	0.956
198	2.461	1.585	0.041	0.020	2.438	2.682	0.371	0.975

Coefficients shown are for bearing 1. Values of coefficients for bearing 2 are 80% of the values for bearing 1.

Table 9. Predicted tilting pad bearing force coefficients and equivalent bearing coefficients of series support *FPJB-ISFD* as functions of the excitation frequency.

Tilting pad bearing coefficients (average of drive and free ends)
2,000 rpm (33.3Hz)

Frequency	K_{xx}	K_{yy}	K_{xy}	K_{yx}	C_{xx}	C_{yy}	C_{xy}	C_{yx}
(Hz)	MN/m				KN-s/m			
16.6	18.1	17.9	7.50	5.74	42.6	43.0	14.1	17.1
33.3	17.5	17.1	7.19	5.59	43.8	44.2	15.2	17.7
53.3	16.2	16.1	6.57	5.23	45.9	46.2	16.4	18.6

Squeeze film damper force coefficients
Structural stiffness (average x and y directions): 3.4 MN/m (experimentally validated)
Predicted damping coefficients (0.3 orbit eccentricity, circular centered orbit): 950 N-s/m.

Equivalent bearing coefficients of tilting pad bearing and squeeze film damper in series

Frequency	K_{xx}	K_{yy}	K_{xy}	K_{yx}	C_{xx}	C_{yy}	C_{xy}	C_{yx}
(Hz)	MN/m				KN-s/m			
16.6	2.81	2.80	-0.16	-0.20	1730	1757	80.46	309.3
33.3	2.80	2.79	-0.16	-0.18	1675	1712	102.7	268
53.3	2.76	2.76	-0.14	-0.14	1553	1560	119.2	203

Mass of attachment between the series impedances (including damper journal and tilting pad bearing masses): 1.2 kg per bearing.

Table 10. Correlation factors between predicted and measured responses for two impacts delivered in the horizontal (x) and vertical (y) directions.

Frequency range used for estimation of correlation factor: 2-200 Hz
Rotor response predicted using identified parameters and experimental forces

Impact in horizontal direction (x)		Impact in vertical direction (y)	
Location of response	Correlation factor r^2	Location of response	Correlation factor r^2
x_1	0.96	x_1	0.609
x_2	0.93	x_2	0.678
y_1	0.145	y_1	0.758
y_2	0.134	y_2	0.891

Table 11. Unbalance mass distribution for numerical example of rotor dynamic response.

Location	Left end	Right end
Unbalance A	7.9 gr at 6°	6.6 gr at 6°
Unbalance B	8.0 gr at -8 °	6.5 gr at 180°

Left end disk: radius $r_1 = 0.114$ m, distance from rotor CG $d_1 = 0.067$ m.
Right end disk: radius $r_2 = 0.095$ m, distance from rotor CG $d_2 = 0.102$ m.
Positive angles on rotor are measured opposite to direction of rotation and from rotating reference (i.e. keyway in rotor or reflective pick-up mark).

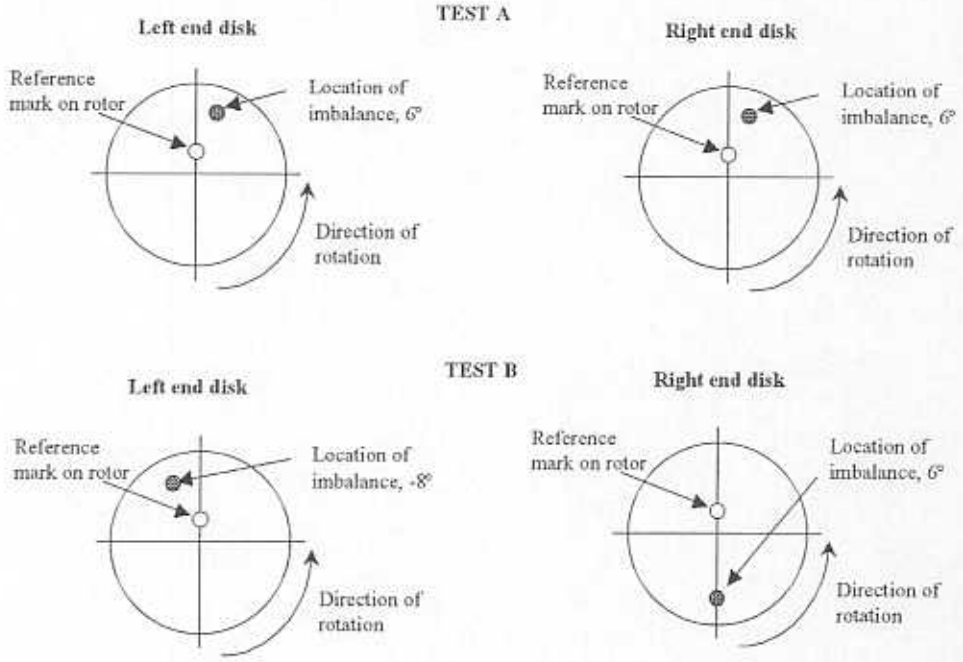

Table 12. Predicted equivalent bearing coefficients of *ISFD-FPJB* support as a function of the running speed.

Tilting pad bearing synchronous (1x) coefficients (average of drive and free ends)

Speed	K_{xx}	K_{yy}	K_{xy}	K_{yx}	C_{xx}	C_{yy}	C_{xy}	C_{yx}
(rpm)	MN/m				kN-s/m			
1,000	28.41	28.53	12.50	10.71	119	118	53.8	58.6
2,000	19.45	19.58	7.624	6.050	48.2	47.9	16.0	18.7
3,000	16.10	16.23	6.030	4.499	29.7	29.5	8.09	9.89
4,000	14.07	14.20	5.075	3.548	21.1	20.9	4.90	6.28
5,000	12.80	12.95	4.517	2.968	16.3	16.2	3.42	4.54
6,000	11.92	12.09	4.164	2.572	13.4	13.3	2.65	3.60
7,000	11.26	11.47	3.933	2.284	11.5	11.4	2.20	3.13
8,000	10.76	11.01	3.783	2.069	10.1	10.0	1.91	2.65
9,000	10.44	10.73	3.707	1.903	9.07	8.98	1.73	2.39
10,000	9.99	10.32	3.580	1.727	8.16	8.07	1.54	2.16

Squeeze film damper force coefficients

Structural stiffness (average x and y directions): 3.4 MN/m (experimentally validated)
Predicted damping coefficients (0.3 orbit eccentricity, circular centered orbit): 950 N-s/m.

Equivalent bearing coefficients of tilting pad bearing and squeeze film damper in series

Speed	K_{xx}	K_{yy}	K_{xy}	K_{yx}	C_{xx}	C_{yy}	C_{xy}	C_{yx}
(rpm)	MN/m				kN-s/m		N-s/m	
1,000	3.013	3.013	-0.152	-0.139	2.00	1.99	349	187
2,000	2.874	2.876	-0.158	-0.142	1.63	1.61	228	91.6
3,000	2.765	2.766	-0.155	-0.136	1.41	1.40	169	54.4
4,000	2.652	2.654	-0.149	-0.127	1.27	1.26	126	26.7
5,000	2.537	2.539	-0.142	-0.117	1.16	1.15	93.5	7.73
6,000	2.413	2.416	-0.134	-0.108	1.07	1.07	67.5	-6.03
7,000	2.279	2.283	-0.127	-0.099	1.01	1.00	46.3	-18.5
8,000	2.132	2.137	-0.118	-0.087	0.95	0.95	29.1	-22.7
9,000	1.973	1.979	-0.108	-0.075	0.91	0.90	14.3	-27.3
10,000	1.792	1.799	-0.097	-0.063	0.87	0.87	2.59	-30.1

Table 13. Bearing characteristics and main dimensions of support consisting of a rigid fluid film bearing and a cylindrical squeeze film damper.

Squeeze film damper:			
Damper journal diameter (D_d)	95.0 mm		3.740 in
Land radial clearance (c_d)	0.229 mm		0.009 in
(after static deflection under rotor weight)			
Damper axial length (L_d)	23.00 mm		0.910 in
Land extent (in circumferential direction, nom.)		360°	

Fluid film bearing		
Bearing type:	Full cylindrical with upper feeding hole at axial midplane	
Material:	Bronze	
Bearing nominal diameter:	30.15 mm	1.187 in
Bearing axial length: (L_b)	29.0 mm	1.142 in
Bearing radial clearance: (c_b)	0.051 mm	2 mils
Average inlet lubricant viscosity (μ)	15.76 cP	at 24.4° C (76° F)
Operating speed range:	0-6,000 rpm	
Static carrying load:	198.2 N	44.5 lb (32.8 psi - specific load)

Table 14. Unbalance distribution of test rotor for experimental identification of series-support equivalent synchronous force coefficients.

	Drive end disk	Free end disk
Unbalance	3.2 gr at 30°	3.3 gr at 30°

Drive end disk: radius $r_2 = 0.114$ m, distance from rotor CG $d_2 = 0.067$ m.
Free end disk: radius $r_1 = 0.095$ m, distance from rotor CG $d_1 = 0.102$ m.
Positive angles on rotor are measured opposite to direction of rotation and from rotating reference (i.e. keyway in rotor or reflective pick-up mark).

Table 15. Summary of identification of equivalent bearing force coefficients in the principal directions from least squares and instrumental variable filter over a range of speeds.

Id method	K_{xx1}	K_{xx2}	K_{yy1}	K_{yy2}	C_{xx1}	C_{xx2}	C_{yy1}	C_{yy2}
	MN/m				N-s/m			
LS	1.38	3.89	2.21	3.41	1130	514	2620	1630
IVF	1.46	3.73	2.02	3.45	937	546	3100	1287
SDav	1.89	2.37	2.22	2.24	3940	2228	2747	1795

Range of speeds for identification: 1,500 to 3050 rpm
LS: Least squares error minimization
IVF: Instrumental Variable Filter
SDav: Average speed dependent force coefficients identified in the given range of speeds.

Table 16. Predicted bearing coefficients of two-lobe bearing as a function of the running speed.

Speed	K_{xx}	K_{xy}	K_{yx}	K_{yy}	C_{xx}	C_{xy}	C_{yx}	C_{yy}
rpm	N/m				N-s/m			
400	1.11	-0.47	-3.02	5.55	17.05	-31.18	-31.13	131.14
1,000	1.10	0.03	-2.44	3.27	10.22	-11.69	-11.68	44.68
1,500	1.12	0.26	-2.32	2.74	7.98	-7.31	-7.30	28.96
2,000	1.14	0.47	-2.26	2.38	6.77	-5.15	-5.14	21.47
2,500	1.17	0.64	-2.27	2.24	6.07	-3.90	-3.89	17.54
2,750	1.18	0.73	-2.28	2.17	5.81	-3.45	-3.43	16.12
3,000	1.19	0.82	-2.29	2.11	5.61	-3.06	-3.05	14.97
3,250	1.20	0.91	-2.33	2.12	5.48	-2.73	-2.72	14.27
3,500	1.21	1.00	-2.37	2.13	5.37	-2.45	-2.43	13.66
3,750	1.23	1.09	-2.41	2.14	5.28	-2.20	-2.18	13.14
4,000	1.24	1.19	-2.45	2.15	5.20	-1.98	-1.97	12.68
4,250	1.25	1.28	-2.49	2.16	5.13	-1.79	-1.78	12.28
4,500	1.26	1.37	-2.53	2.17	5.06	-1.62	-1.60	11.92
4,750	1.27	1.47	-2.58	2.19	5.00	-1.47	-1.45	11.61
5,000	1.28	1.56	-2.63	2.23	4.94	-1.30	-1.28	11.39

Bearing radial clearance: 89 microns
Dimensionless preload: 0.05

Table 17. Unbalance distribution of test rotor for parameter identification of two-lobe bearing force coefficients.

	Drive end disk	Free end disk
Unbalance	10.6 gr at 0°	0 gr at 0°

Drive end disk: radius $r_1 = 0.070$ m, distance from rotor CG $d_1 = 0.139$ m.
Free end disk: radius $r_2 = 0.070$ m, distance from rotor CG $d_2 = 0.141$ m.
Positive angles on rotor are measured opposite to direction of rotation and from rotating reference (i.e. keyway in rotor or reflective pick-up mark).

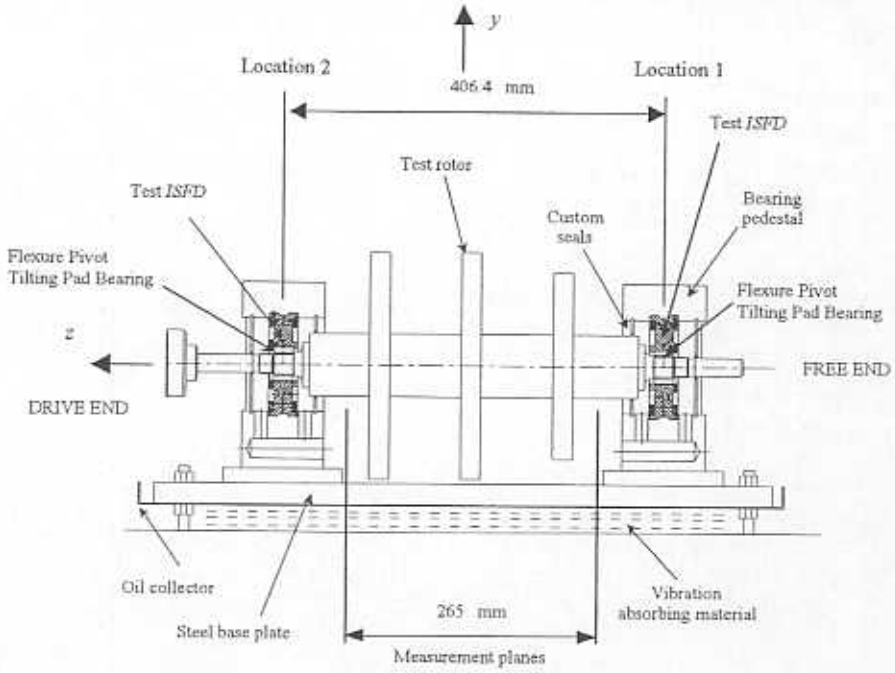

Figure 1. Test rig for measurements of transient response of rotor supported on hydrodynamic bearings and squeeze film dampers.

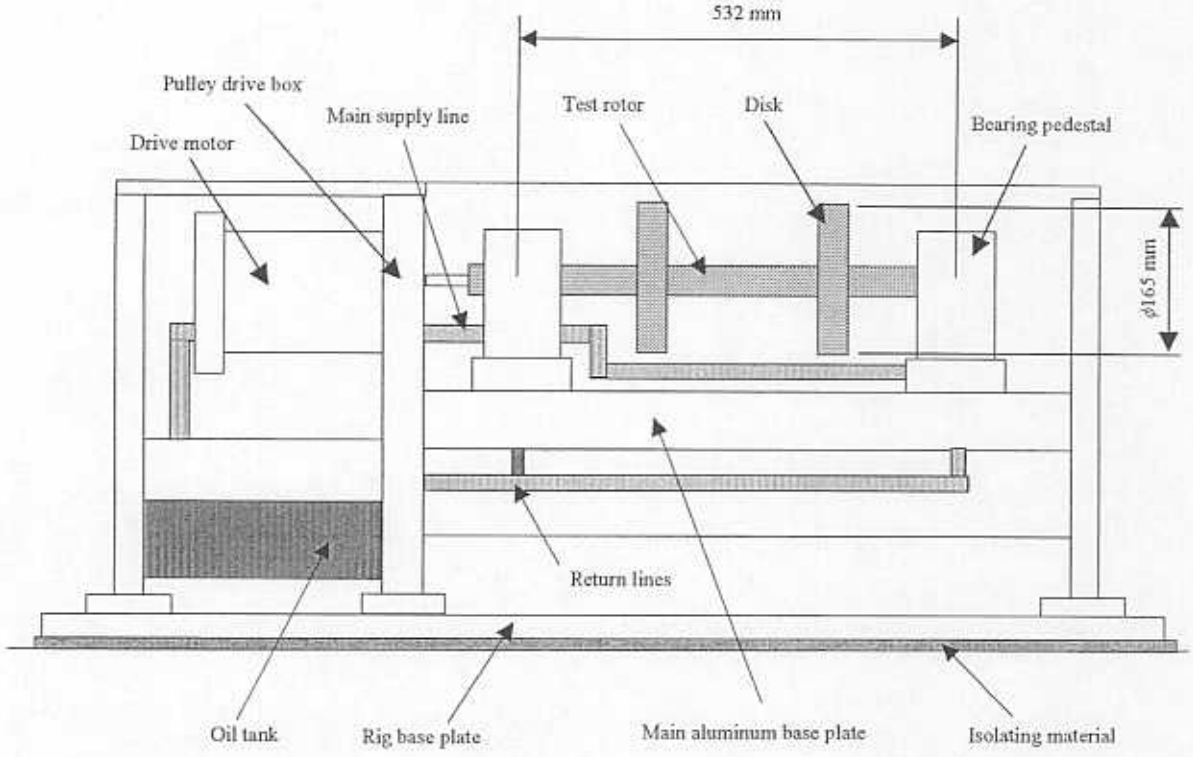

Figure 2. AMOCO test rig for imbalance response measurements of rotor mounted on hydrodynamic bearings.

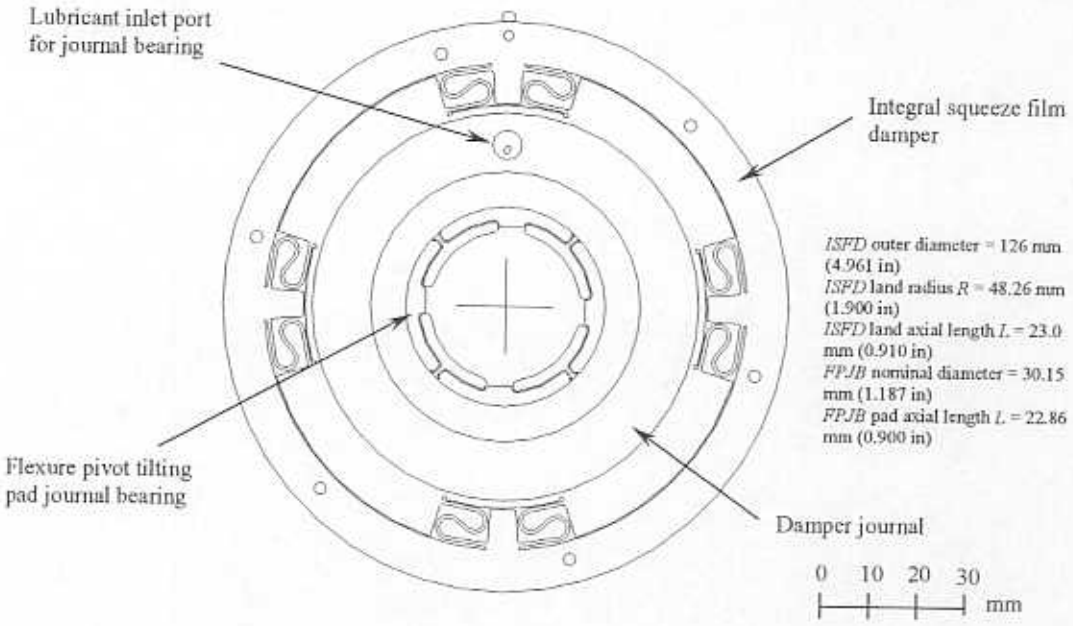

Figure 3. Integral squeeze film damper and flexure pivot tilting pad journal bearing assembly.

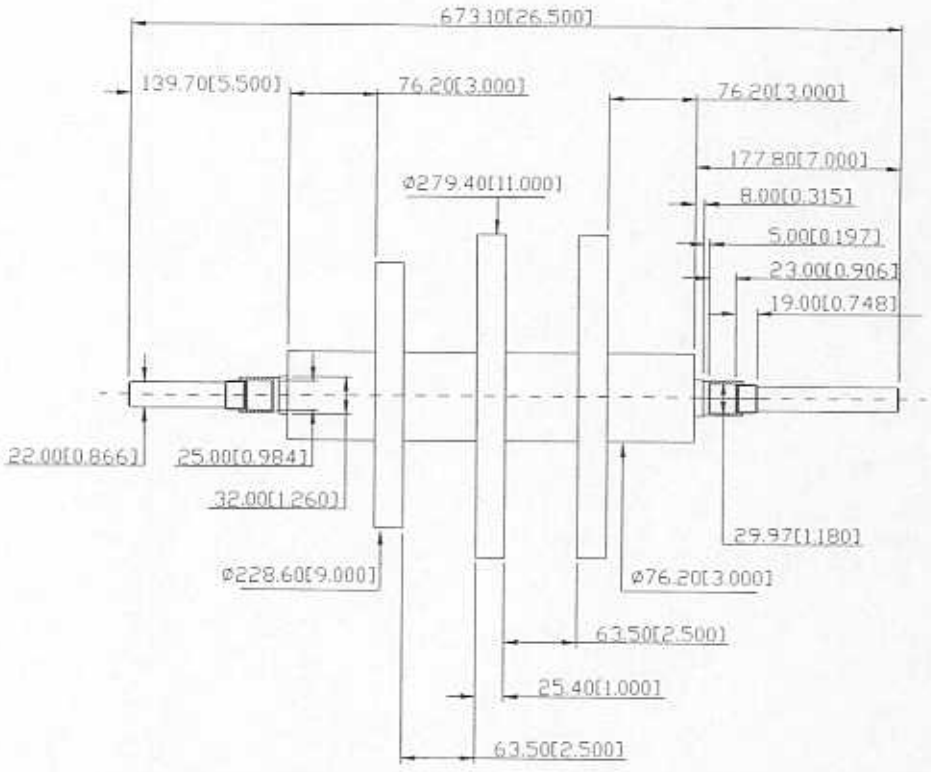

Figure 4. Geometry of three-disk rotor (mass 41.7 kg, 91.8 lb). Test rig shown in Figure 1.

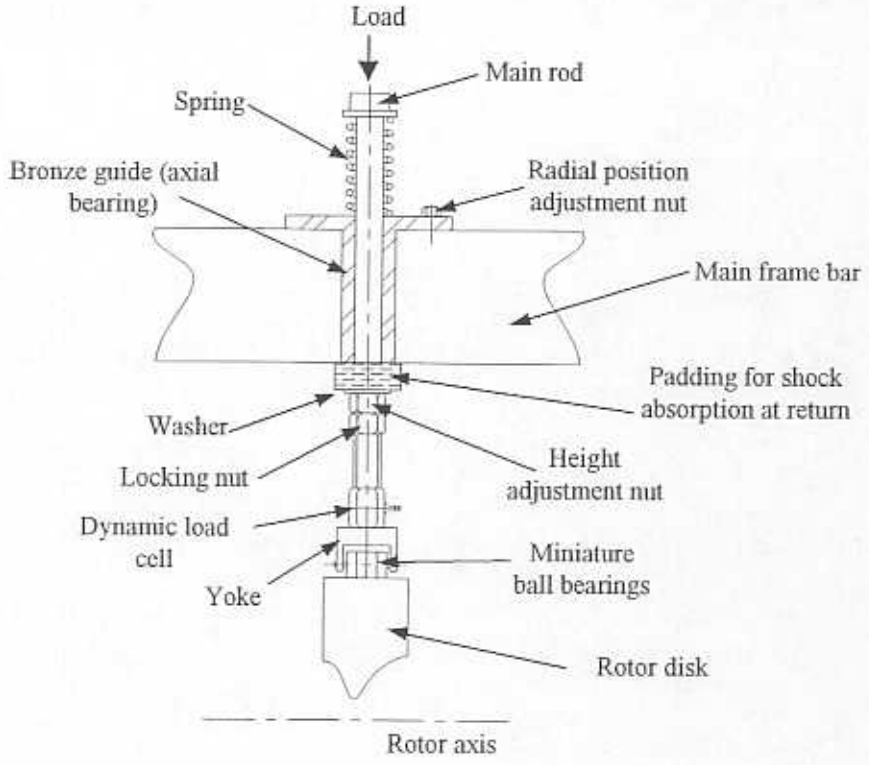

Figure 5. Detail of mechanism for delivery of impact load on the rotor disk.

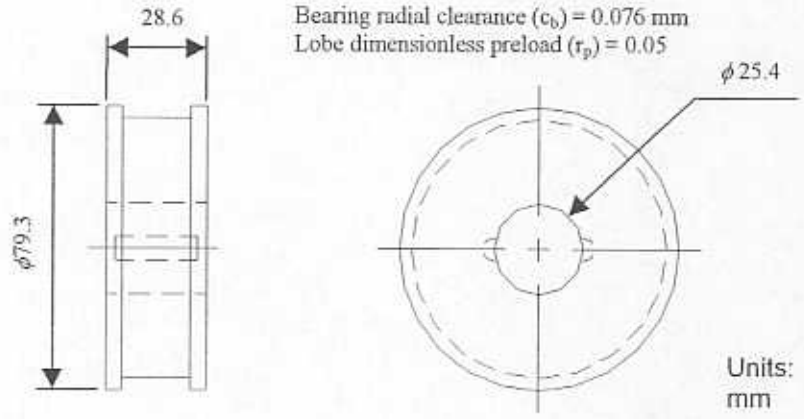

Figure 6. Two-lobed, cylindrical fluid film hydrodynamic journal bearings for parameter identification experiments. (Test rig shown in Figure 2).

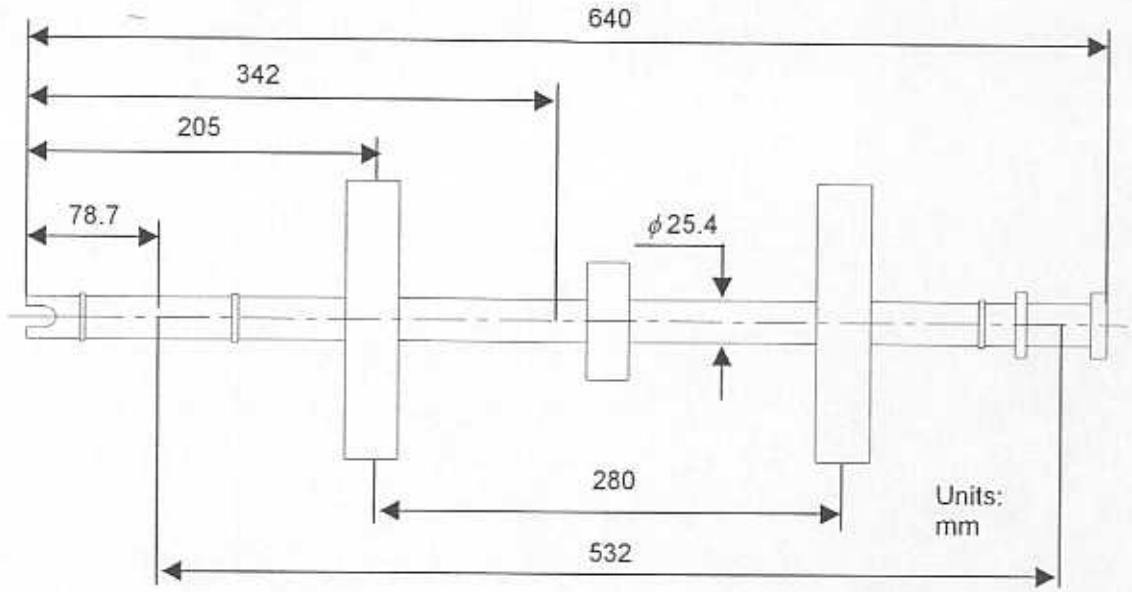

Figure 7. Test rotor for experiments on bearing parameter identification from imbalance response measurements. (Rig shown in Figure 2).

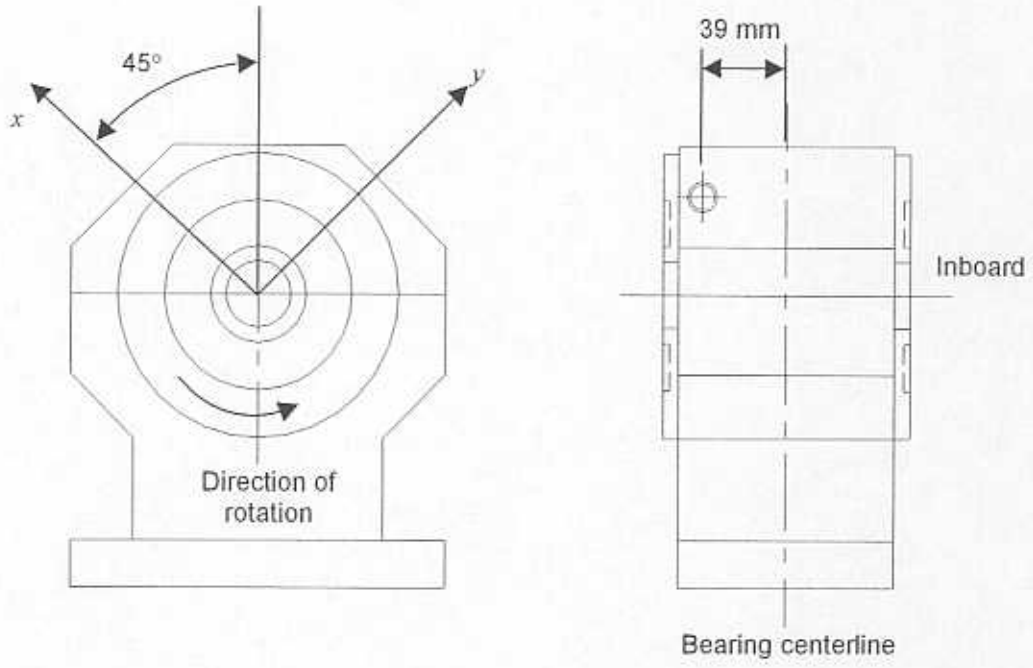

Figure 8. Bearing housing and location of proximity probes for measurement of rotor response to imbalance. (Rig shown in Figure 2).

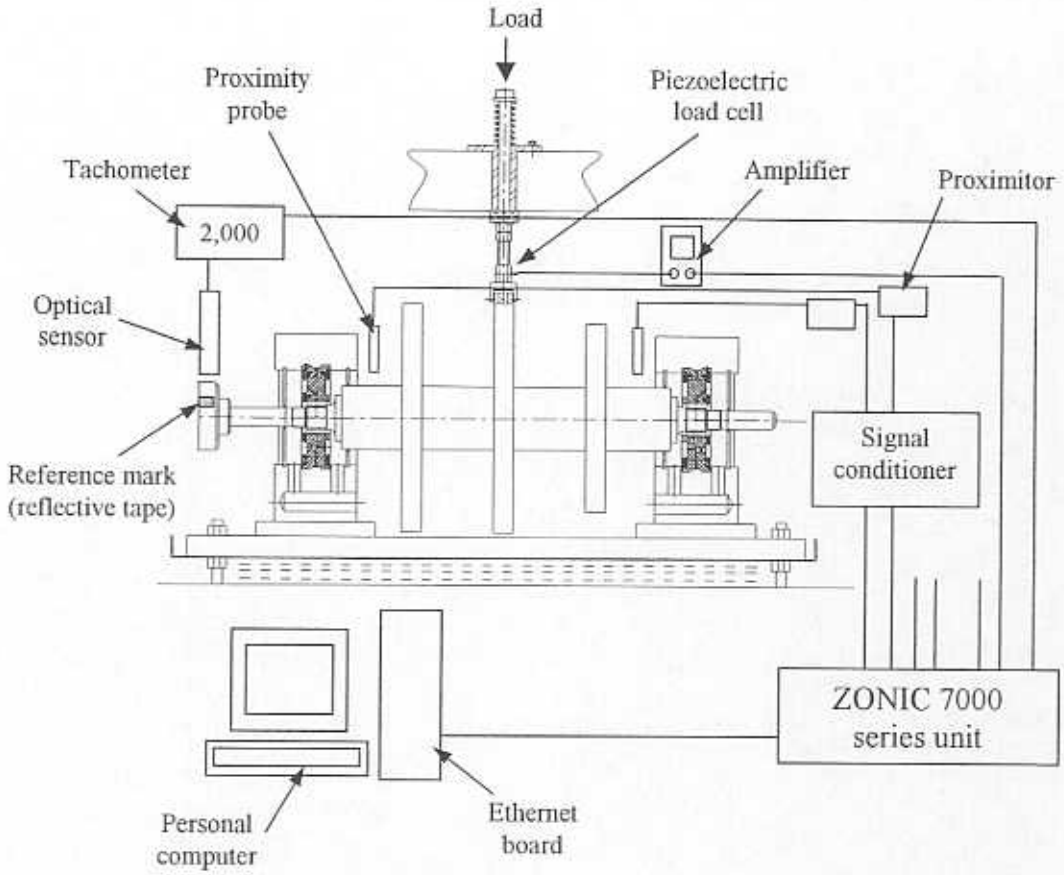

Figure 9. Data acquisition system for measurement and recording of rotor vibration, applied load and speed for transient rotor response.

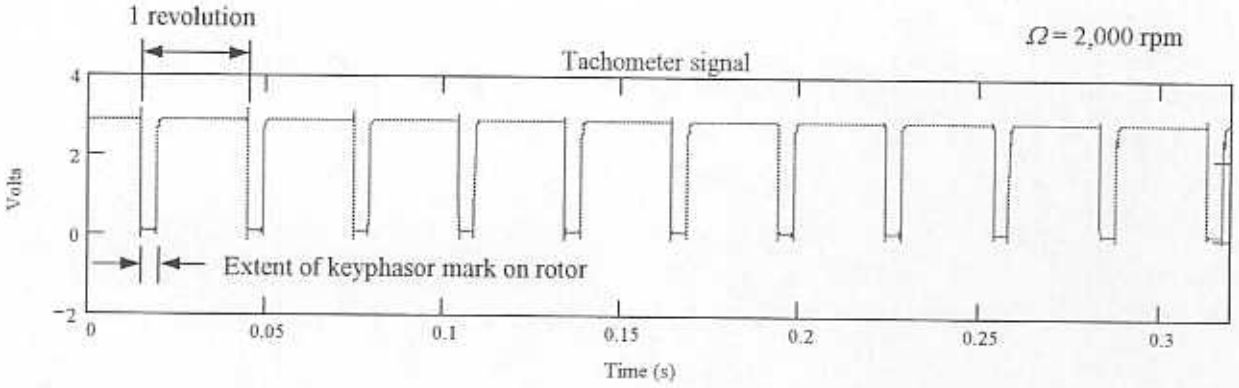

Figure 10. Tachometer signal recorded during an impact load delivered in the horizontal direction. Sampling frequency: 12.8 ksamples/s. $\Delta t = 7.8 \times 10^{-5}$ s. Register size: 4,096 points.

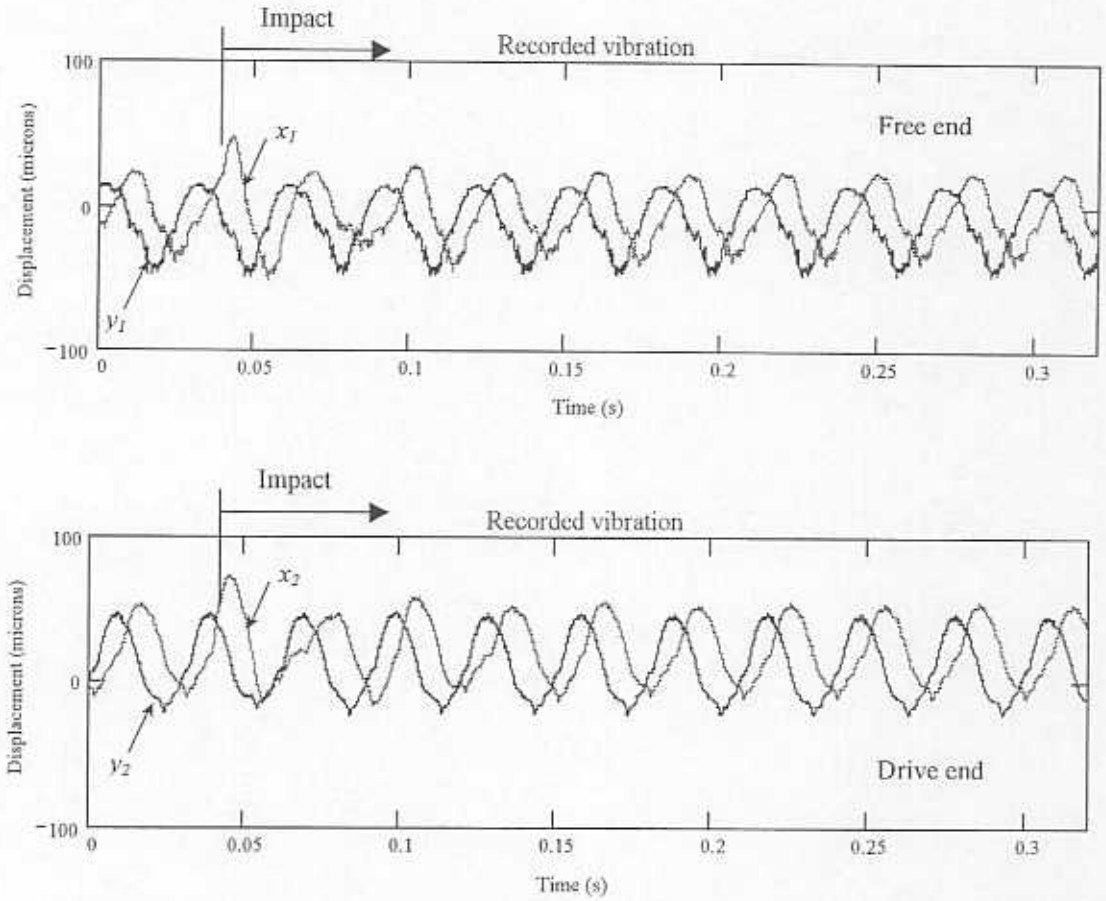

Figure 11. Original vibration signals recorded for an impact in the horizontal (x) direction. Rotor speed: 2,000 rpm. Pre-trigger time: 39 ms (1.3 revolutions). Top: free end bearing, bottom: drive end bearing.

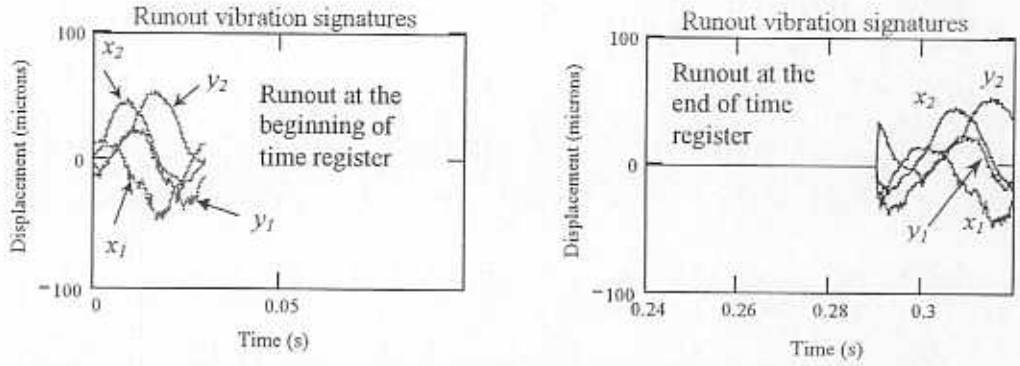

Figure 12. Runout vibration signatures corresponding to one revolution identified at the beginning and at the end of the time records.

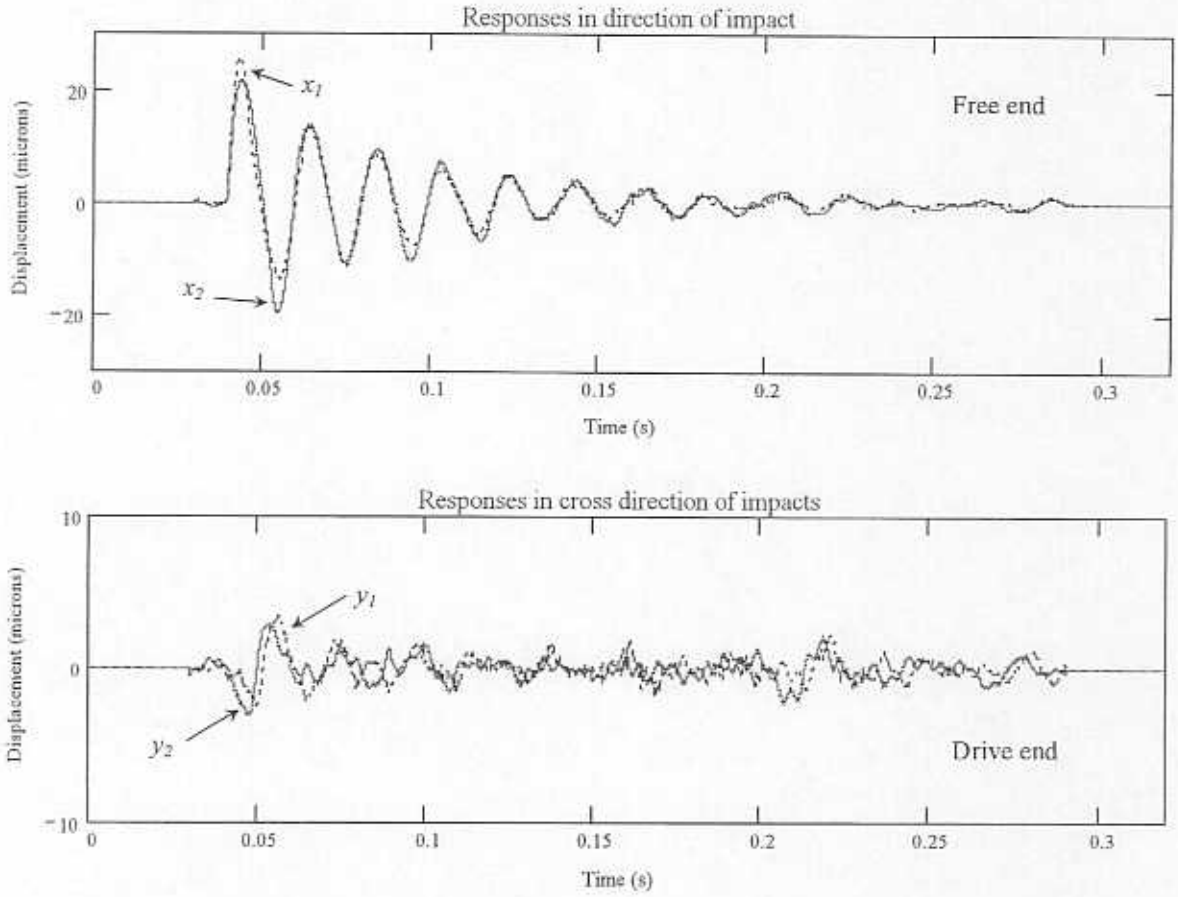

Figure 13. Filtered signals showing dynamic response to impact in the horizontal (x) direction. Top: free end bearing, bottom: drive end bearing.

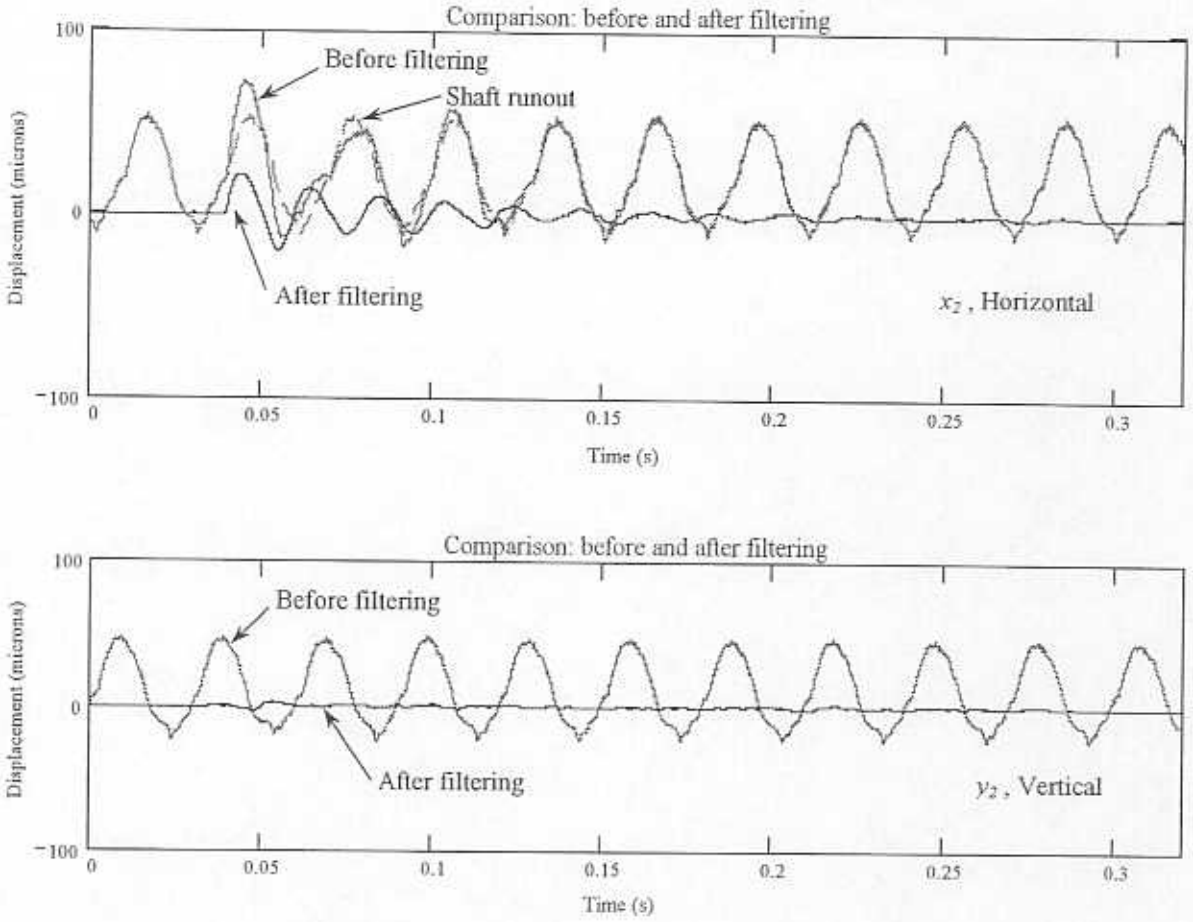

Figure 14. Comparisons between filtered and unfiltered vibration signals. Rotor speed: 2,000 rpm. Top: horizontal, bottom: vertical.

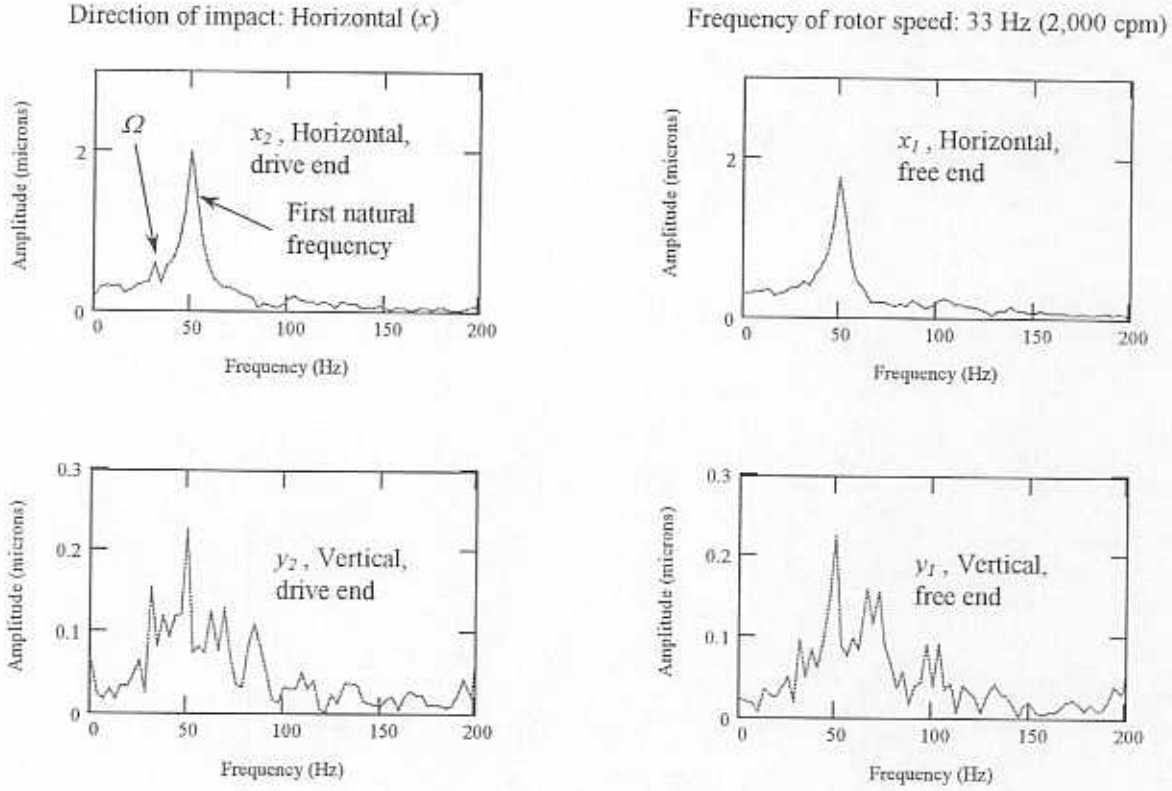

Figure 15. Frequency response functions generated with filtered signals in time domain. Impact in horizontal (x) direction at rotor middle disk. Note different scales for direct and cross-coupled motions.

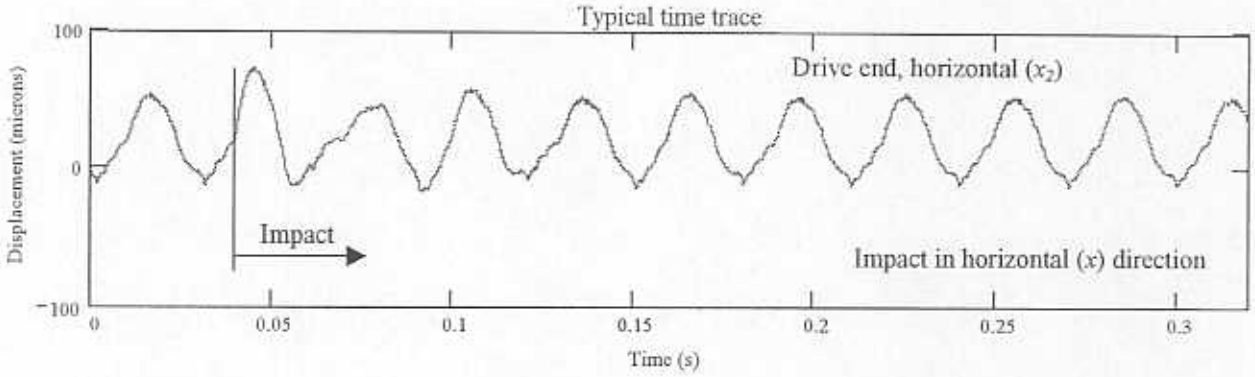

Figure 16. Time register of rotor vibration after impact. Rotor speed: 2,000 rpm.

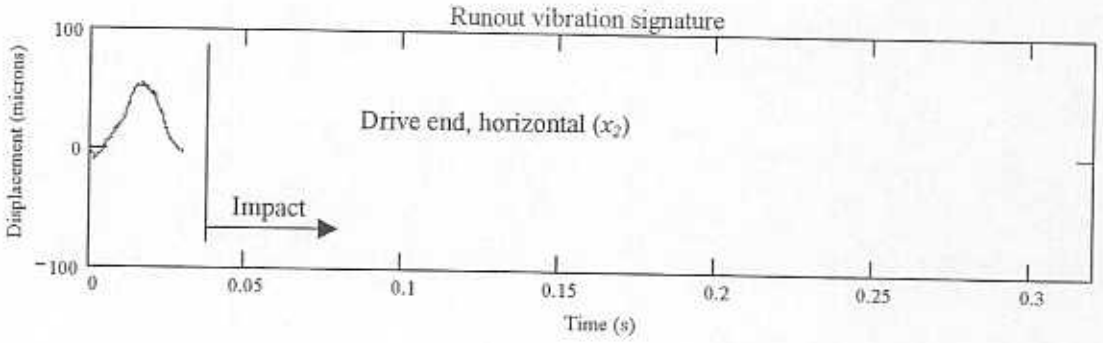

Figure 17. Identified shaft runout and remnant imbalance vibration signature of rotor at drive end, horizontal location (x_2).

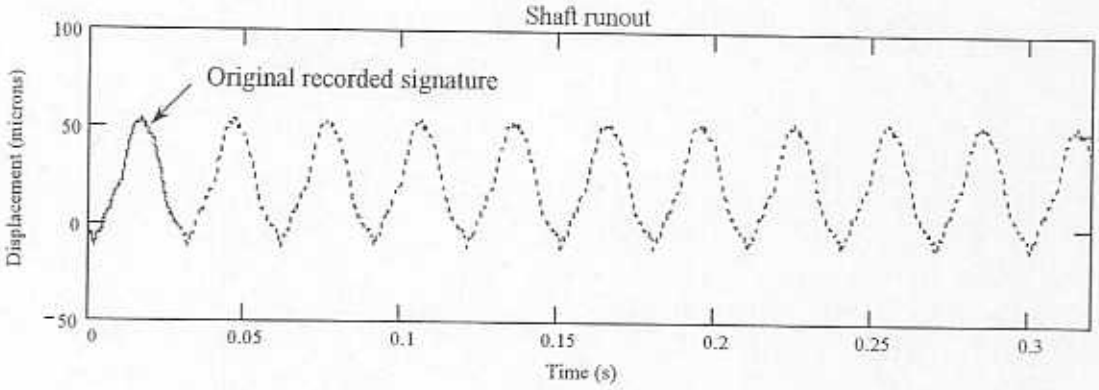

Figure 18. Estimated runout and remnant imbalance vibration of rotor for the entire time register at drive end, horizontal location (x_2).

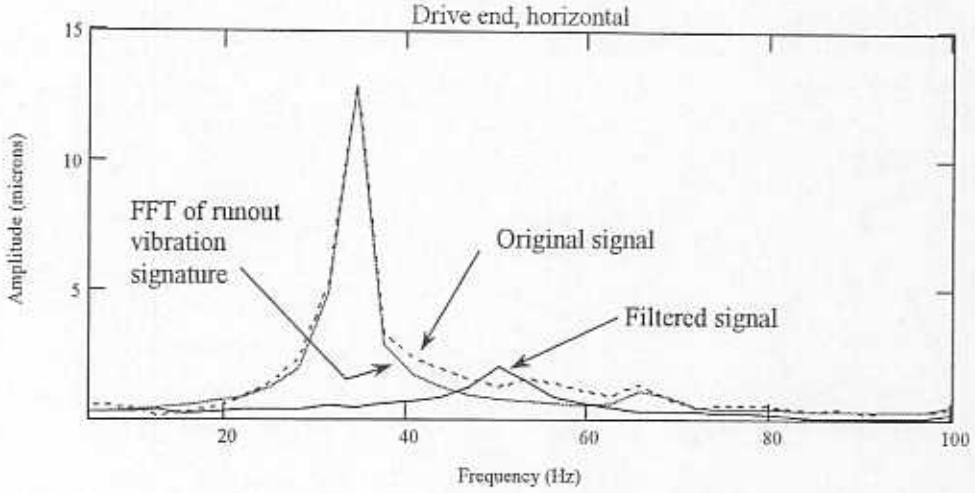

Figure 19. FFT of vibration signals before and after frequency-based filtering at drive end, horizontal location (x_2).

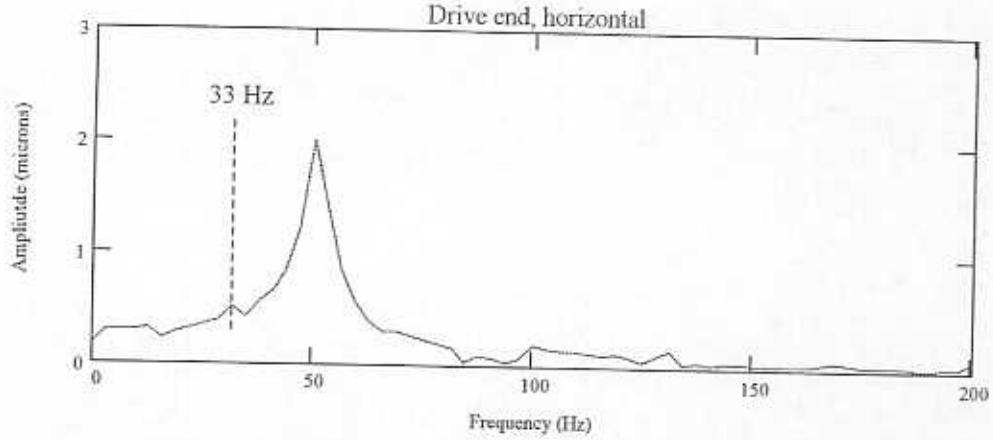

Figure 20. Spectrum of filtered signal in the frequency domain resulting of an impact in the horizontal direction. Drive end, horizontal location (x_2). Rotor speed: 2,000 rpm (33 Hz).

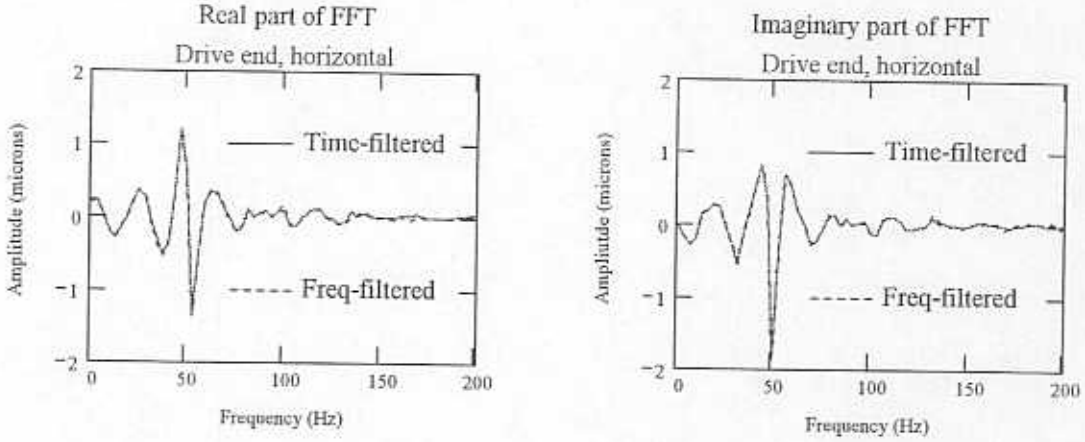

Figure 21. Comparison of real and imaginary parts of spectra for time-filtered and frequency-filtered signals. Drive end, horizontal location (x_2). Rotor speed: 2,000 rpm (33 Hz).

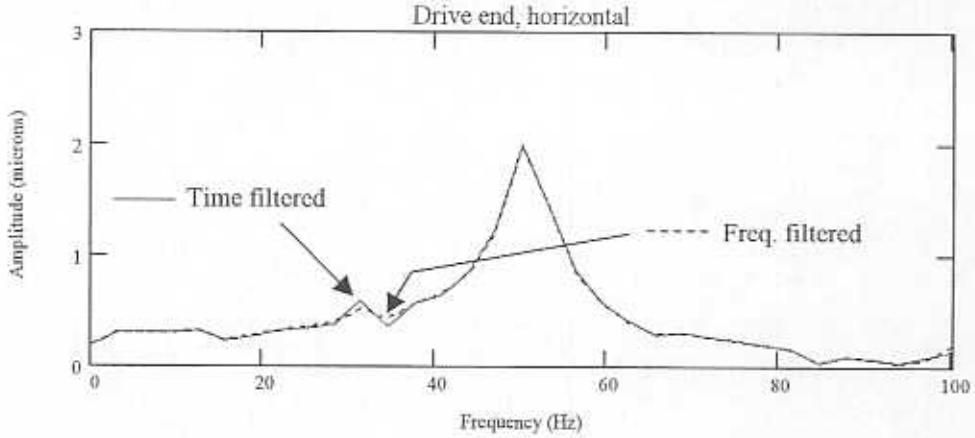

Figure 22. Comparison of frequency component amplitudes for time-filtered and frequency-filtered signals. Drive end, horizontal location (x_2). Rotor speed: 2,000 rpm (33 Hz).

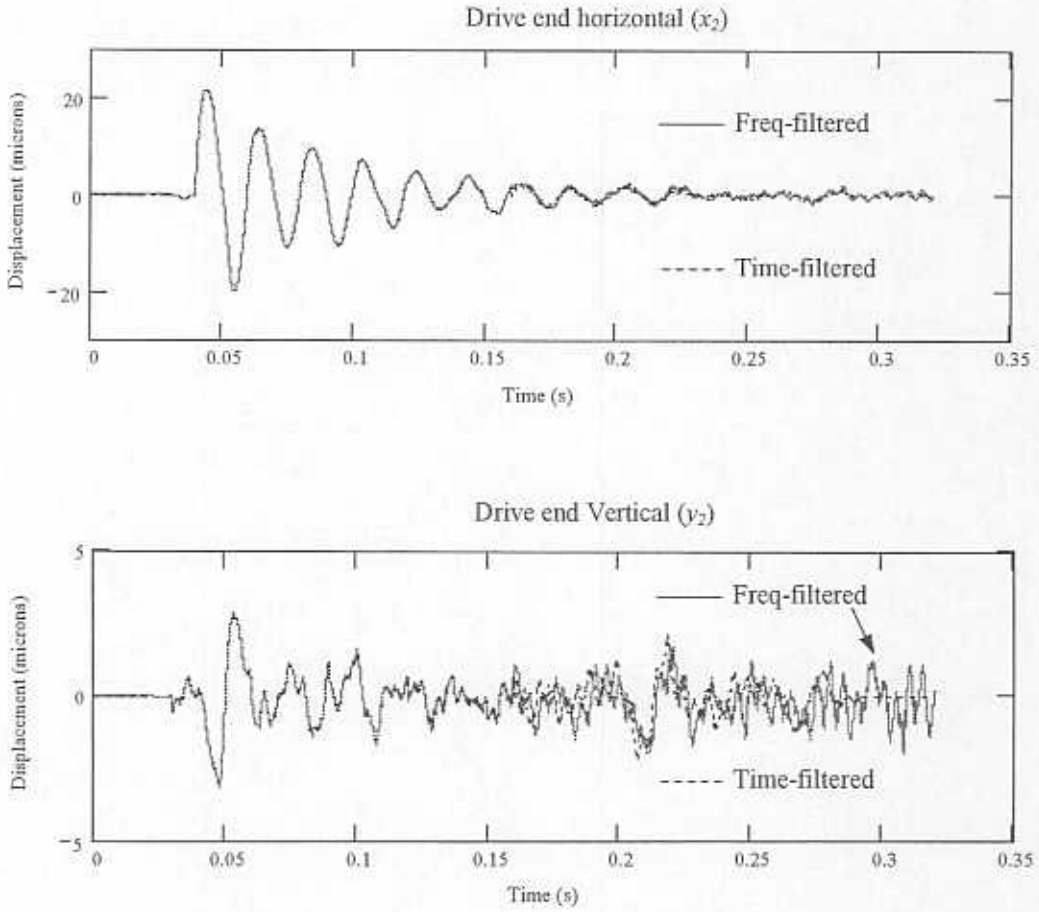

Figure 23. Recovered time response from filtered signal by inverse FFT in direction of impact (x) and in cross direction from impact (y). Rotor speed: 2,000 rpm. Notice different scales for motions in the (x) and (y) directions.

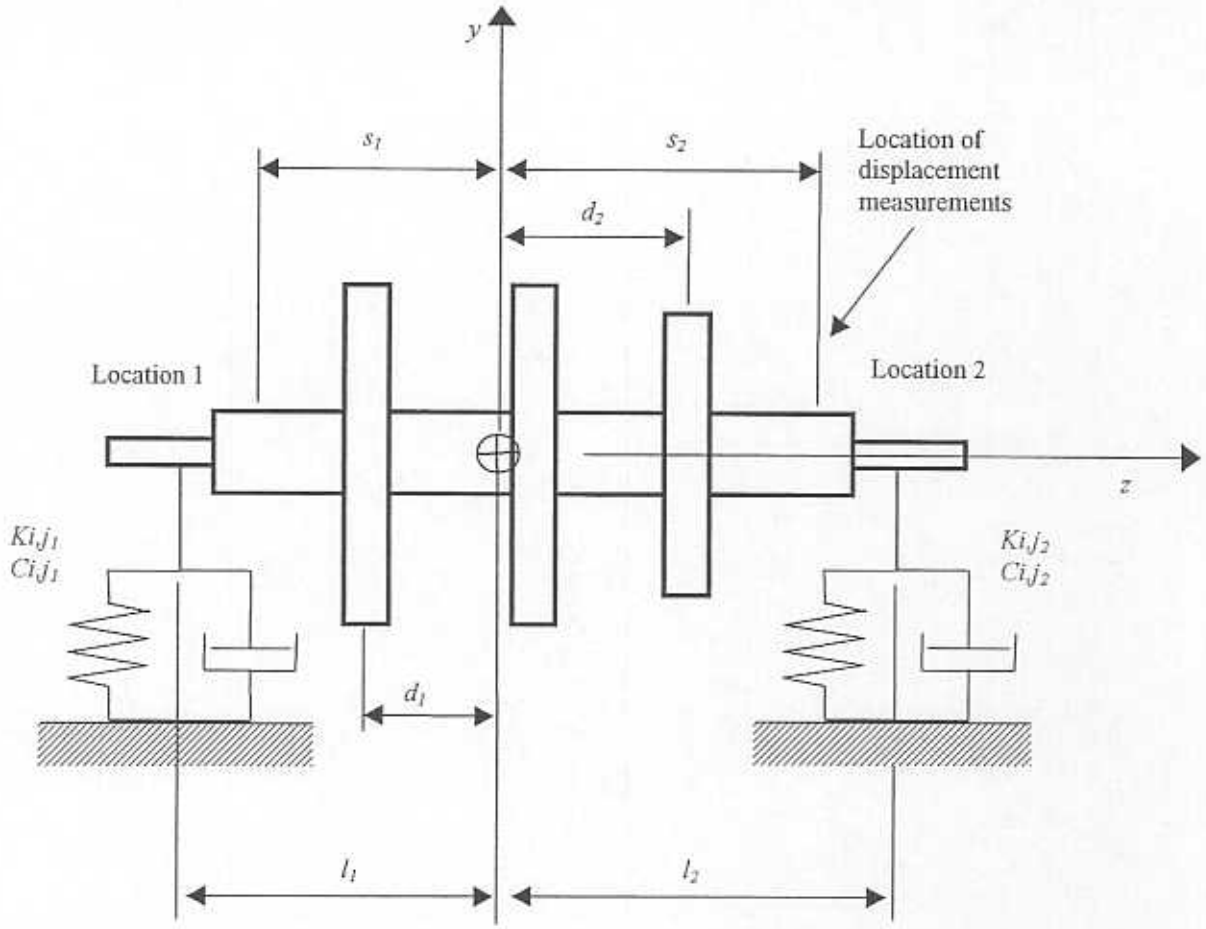

Figure 24. Rotor model for identification of equivalent support parameters.

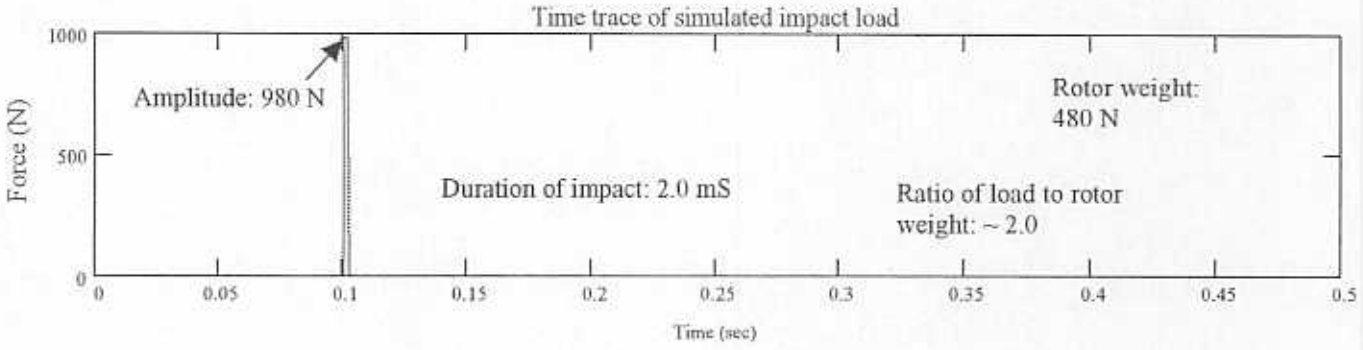

Figure 25. Impact load applied to test rotor in horizontal direction (x) for numerical experiment.

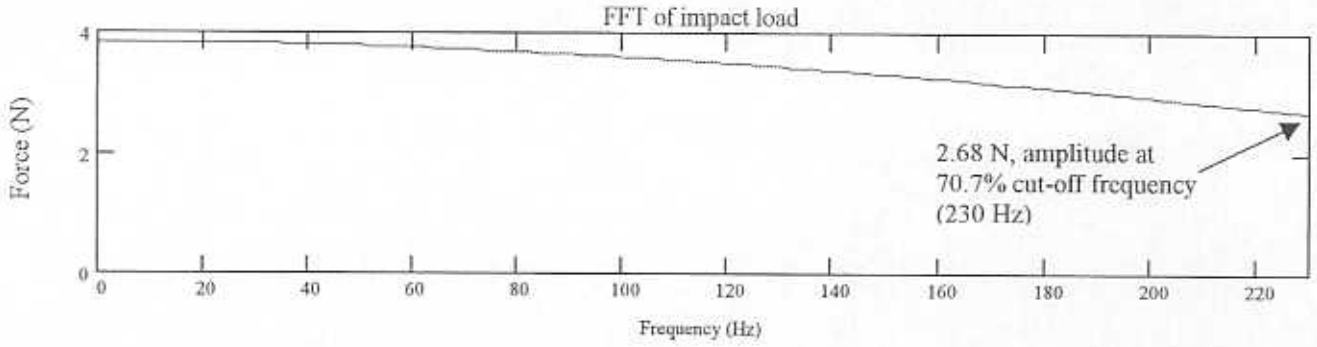

Figure 26. Time and frequency representation of impact load (980 N, 2.0 ms duration). Impact in (x) direction (horizontal).

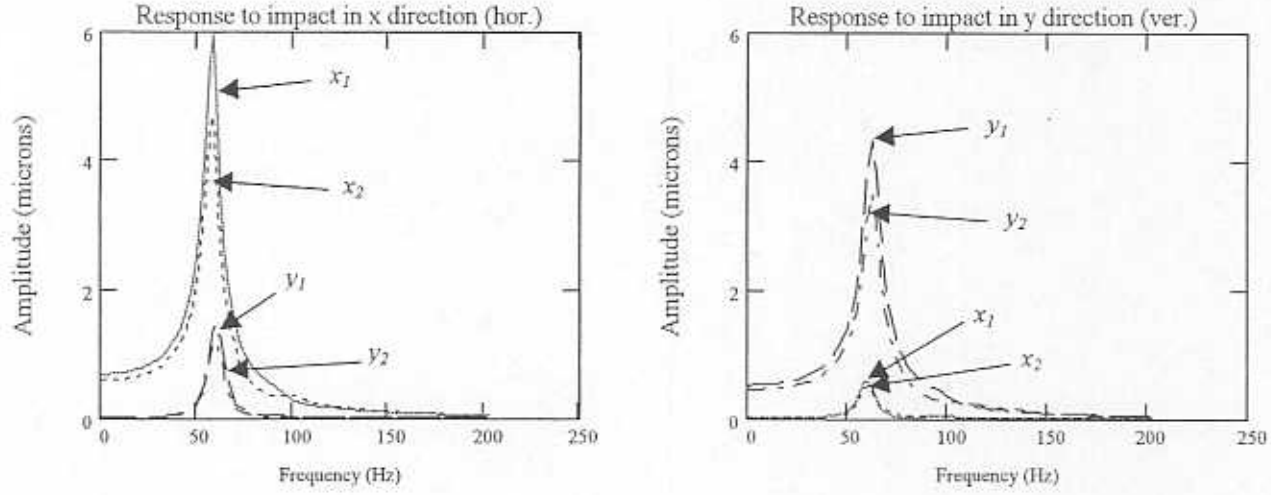

Figure 27. Predicted response of rotor model at bearing locations from impact loads in horizontal (x) and vertical (y) directions.

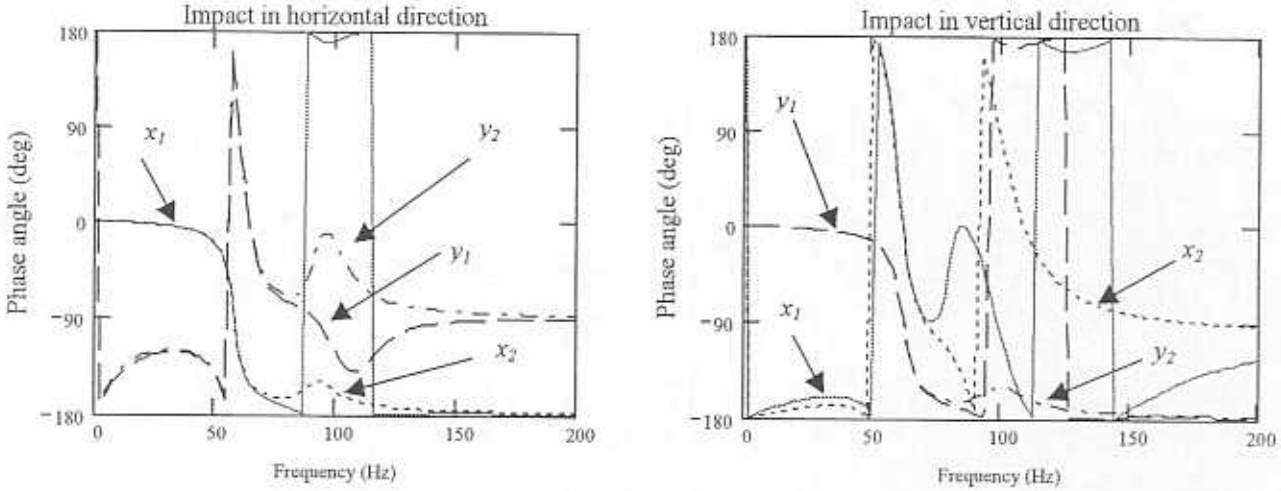

Figure 28. Phase angles of predicted rotor response at bearing locations from impact loads in horizontal (x) and vertical (y) directions.

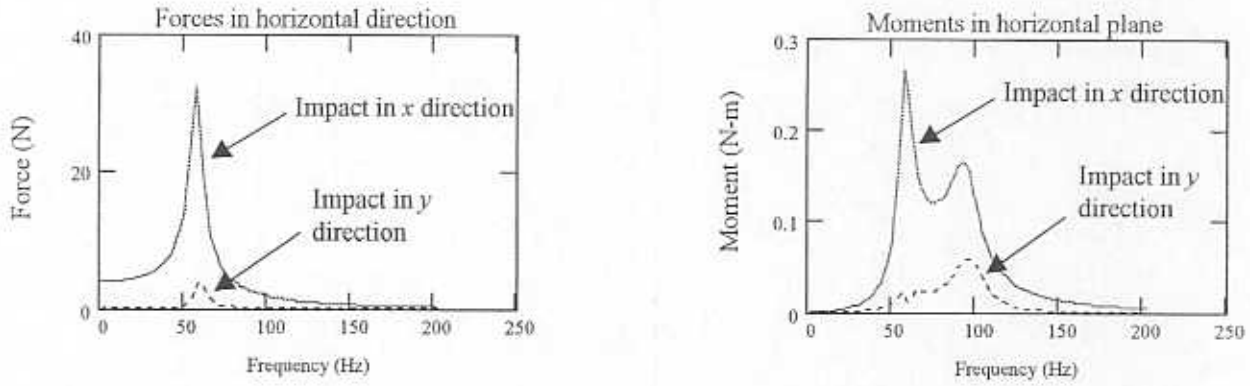

Figure 29. Total force and excitation moments applied at the rotor center of gravity in the (x-z) plane including impact and inertia effects as a function of the frequency.

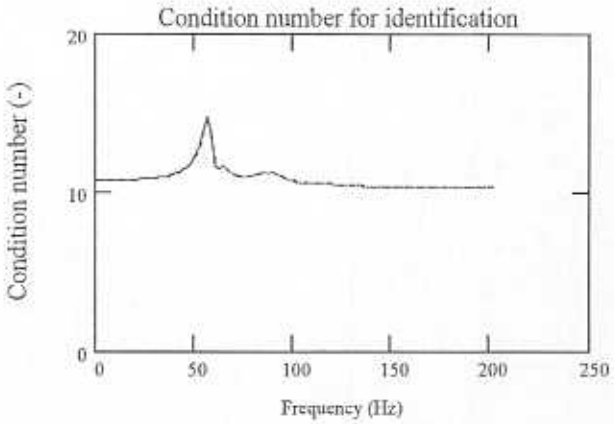

Figure 30. Condition number of identification matrices $\overline{Q}^x$ and $\overline{Q}^y$ as a function of the frequency (Numerical example).

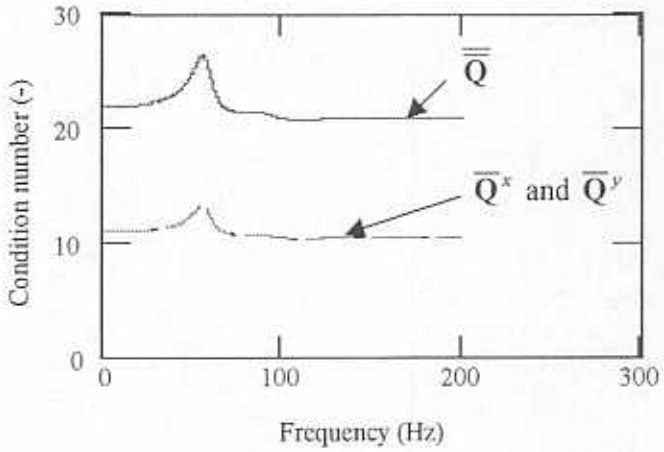

Figure 31. Comparison of condition numbers (based on Euclidean norm) of identification matrices of two different algebraic formulations (equations 16 and 26).

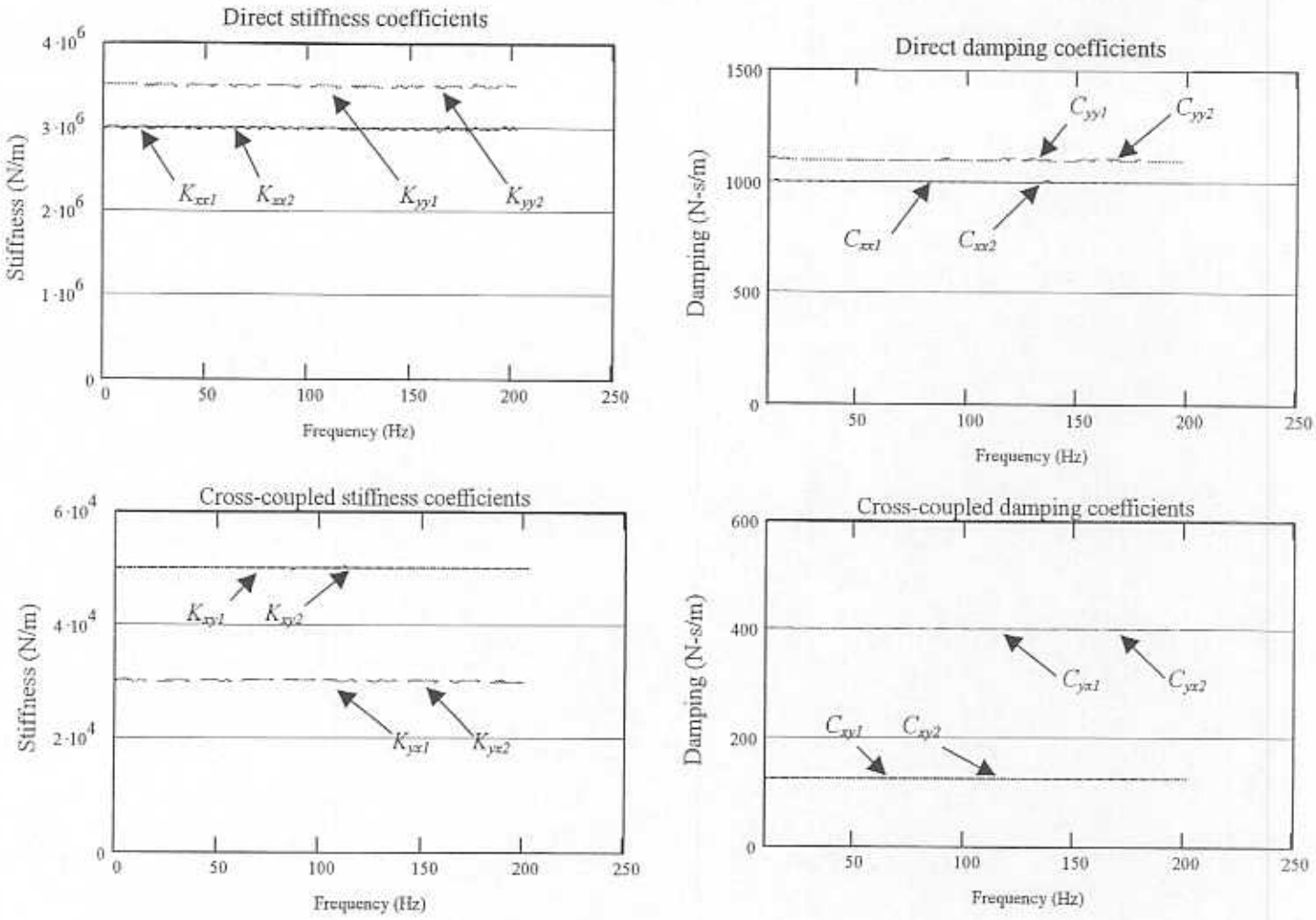

Figure 32. Identified bearing parameters as a function of excitation frequency. Results of numerical experiment.

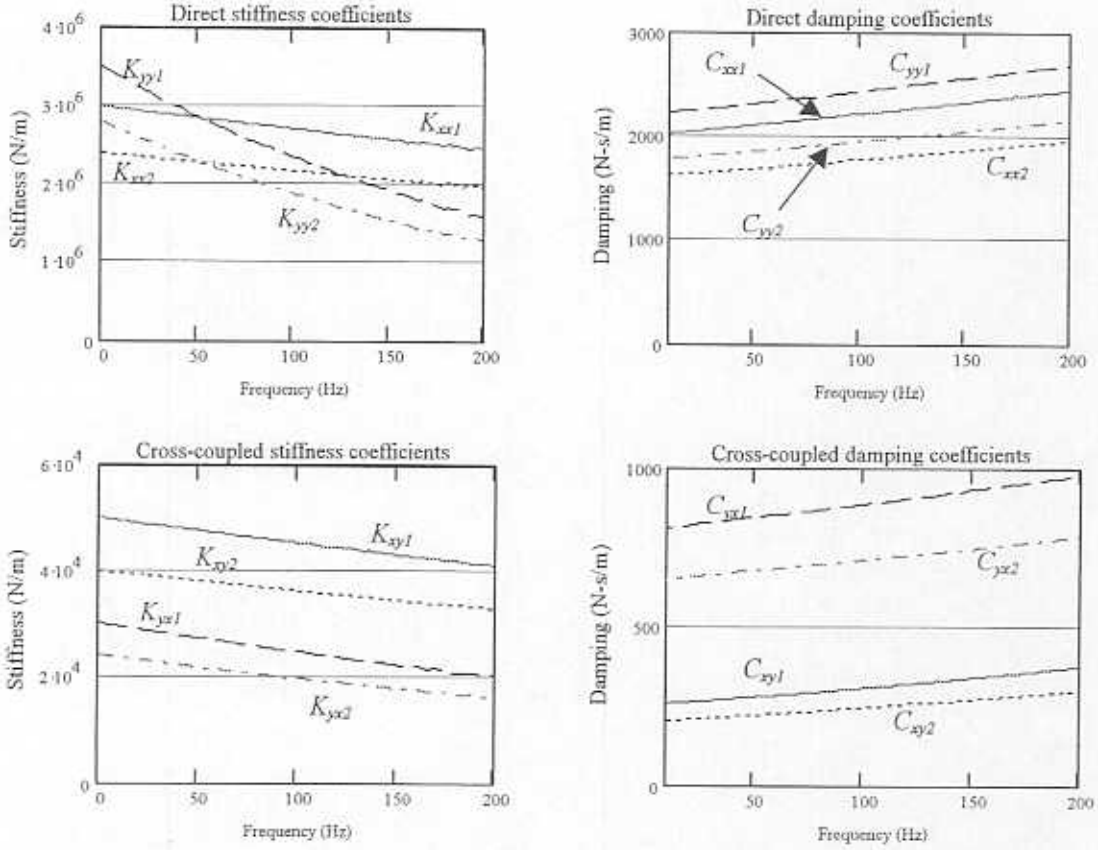

Figure 33. Identified bearing parameters as a function of excitation frequency for second numerical example (frequency dependent force coefficients).

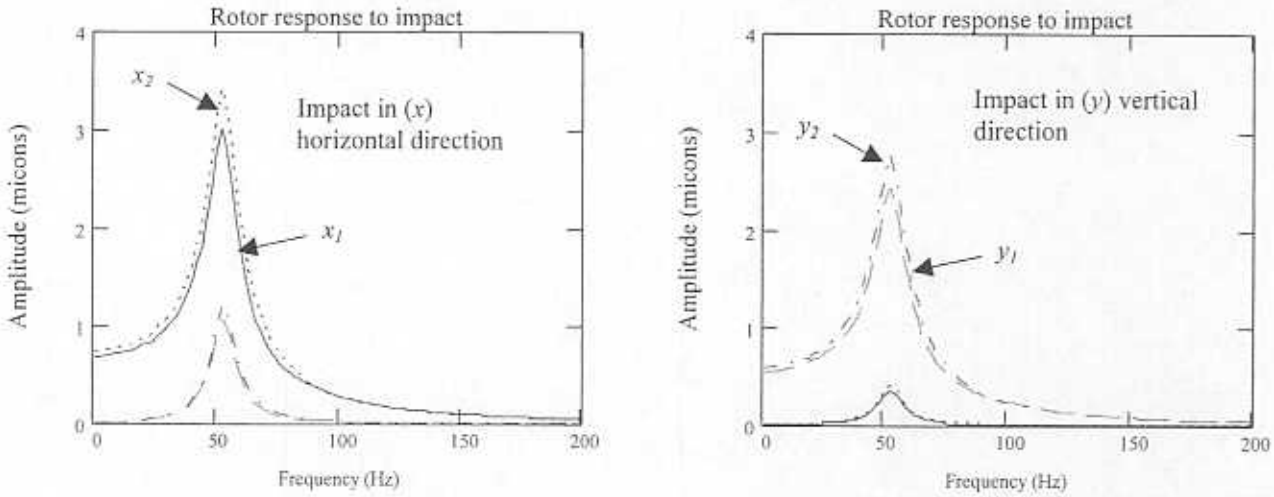

Figure 34. Numerical response of rotor with 2% noise.

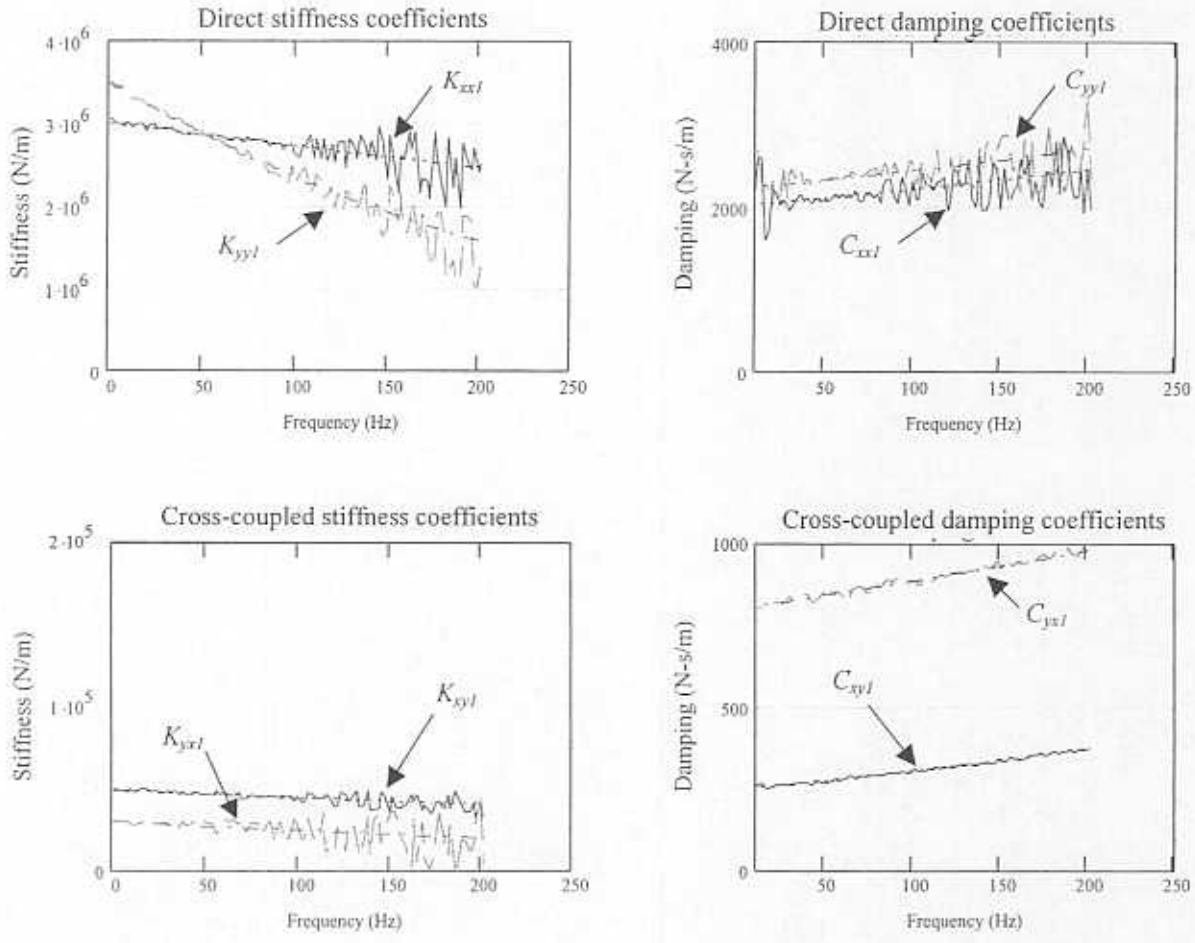

Figure 35. Identification of frequency-dependent force coefficients from numerical response with 2% noise.

(x) direction

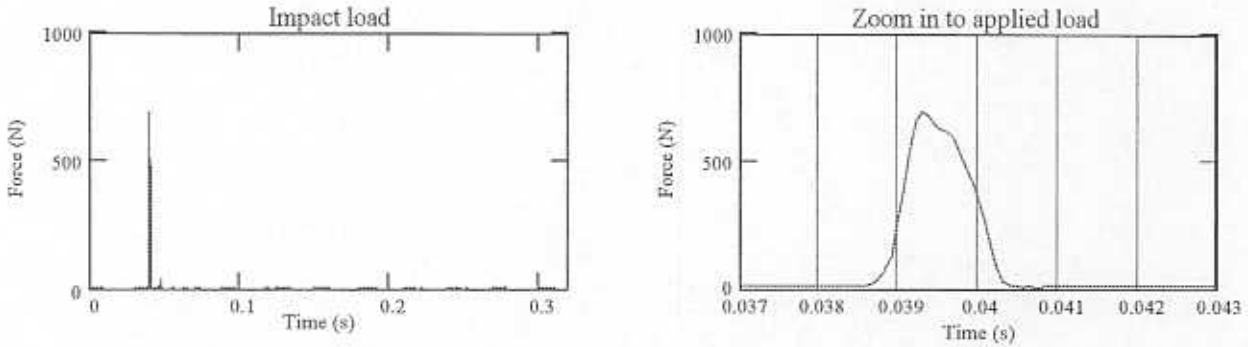

Period of rotation: 30.0 mS

(y) direction

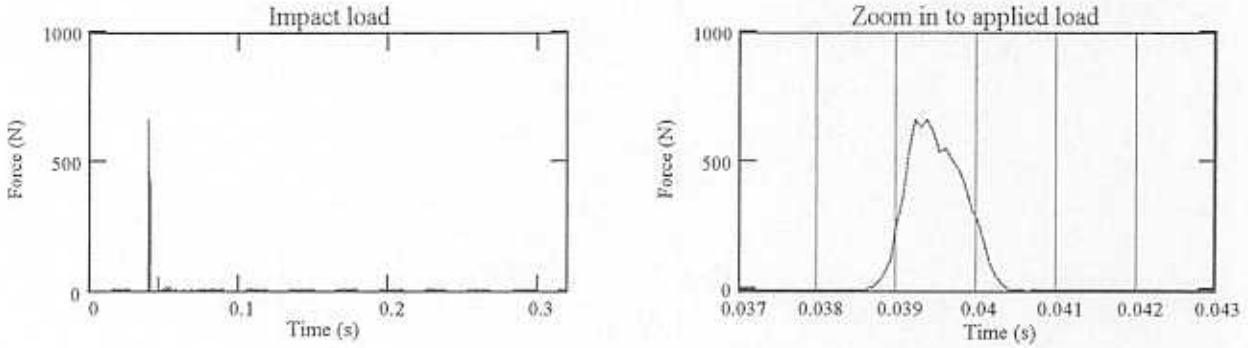

Figure 36. Time representation (record) of experimental impact loads applied to the test rotor in horizontal (x) and vertical (y) directions. Rotor speed: 2,000 rpm.

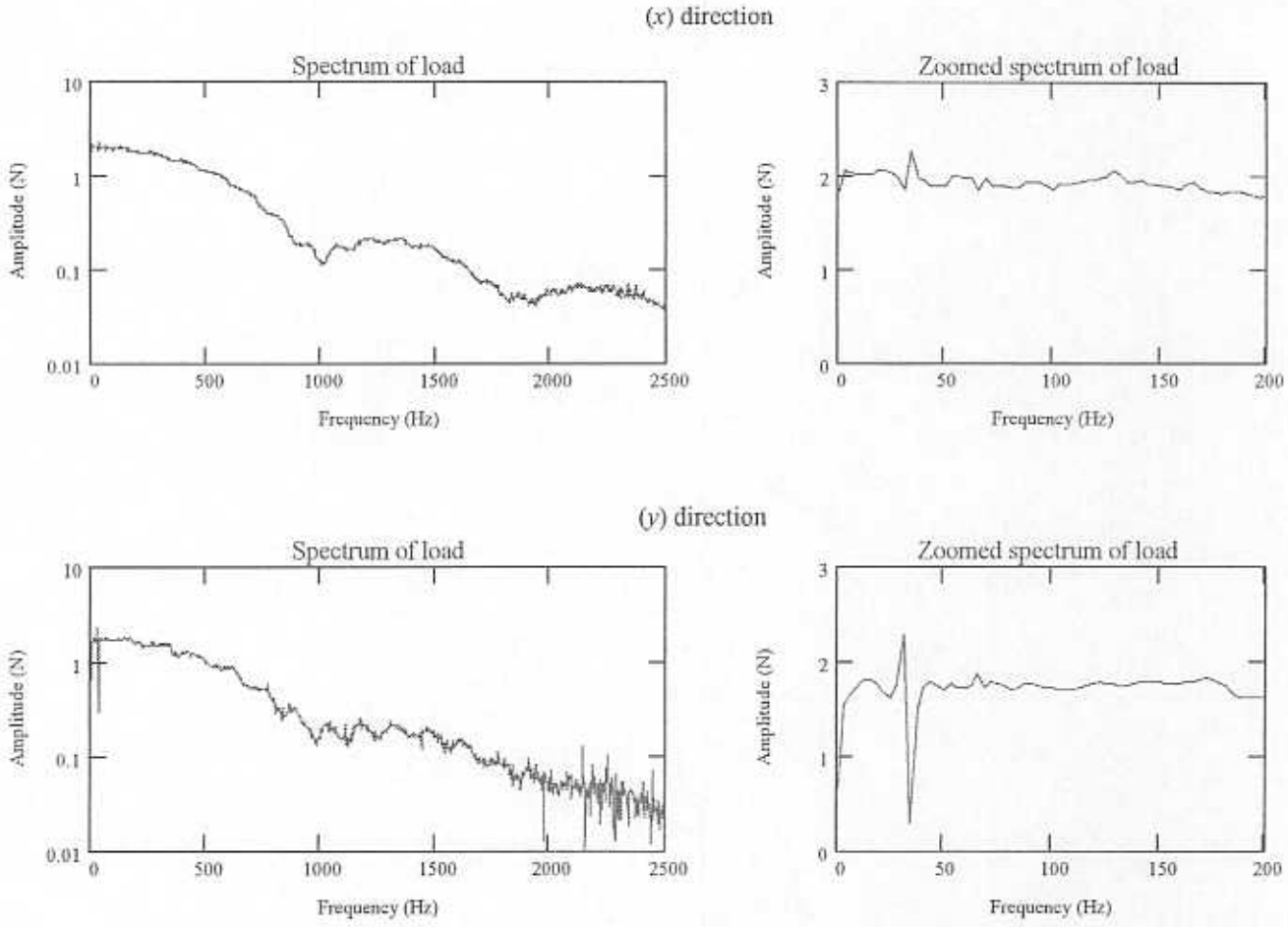

Figure 37. Frequency spectrum (amplitude) of experimental impact loads applied to the test rotor in horizontal (x) and vertical (y) directions. Rotor speed: 2,000 rpm (33.3 Hz).

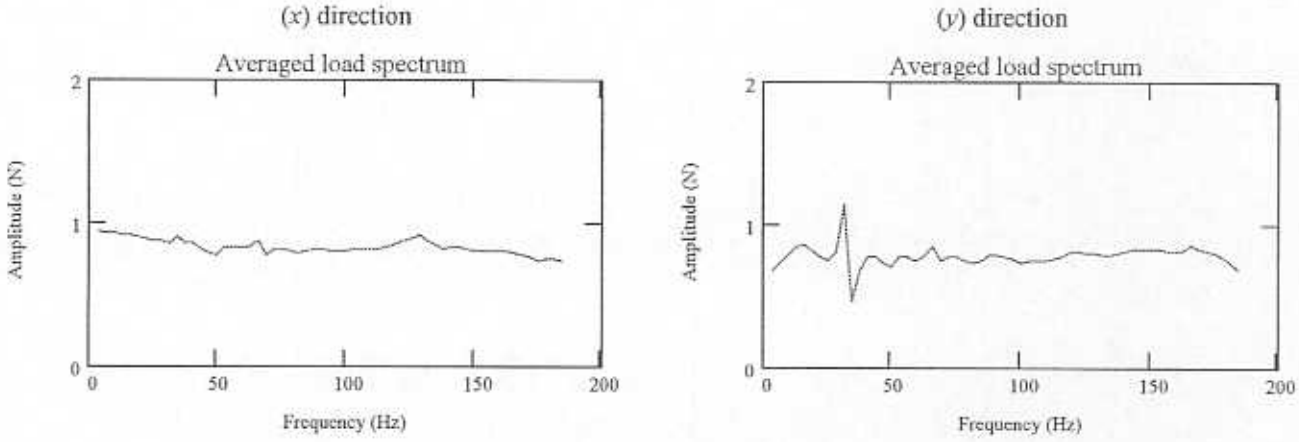

Figure 38. Amplitude of averaged spectra of 5 consecutive impacts applied to the test rotor in each orthogonal direction (*x*, horizontal and *y*, vertical). Rotor speed: 2,000 rpm (33.3 Hz).

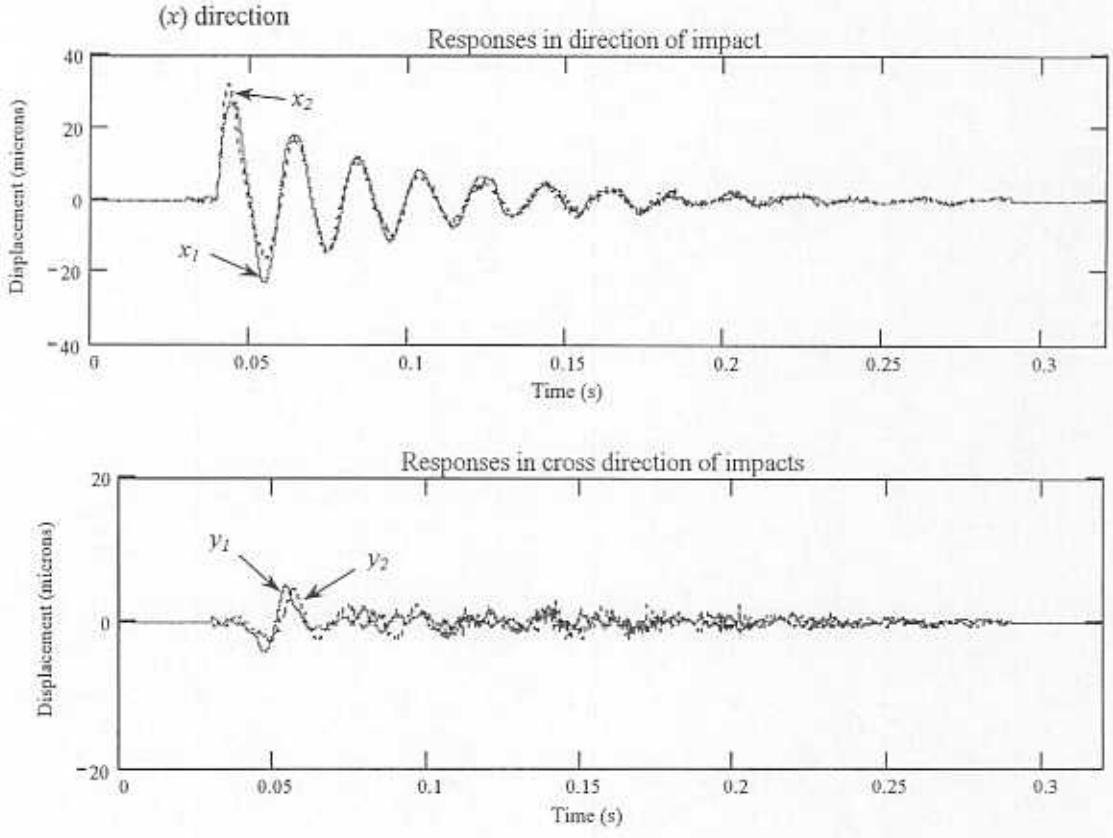

Figure 39a. Experimental rotor responses at measurement locations (s_1, s_2) after shaft runout subtraction. Impact in *x* direction. Applied load: 690 N, ~ 1.5 ms. Rotor speed: 2,000 rpm (33.3 Hz).

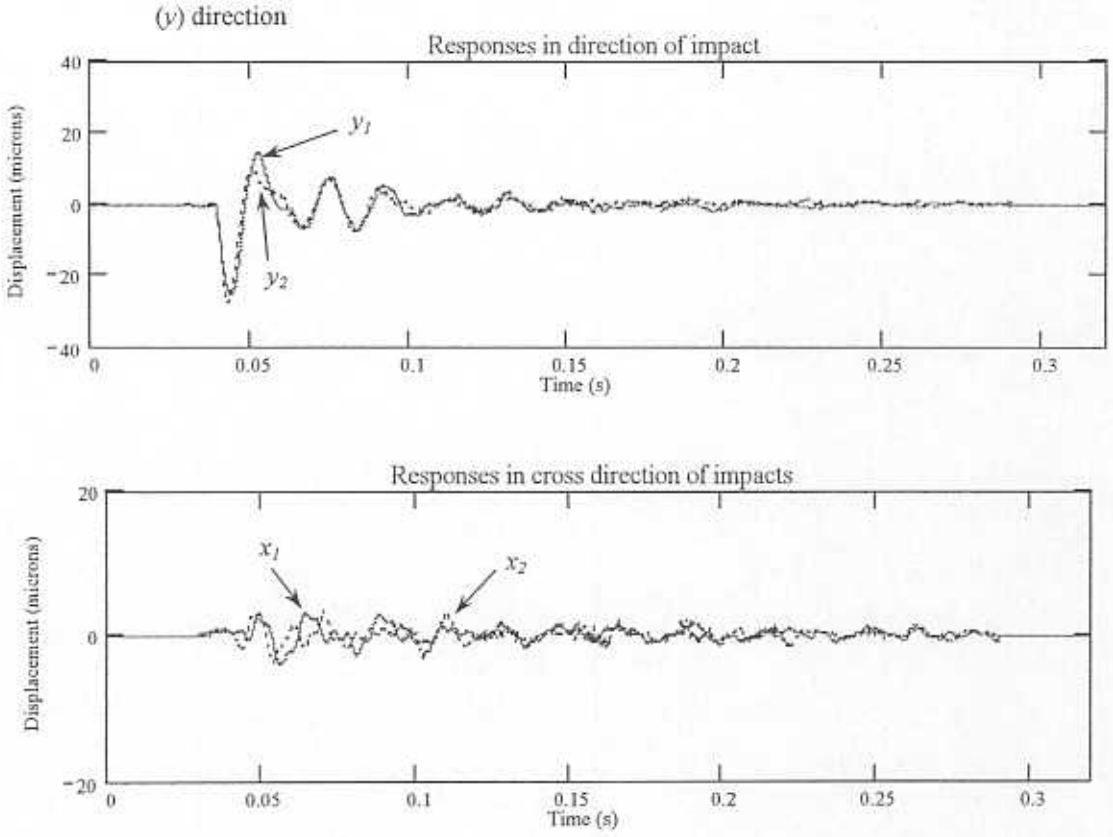

Figure 39b. Experimental rotor responses at measurement locations (s_1, s_2) after shaft runout subtraction. Impact in y direction. Applied load: 712 N, ~ 1.3 ms. Rotor speed: 2,000 rpm (33.3 Hz).

Impact in (x) direction

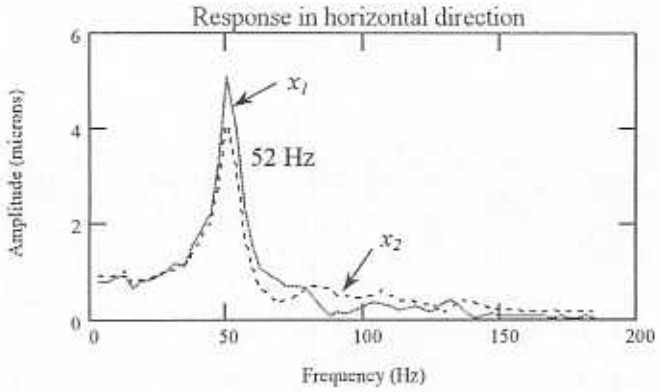

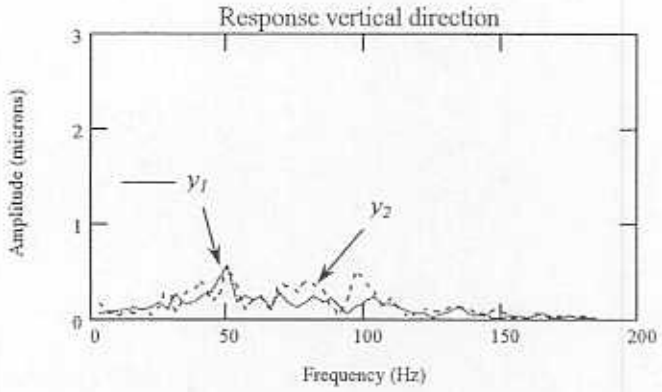

Impact in (y) direction

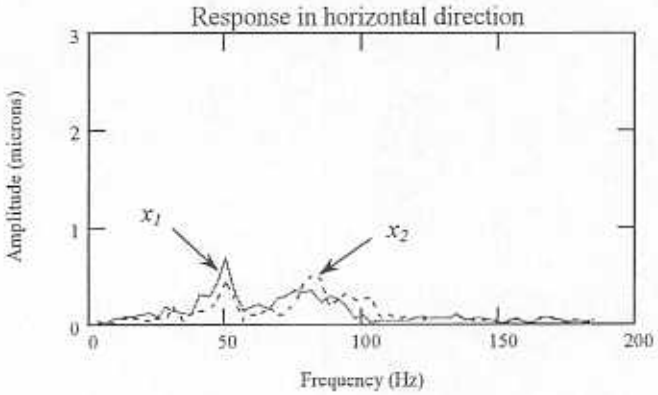

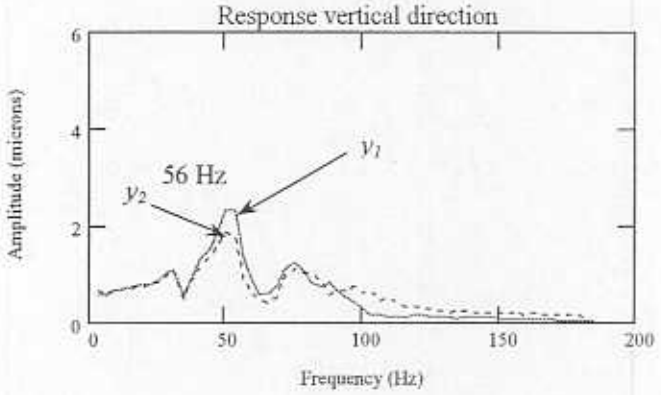

Figure 40. Averaged spectra of rotor response to impact excitation. Five consecutive impacts in each direction delivered at the rotor middle disk. Rotor speed: 2,000 rpm (33.3 Hz).

Location 1, free end bearing

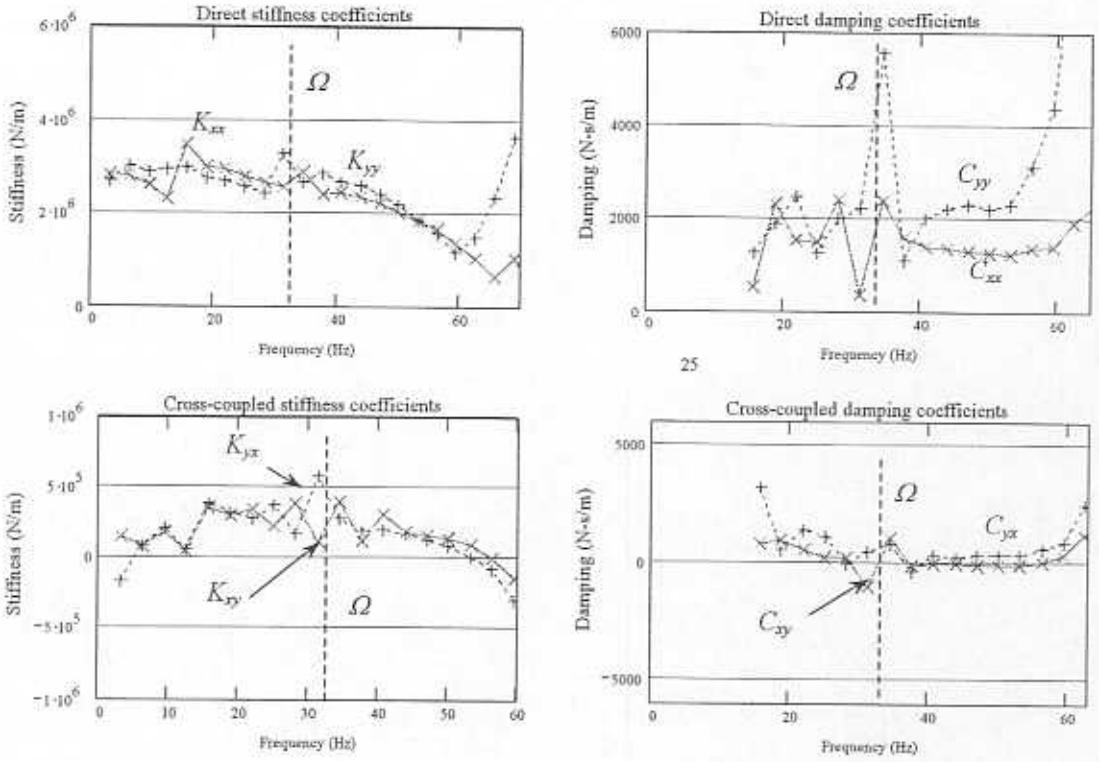

25

Figure 41a. Identified bearing coefficients as functions of the excitation frequency. Free end bearing. Rotor speed: 2,000 rpm (33.3 Hz).

Location 2, drive end bearing

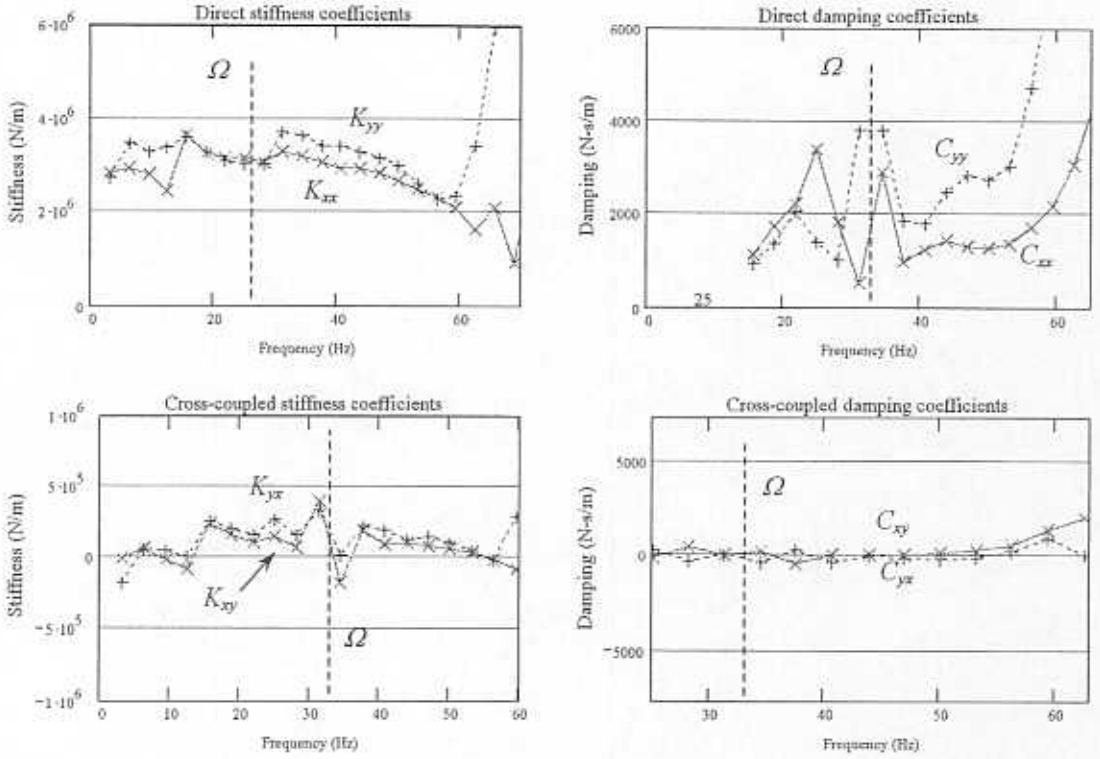

Figure 41b. Identified bearing coefficients as functions of the excitation frequency. Drive end bearing. Rotor speed: 2,000 rpm (33.3 Hz).

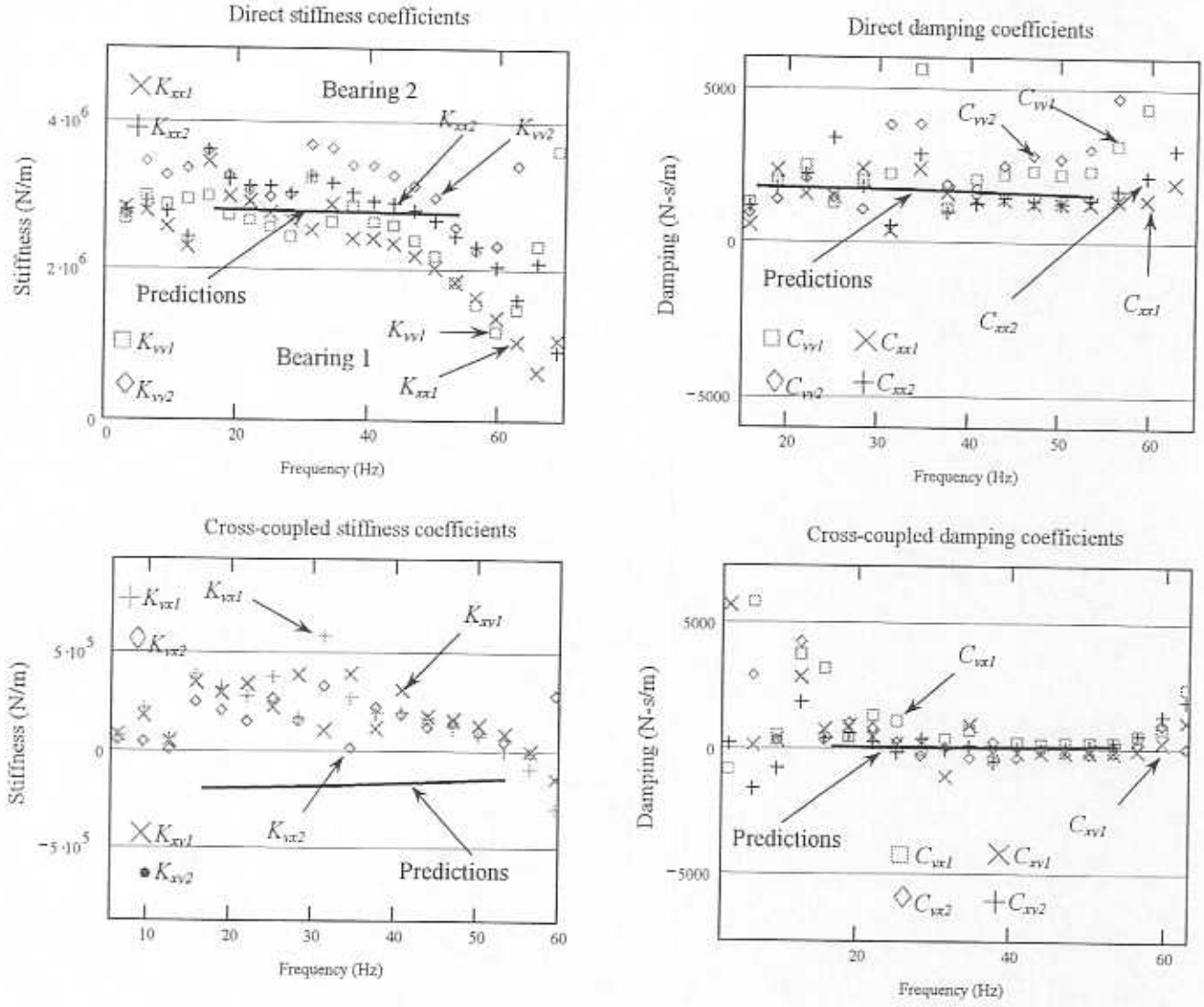

Figure 42. Comparisons of experimental bearing coefficients with model predictions. Rotor speed: 2,000 rpm (33.3 Hz).

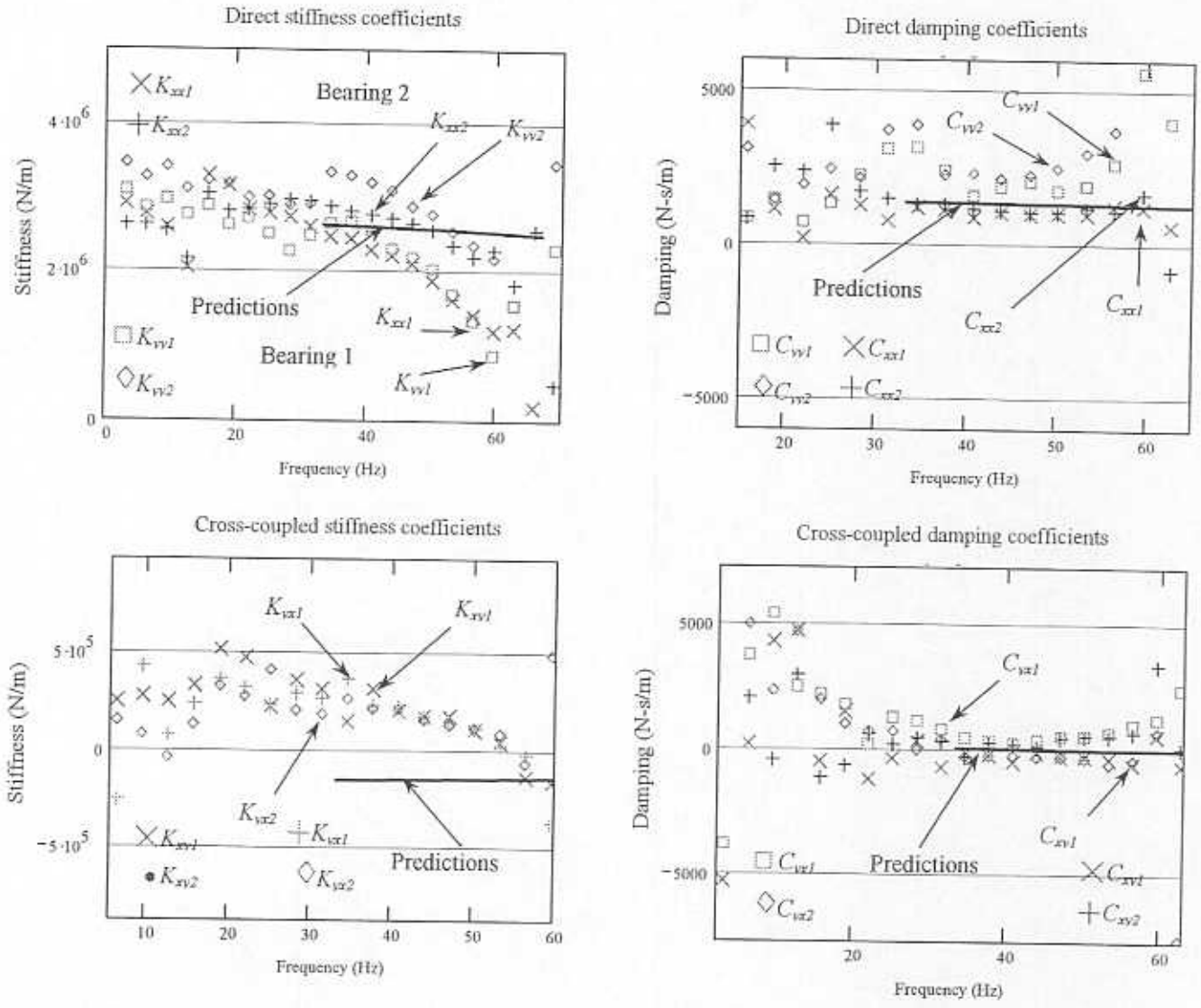

Figure 43. Identified bearing coefficients at 4,000 rpm (66.6 Hz) as a function of excitation frequency and comparisons with model predictions.

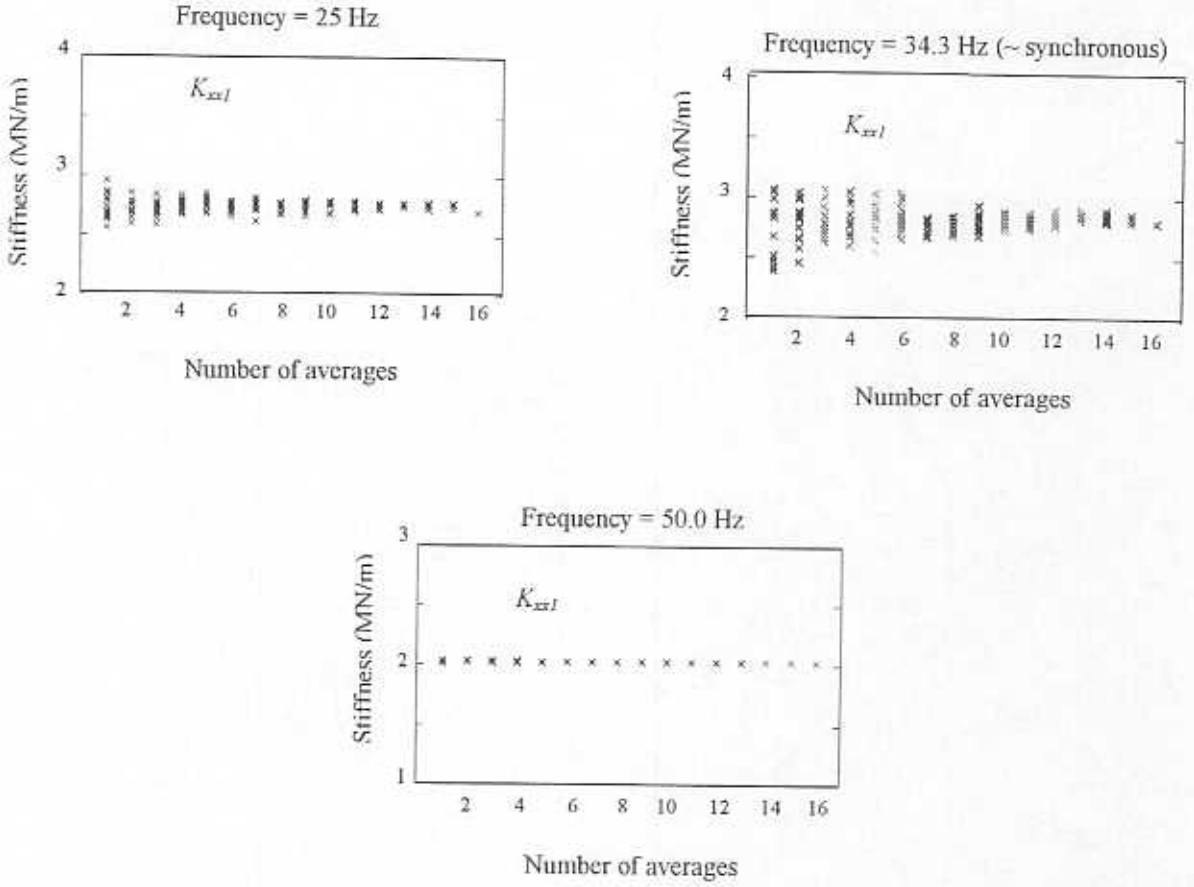

Figure 44. Direct stiffness coefficient (K_{xx1}) identified from impact response experiments as a function of the number of averaged pairs of impacts. Three identification frequencies.

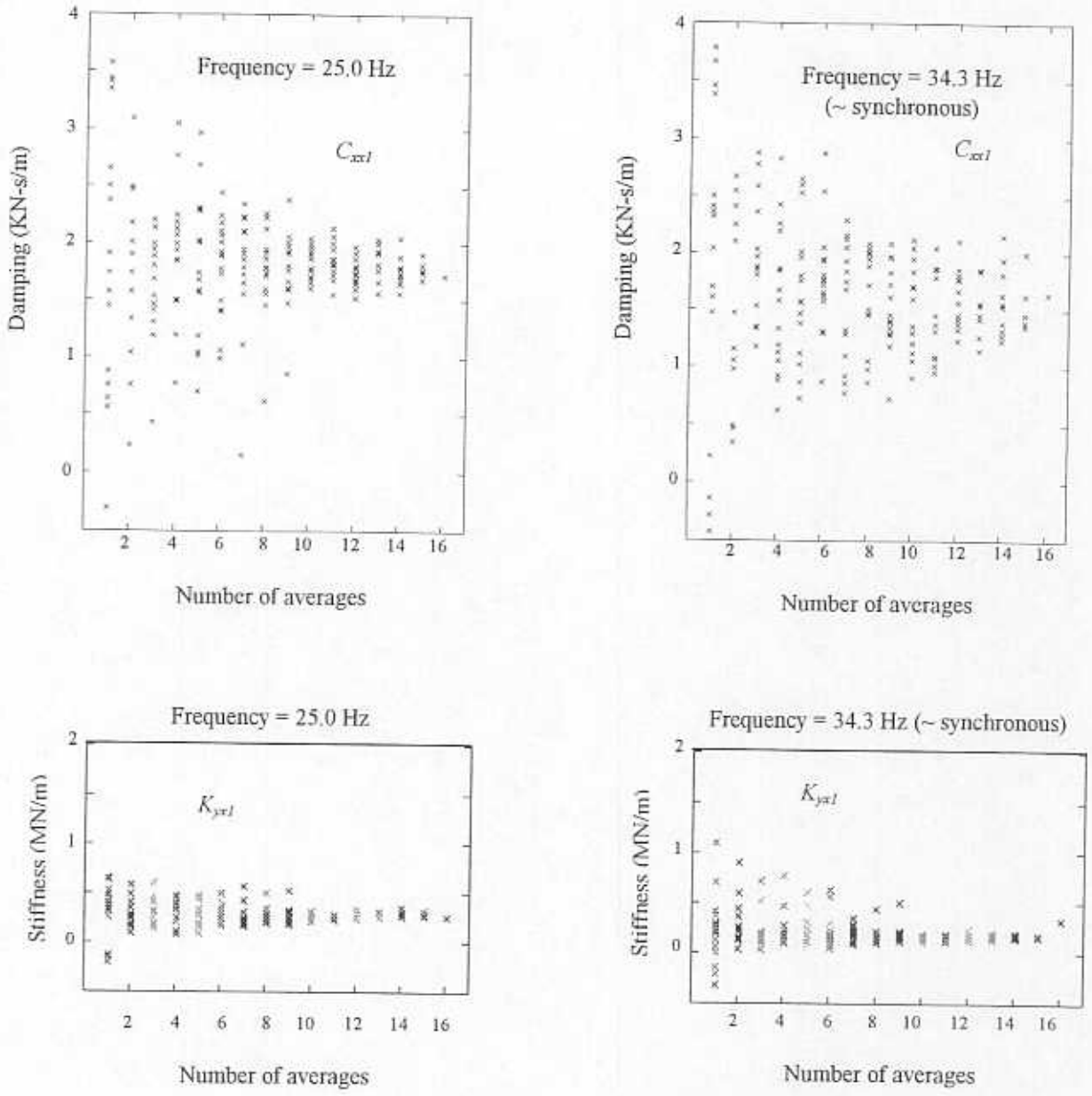

Figure 45. Identified bearing direct damping and cross-coupled stiffness coefficients as a function of number of averages. Low and medium frequencies.

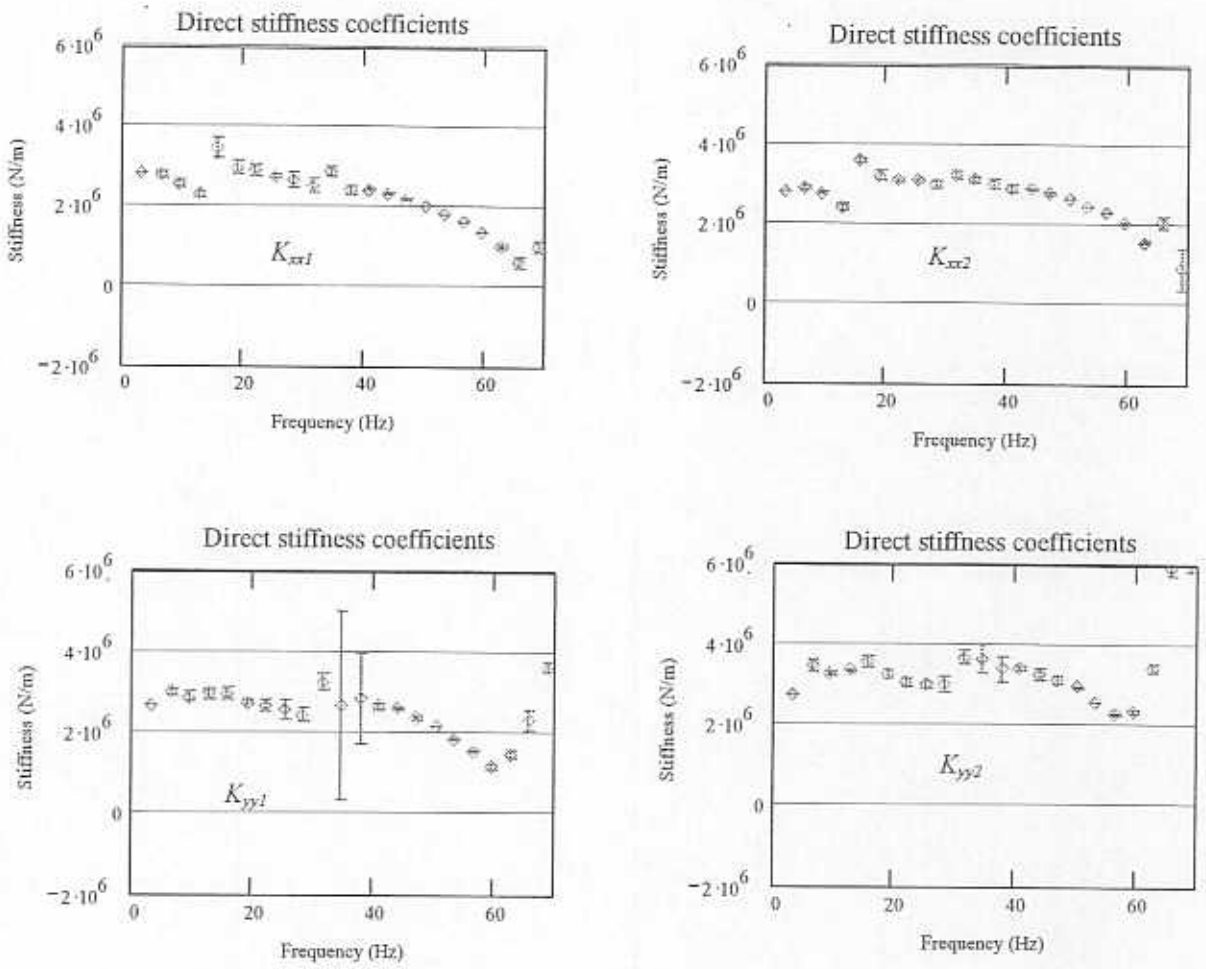

Figure 46a. Average bearing direct stiffness coefficients identified from impact response measurements as a function of the frequency of excitation and depicting the 95% confidence interval. Rotor speed: 2,000 rpm.

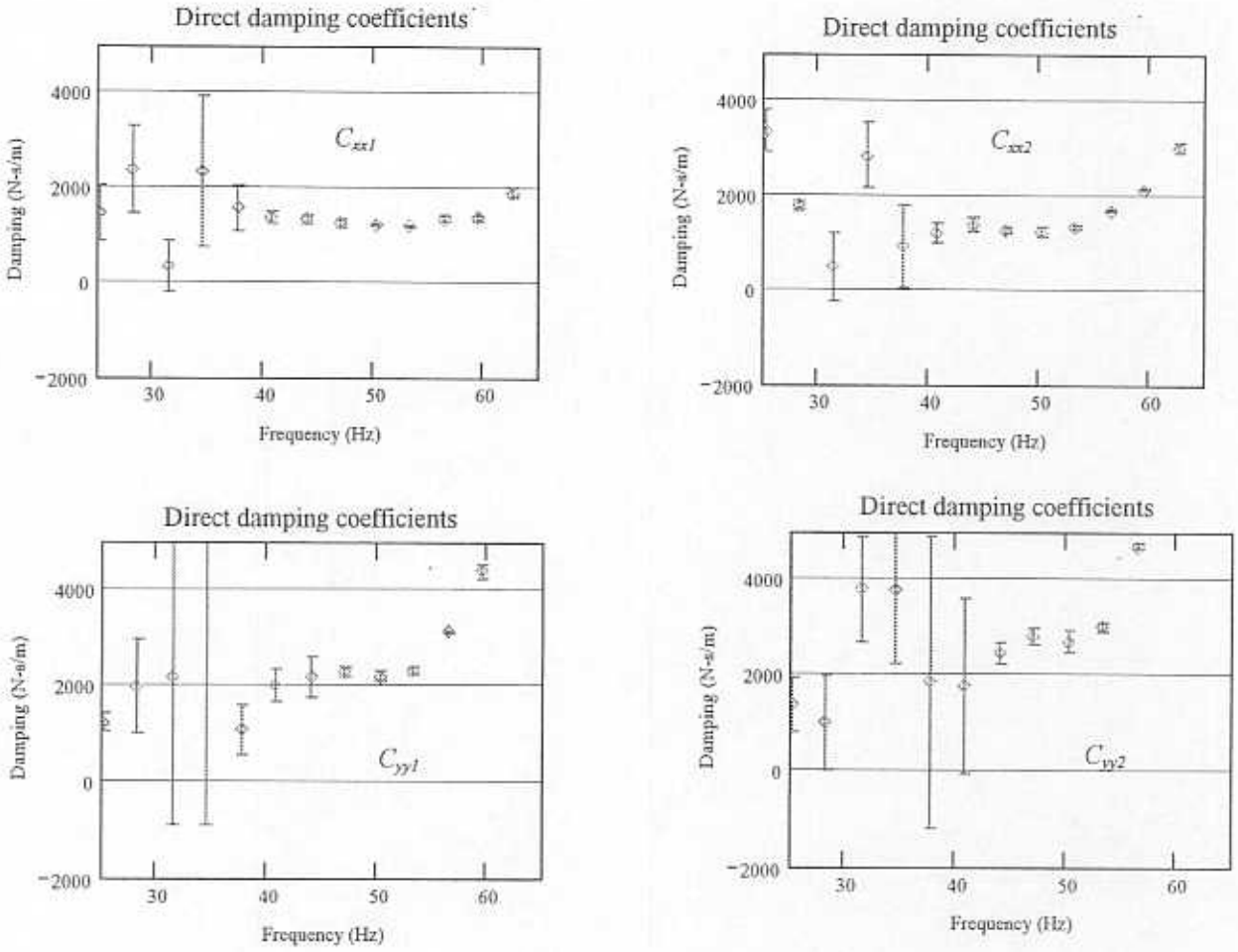

Figure 46b. Average direct damping bearing coefficients identified from impact response measurements as a function of the frequency of excitation and depicting the 95% confidence interval. Rotor speed: 2,000 rpm. (continued)

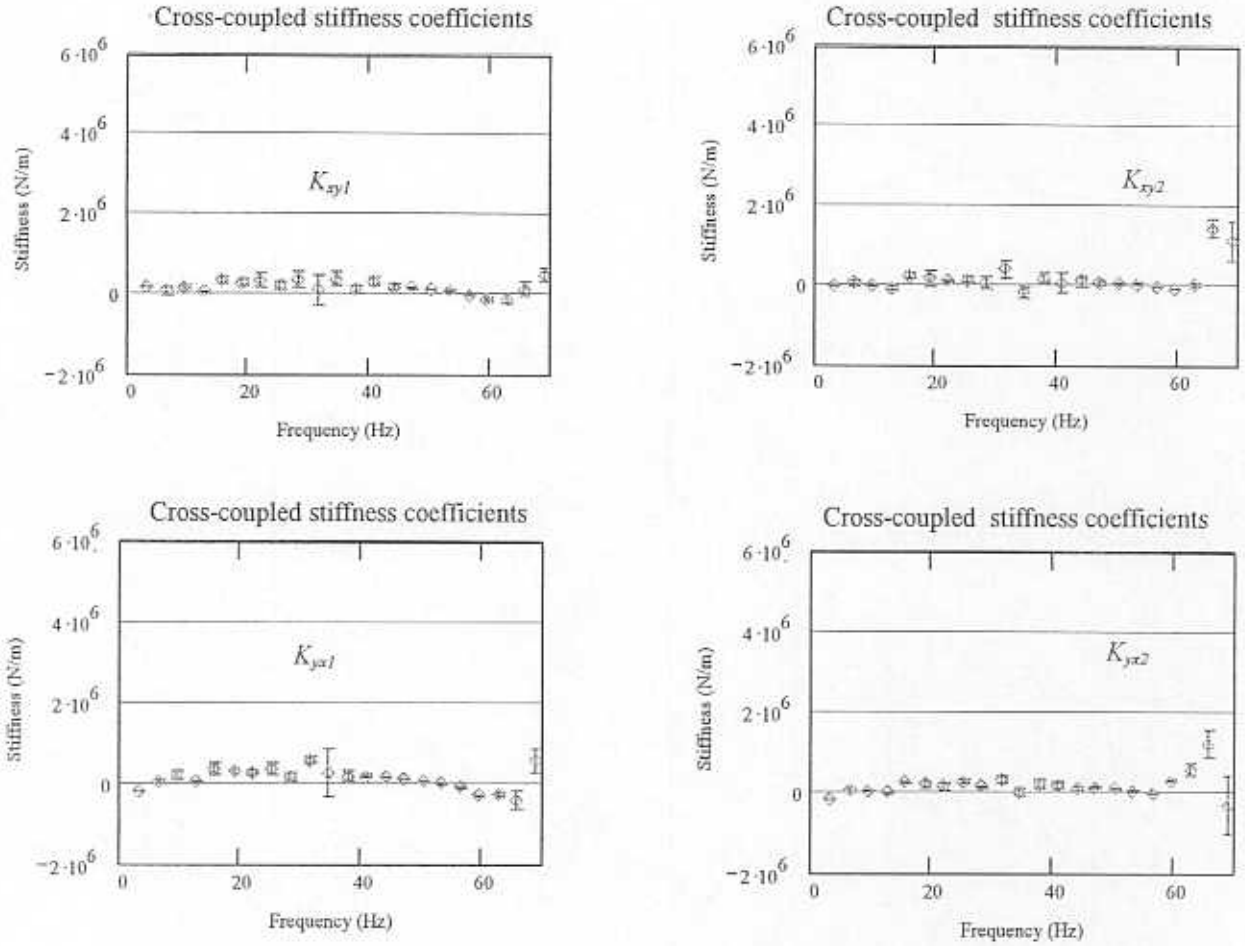

Figure 46c. Average cross-coupled stiffness bearing coefficients identified from impact response measurements as a function of the frequency of excitation and depicting the 95% confidence interval. Rotor speed: 2,000 rpm. (continued)

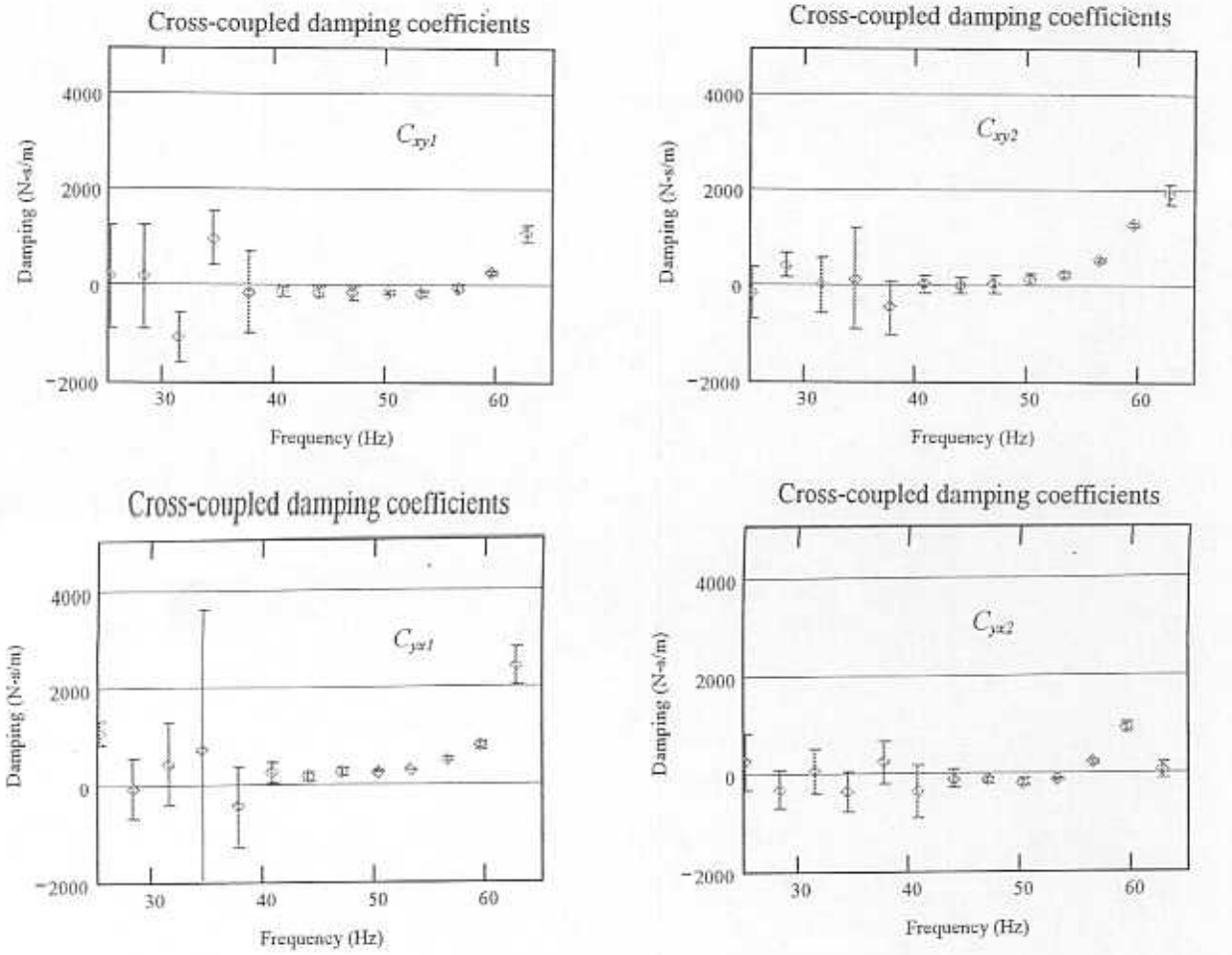

Figure 46d. Average cross-coupled damping bearing coefficients identified from impact response measurements as a function of the frequency of excitation and depicting the 95% confidence interval. Rotor speed: 2,000 rpm. (continued)

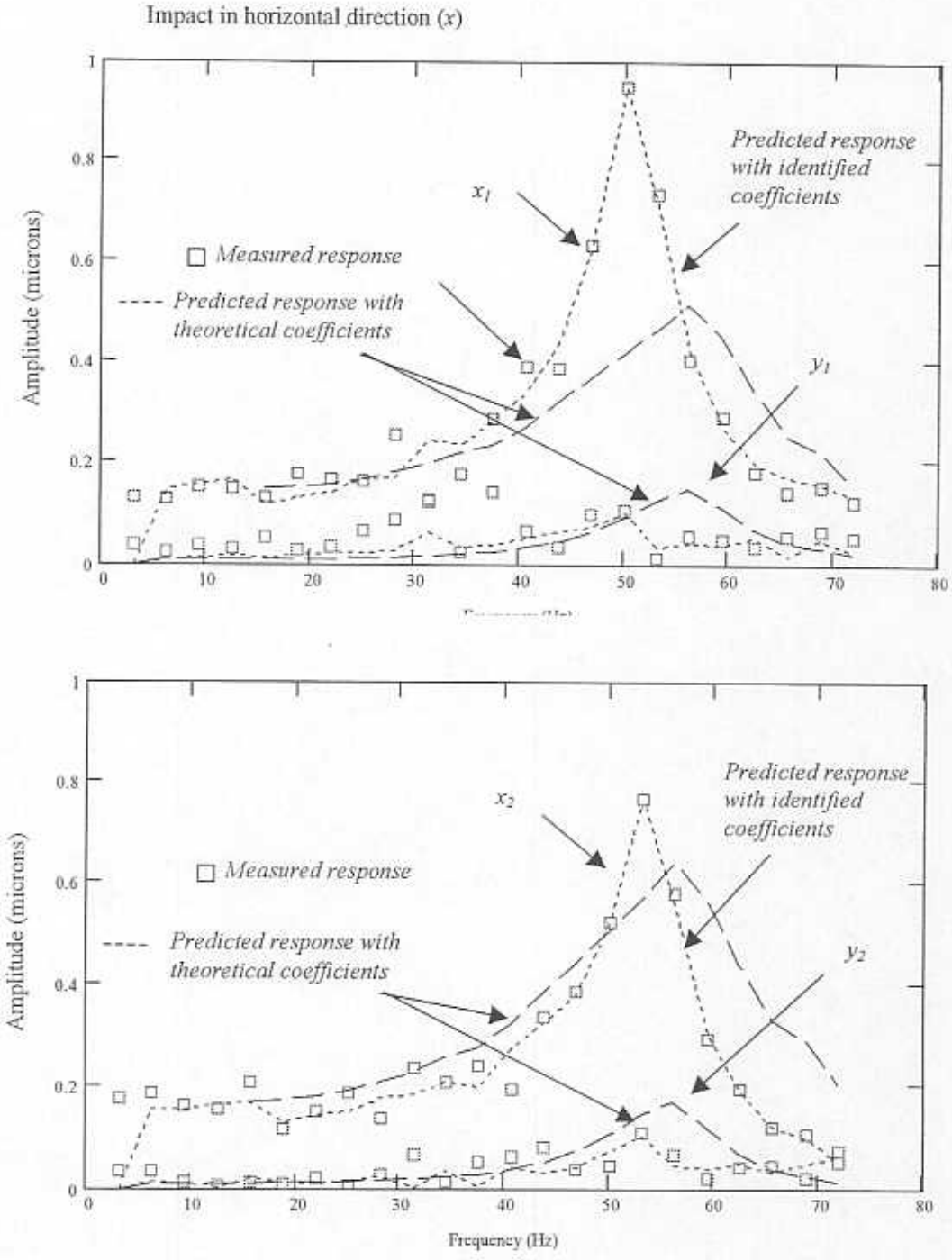

Figure 47. Comparison between measured and predicted rotor response amplitudes at bearing locations. Predictions based on identified and predicted parameters and experimental applied forces.

Impact in vertical direction (y)

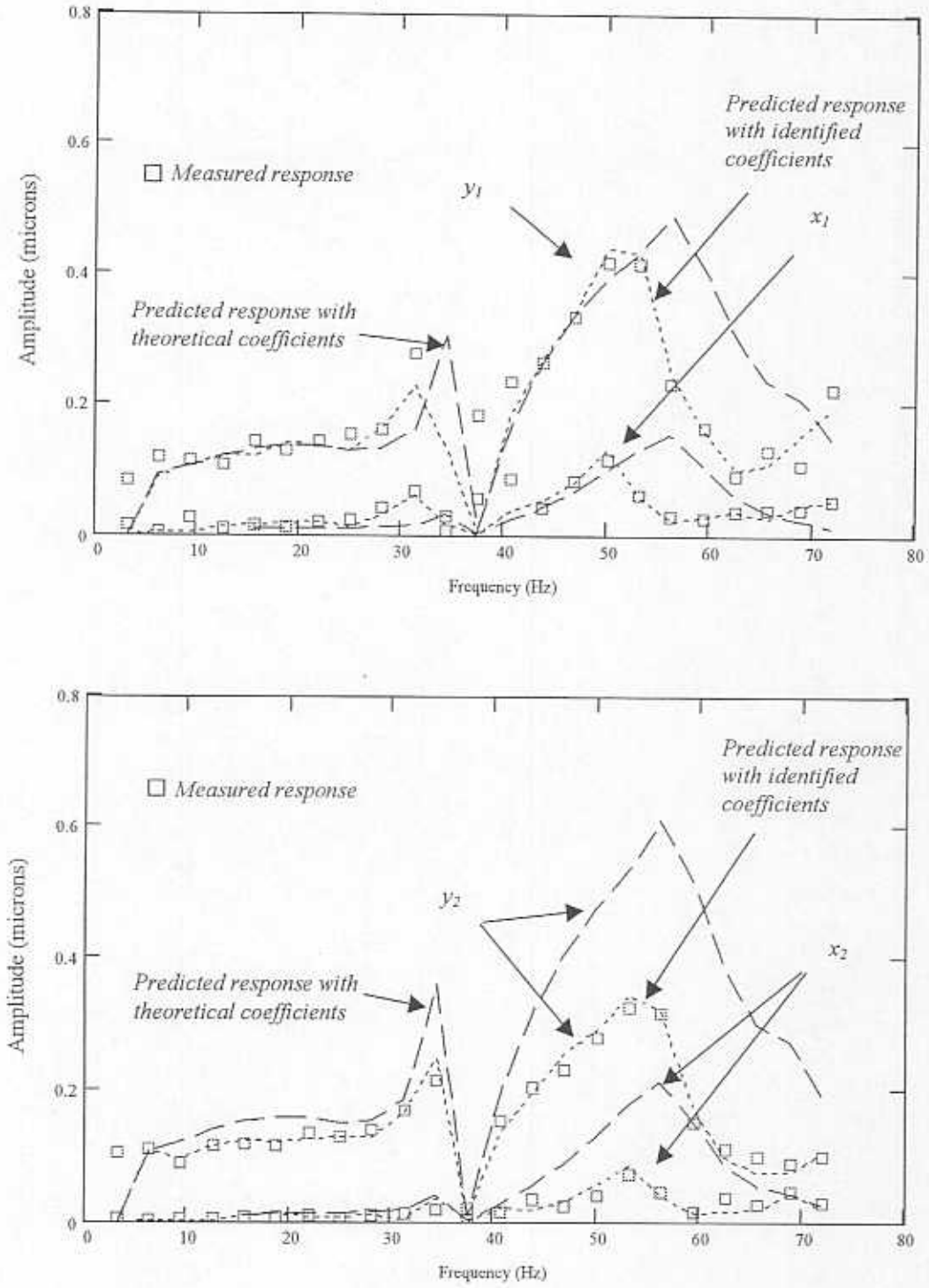

Figure 47b. Comparison between measured and predicted rotor response amplitudes at bearing locations. Predictions based on identified and predicted parameters and experimental applied forces (continued).

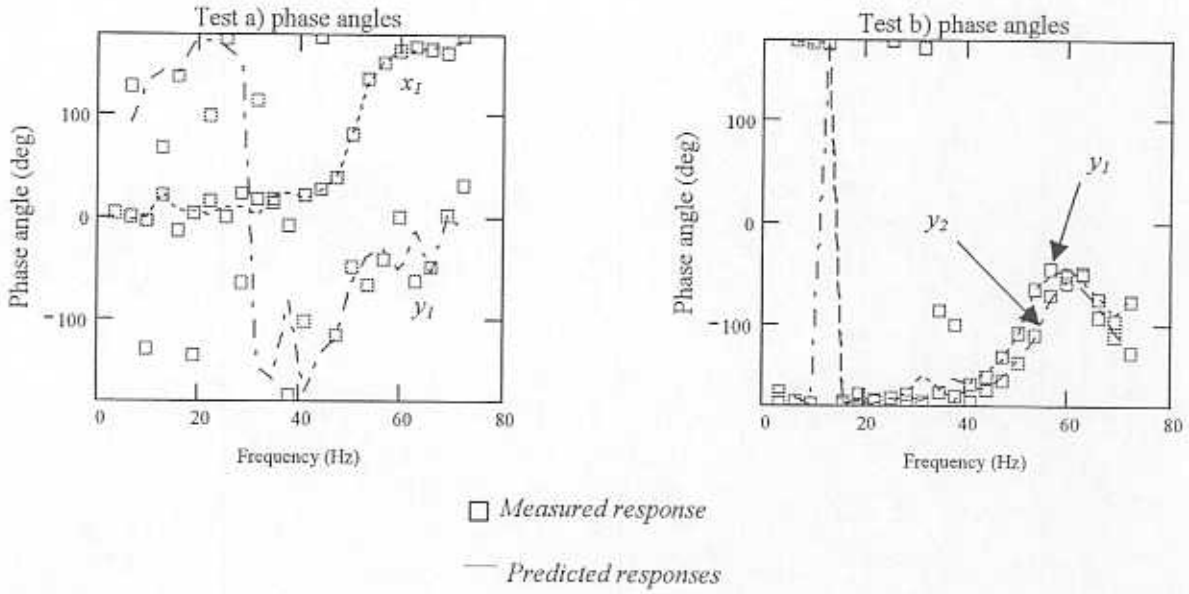

Figure 48. Comparison between measured and predicted phase angles of rotor response at several locations. Predictions based on identified parameters and experimental applied forces.

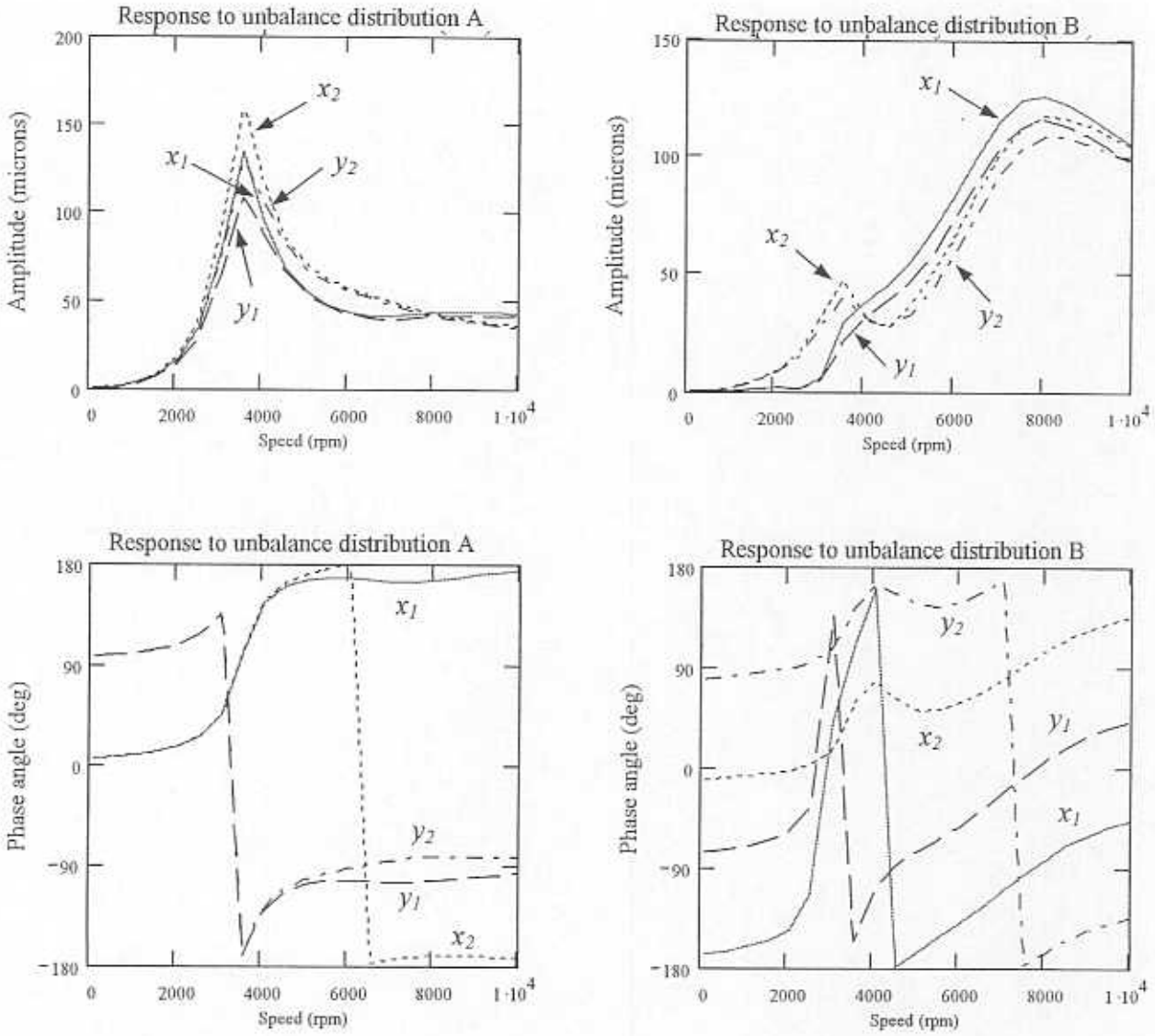

Figure 49. Numerical predictions of rotor synchronous response for two unbalance distributions (*A*,*B*).

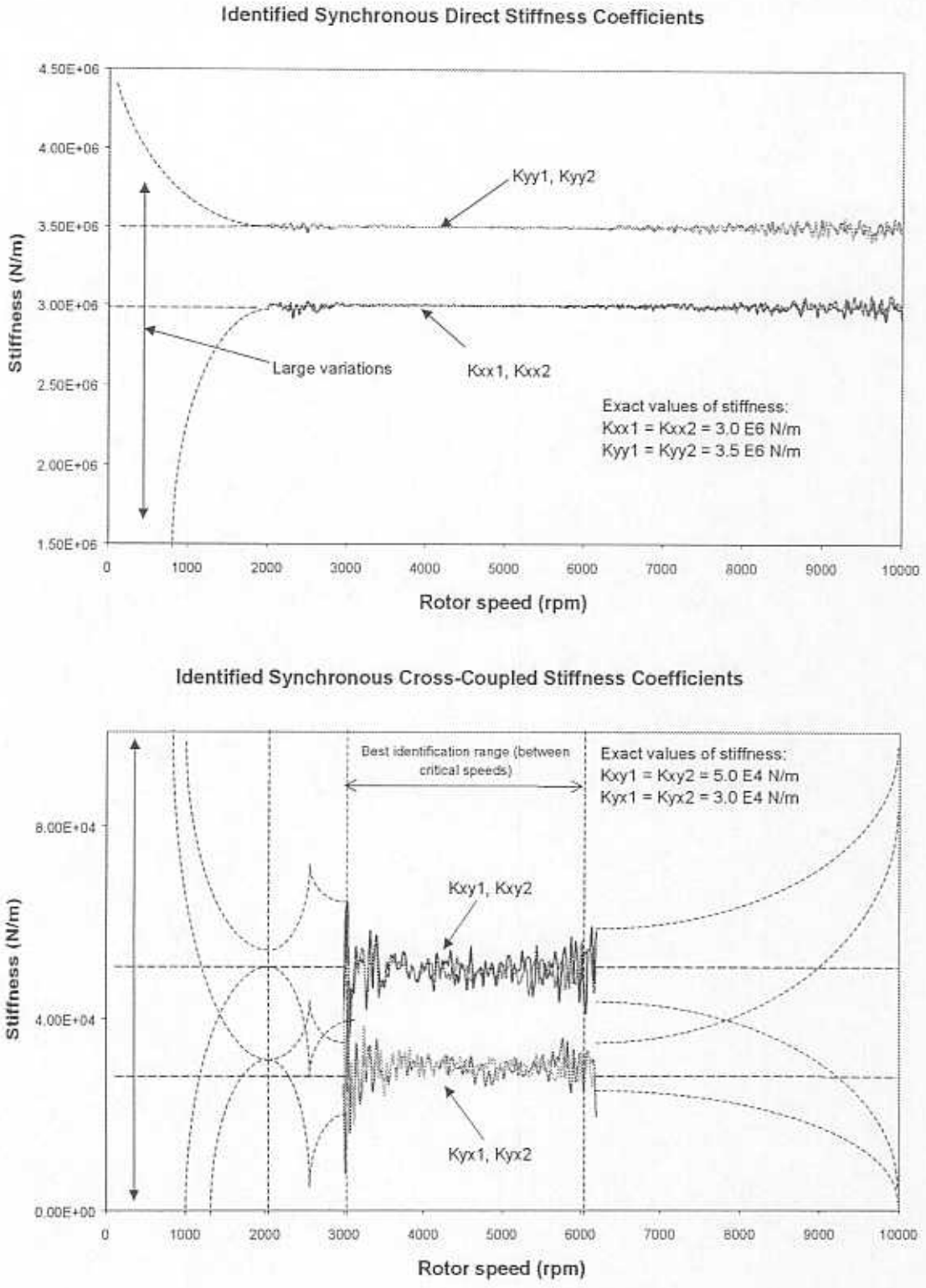

Figure 50a. Identified synchronous rotordynamic force coefficients from imbalance response. Parameters from numerical experiment. Stiffness coefficients.

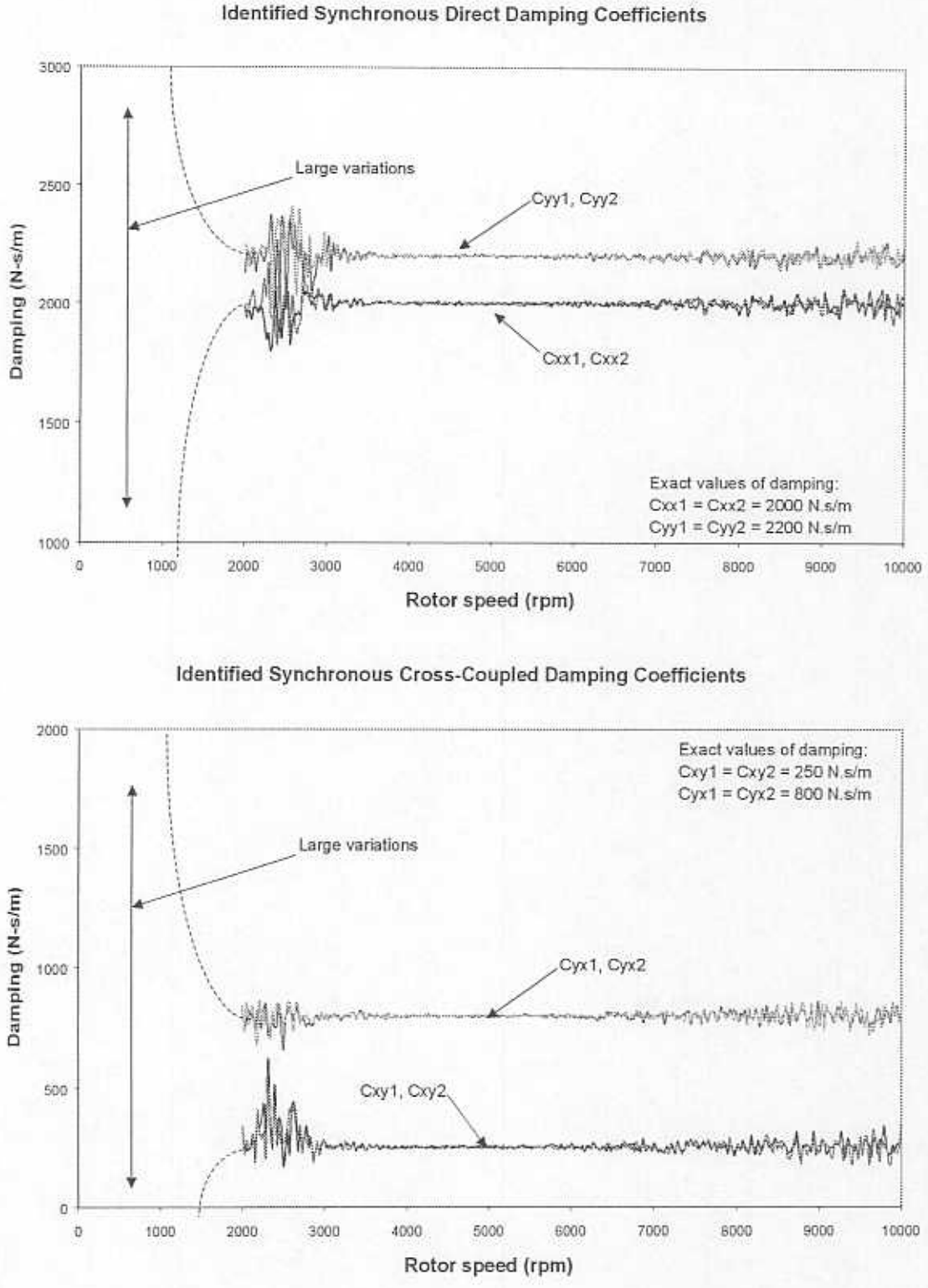

Figure 50b. Identified synchronous rotordynamic force coefficients from imbalance response. Parameters from numerical experiment. Damping coefficients.

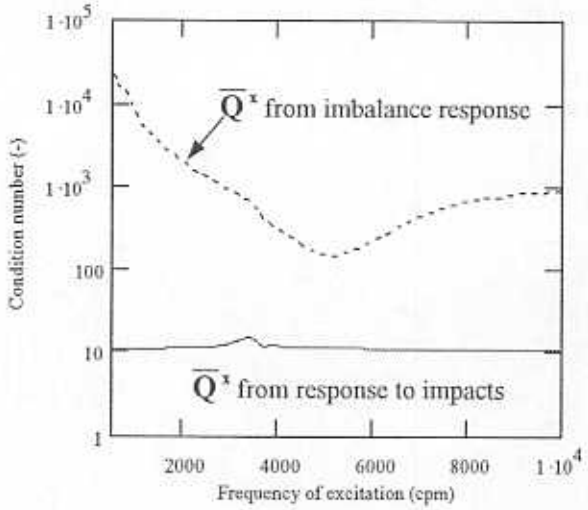

Figure 51. Comparison of condition number of response matrix $\overline{Q}^x$ for two identification methods (from numerical examples).

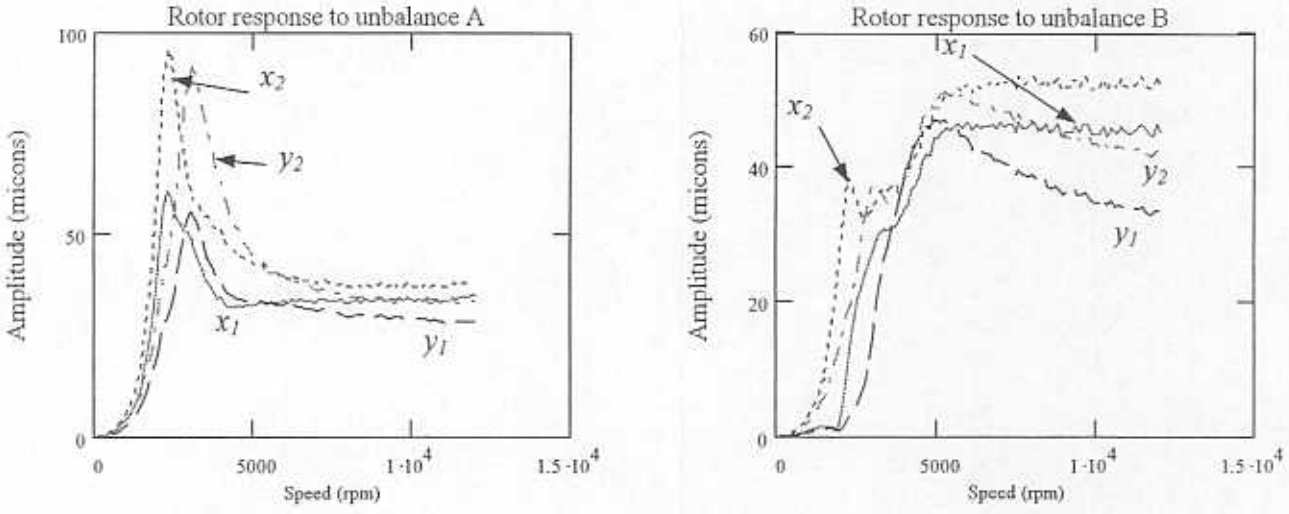

Figure 52. Predicted response to imbalance of test rotor. Calculations performed with speed-dependent bearing dynamic force coefficients. 2% random noise.

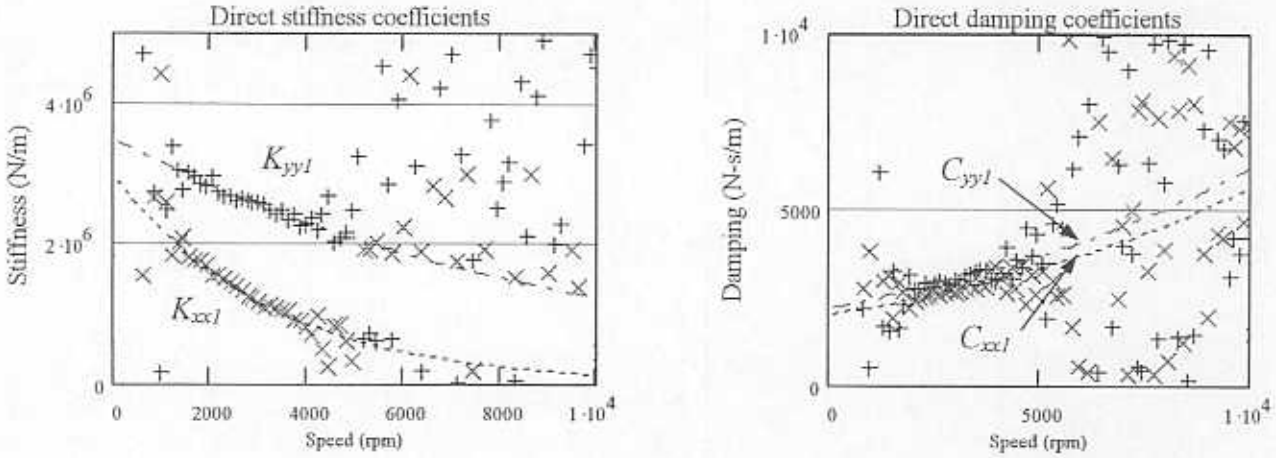

Figure 53. Identification of speed dependent bearing coefficients from numerical example, using rotor responses affected by 2% noise.

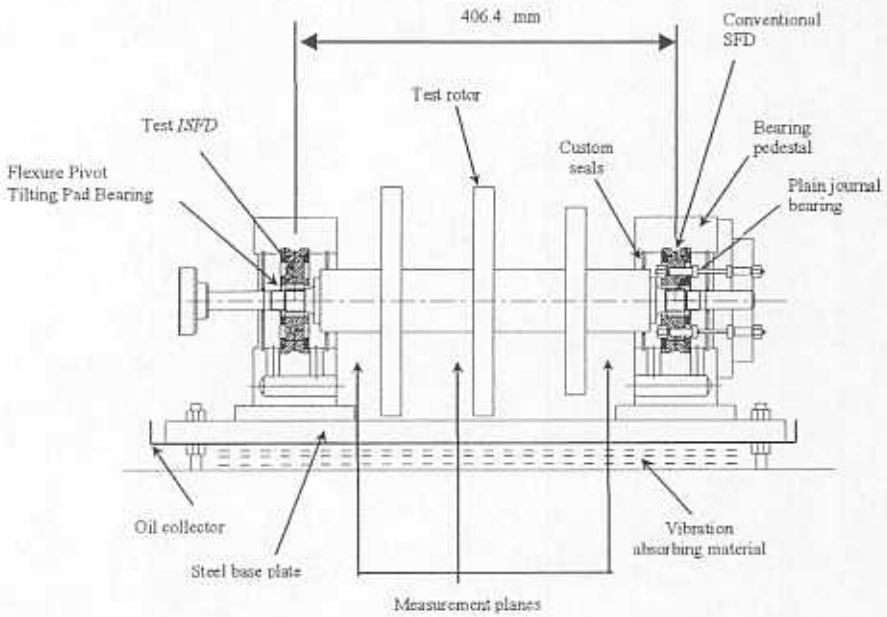

Figure 54. Test rig for measurements of imbalance response of rotor supported on hydrodynamic bearings and squeeze film dampers.

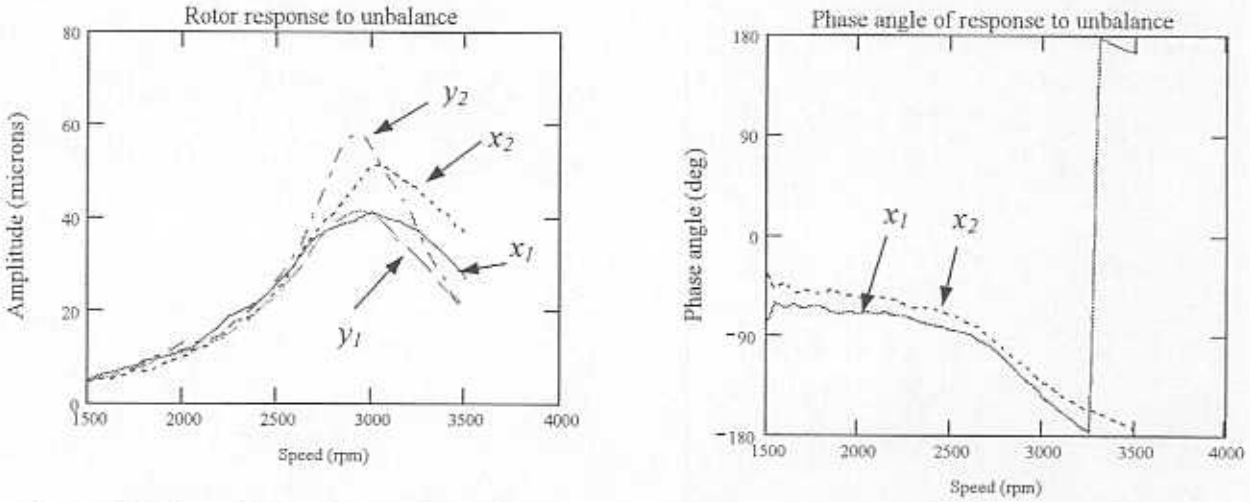

Figure 55. Experimental response of test rotor to calibrated imbalance masses. Imbalance distribution: 3.3 g at location 1 (30°) and 3.2 g at location 2 (at 30°).

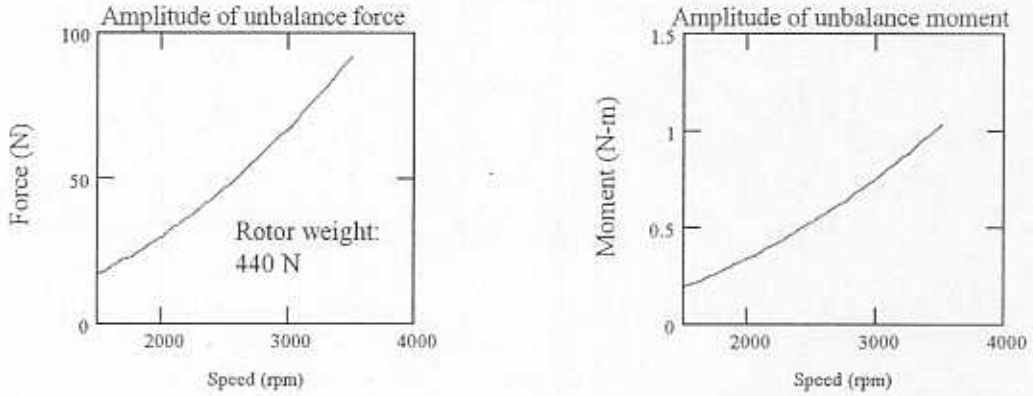

Figure 56. Estimated dynamic forces and moments applied to the rotor CG by the imbalance masses.

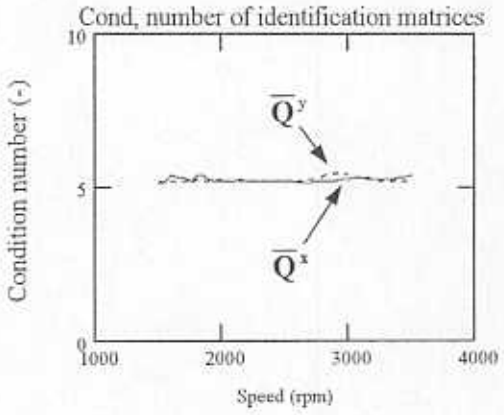

Figure 57. Condition number of response matrices $\overline{Q}^x$ and $\overline{Q}^y$ with experimental amplitudes.

a) Free end: cylindrical bearing with a full cylindrical damper

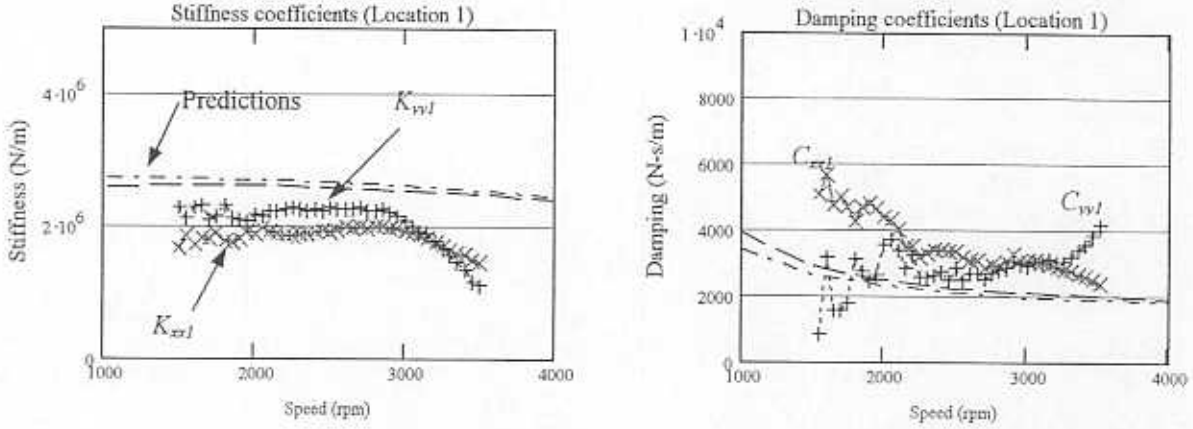

b) Drive end: tilting pad bearing with an integral squeeze film damper

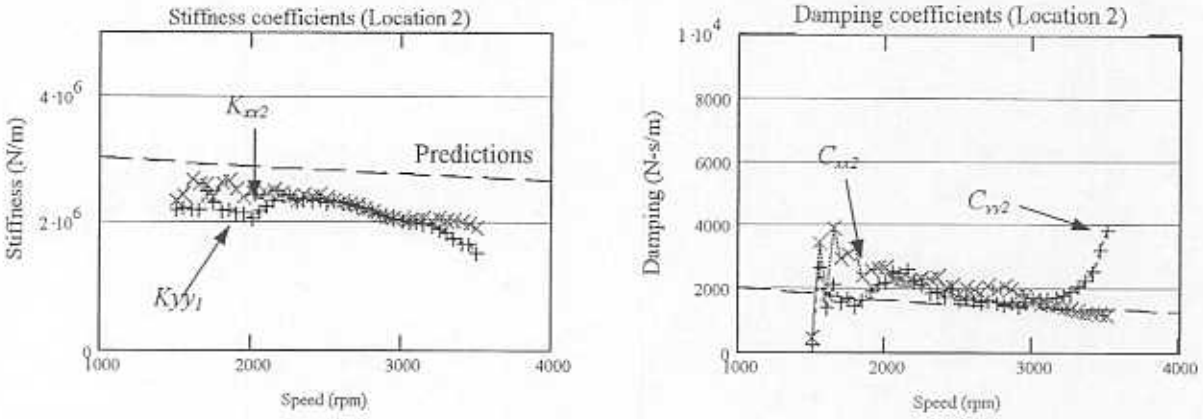

Figure 58. Equivalent, synchronous force coefficients of test series damper-bearing support identified from imbalance response measurements.

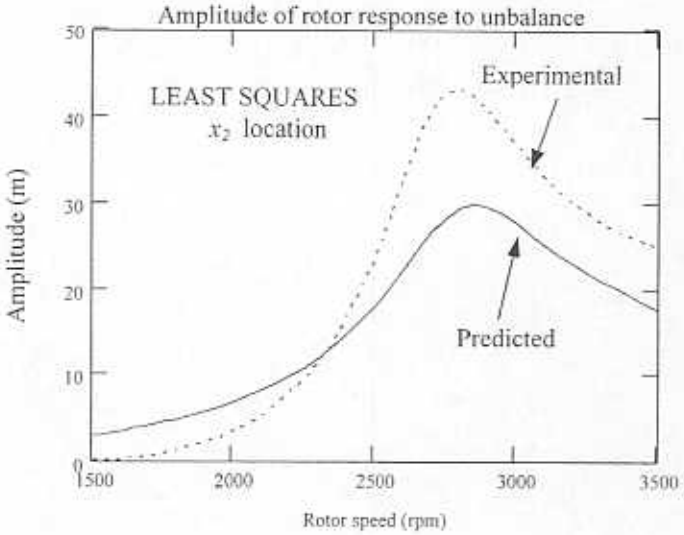

Figure 59. Comparison of experimental and predicted rotor response to imbalance. Predictions based on identified parameters with the least squares method.

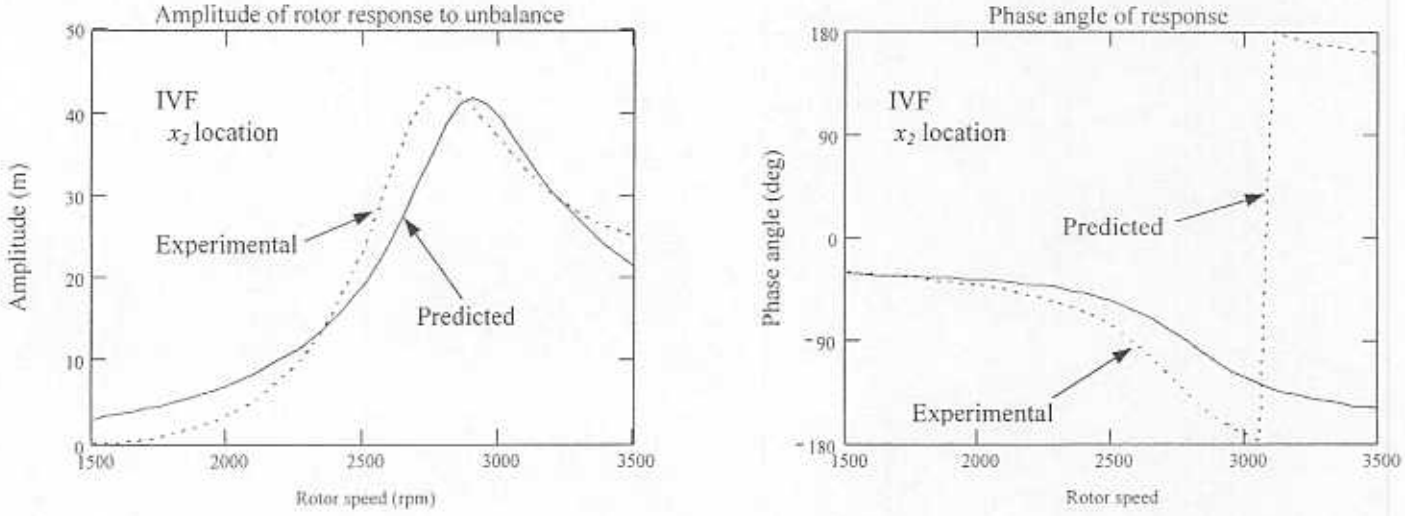

Figure 60. Comparison of experimental and predicted rotor response to imbalance. Predictions based on identified parameters with the instrumental variable filter.

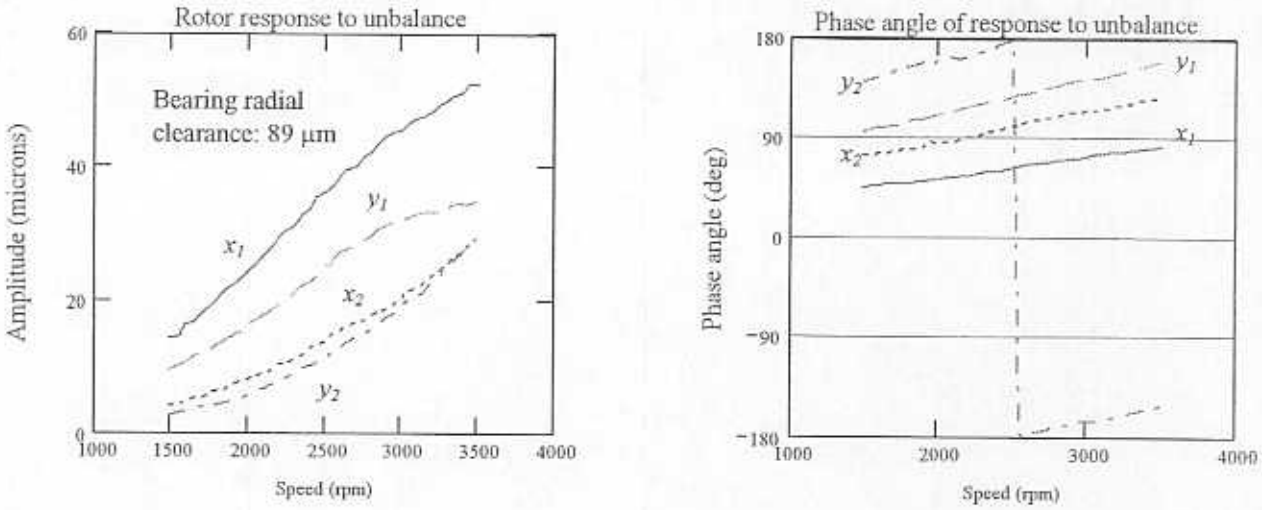

Figure 61. Imbalance response measurement of test rotor supported on two-lobe bearings. Imbalance mass: 10.6 g at 0° at drive end disk (r= 0.070 m).

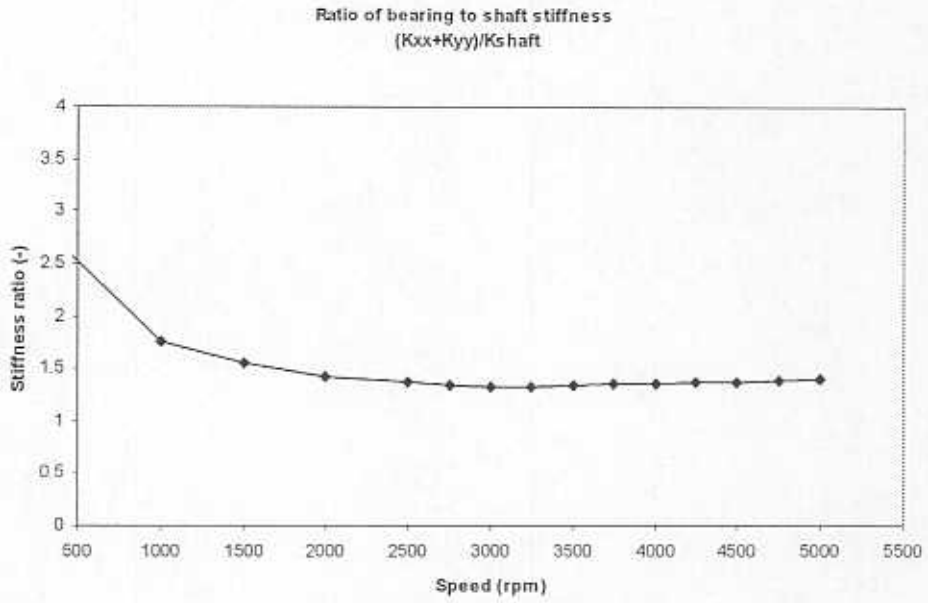

Figure 62. Ratio of bearing to shaft stiffness of test rotor supported on identical two-lobe bearings.

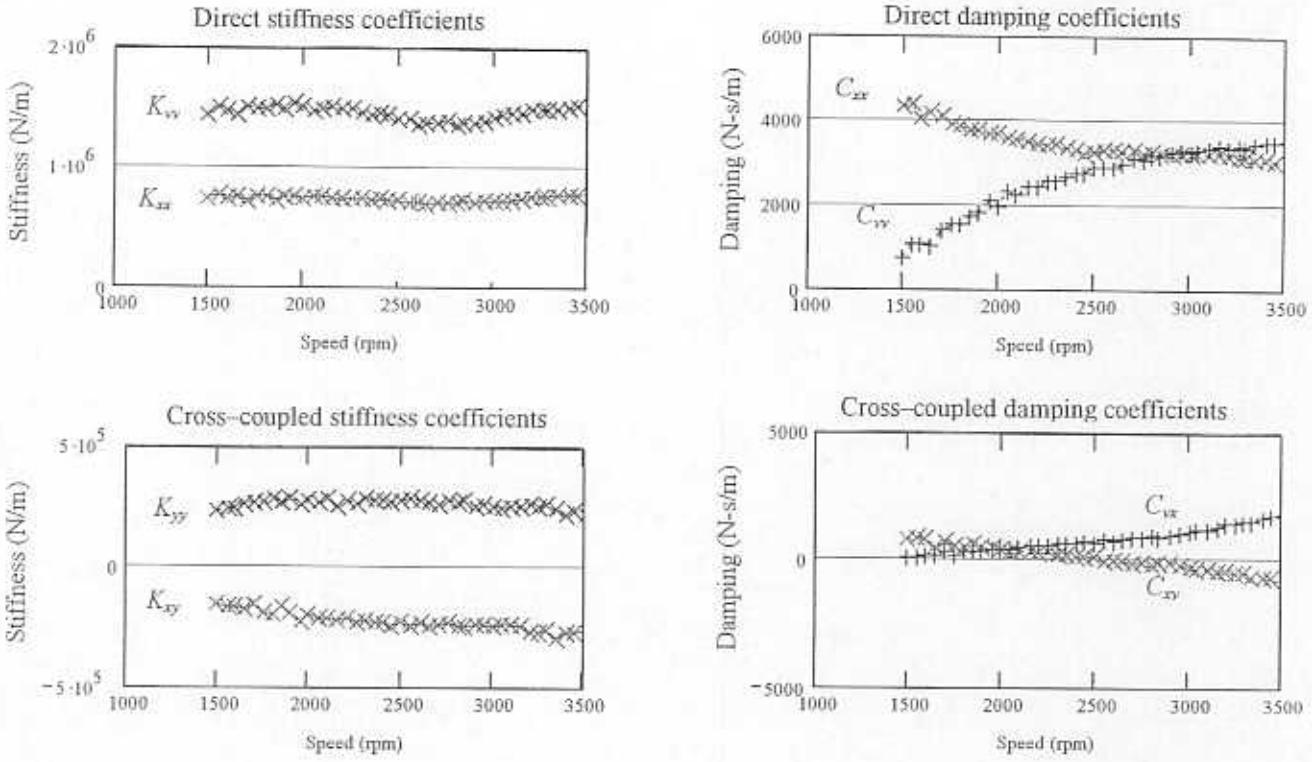

Figure 63. Identified bearing coefficients of two-lobe bearings from rotor response to unbalance.

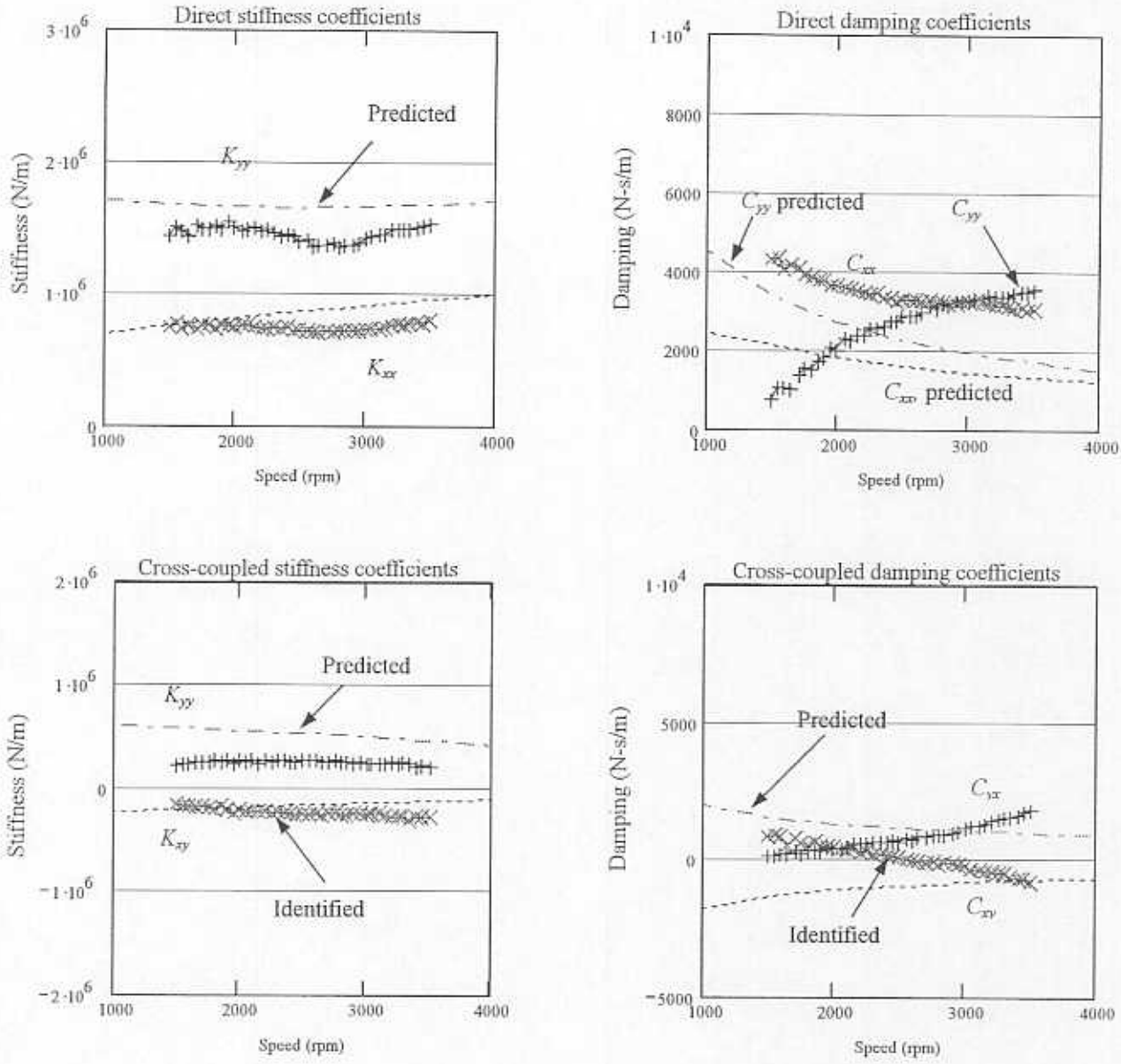

Figure 64. Comparison of predicted and identified force coefficient of two-lobe bearings. Identification based on measurements of rotor unbalance response. Predictions include effect of shaft flexibility.

APPENDIX A.
Data acquisition program (zonic 7000 series) for impact response measurements

```
1.000 ! itest2.BAT
2.000 ! Batch file to perform impact tests on NSF-SFD Rig
3.000 !
4.000 ! Last Modified by fernando romero      3/2/2001
5.000 !              choclo@tamu.edu
6.000 !
7.000 ! **** Initialize acquisition parameters ****
8.000 !
9.000 tpage                    !clear display
9.100 out " "
9.115 out " "
9.130 out " "
9.140 out " "
10.000 i1=0                      !set test counter to zero
11.000 f1=5000                   !(sampling freq)/2.56
12.000 fsv,all,auto              !set FSV for all channels to automatic
13.000 blocksize,4096            !set sampling block size
14.000 iactivate,1:6             !activate channels 1 thru 6
15.000 ifrc,i,f1                 !set sampling frequency
16.000 iacc,trig                 !set acquis. mode to trigger
17.000 tcond, 1, +, 5  !trigger cond. on ch.1 positive slope and 5% of fsv 17.000 iselect,1:6
18.000 iselect 1:6
19.000 cc,sel,dc                 !set dc coupling for 1 thru 6
20.000 tdelay,-500
21.000 ! CHANNEL 1   Load Cell Vertical
22.000 fsv,1,10                  !full scale voltage for channel 1 set to 5 Volts.
23.000 label, 1, Load            !data label
24.000 units, 1, EU, lbs         !unit definition
25.000 sens, 1, 20               !Proximitor sensitivity 50 mV/lb -> 20 lb/Volts
26.000 !
27.000 !CHANNEL 2:5   Proximitor 1
28.000 label, 2, DispDrvY        !Displacement on the drive end  Y= vertical
29.000 label, 3, DispDrvX        !Displacement on the drive end  X= horiz.
30.000 label, 4, DispFreeY       !Displacement on the free end   Y
31.000 label, 5, DispFreeX       !Displacemetn on the free end   X
32.000 iselect 2:5               !select channel list for use in next commands
33.000 units, sel, EU, mil       !unit definition
34.000 sens, 2, 4.935            !Proximitor sensitivity .200 V/mil -> 5 mil/Volts.
34.010 sens, 3, 4.935
34.020 sens, 4, 5.027
34.030 sens, 5, 5.027
35.000 !
36.000 !CHANNEL 6   Reference Signal
37.000 label, 6, RefSgn          !data label
38.000 !units, 6, EU,
39.000 !sens, 6, 2               !ref signal
```

```
40.000 !
41.000 !
42.000 window,none                !set no windowing
43.000 !
44.000 input s9 "Enter first five characters for data files:"
45.000 tpage
46.000 out "Hit me!!!  "
47.000 time1.2.3.4.5.6acqd1          !acquire 1 block of data
47.001 out " "
47.005 out "We have saved",i1," tests so far"
47.006 out " "
47.010 out "PLease make a choice"
47.020 out "--------------------"
47.030 out " "
47.040 out " (R) Repeat this test."
47.045 out " (S) Save the data for this test."
47.050 out " (E) Exit this program."
47.100 input s2
47.110 if s2 = r jump 45
48.000 !
49.000 if s2 = s jump 50
49.010 if s2 = e jump 70
50.000 tpage
51.000 out "Saving the data files for test #",i1+1
51.100 incr i1
52.000 s10="load.prn"
53.000 s11="drvy.prn"
54.000 s12="drvx.prn"
55.000 s13="freey.prn"
56.000 s14="freex.prn"
57.000 s15="refsgn.prn"
58.000 s10=s9+i1+s10
59.000 s11=s9+i1+s11
60.000 s12=s9+i1+s12
61.000 s13=s9+i1+s13
62.000 s14=s9+i1+s14
63.000 s15=s9+i1+s15
64.000 savfunct s10 d1 ascii
65.000 savfunct s11 d2 ascii
66.000 savfunct s12 d3 ascii
67.000 savfunct s13 d4 ascii
68.000 savfunct s14 d5 ascii
69.000 savfunct s15 d6 ascii
69.002 out " "
69.100 out "Make another choice:"
69.110 out "--------------------"
69.111 out " "
69.120 out " (R) Run more tests."
69.125 out " (E) Exit."
```

```
69.130 input s3
69.135 if s3 = r jump 45
70.000 tpage
71.000 out "Thank you for running tests with me, it was fun!"
72.000 end
```

Appendix B. Equivalent impedance of series support squeeze film damper and flexure pivot tilting pad bearing.

The series support *ISFD-FPJB* has equivalent stiffness and damping force coefficients that are dependent on the running speed and on the frequency of excitation. Furthermore, the attachment mass between the two fluid films corresponding to the damper journal and flexure pivot bearing masses (m) introduces a reduction in the equivalent dynamic stiffness at high frequencies. Figure B1 shows a diagram of a point mass rotor supported on two fluid films in series, as well as the coordinate system.

The equations of motion of the point mass rotor and the attachment mass are:

$$\mathbf{M}\ddot{\mathbf{X}}_S + \mathbf{K}(\mathbf{X}_S - \mathbf{X}_D) + \mathbf{C}(\dot{\mathbf{X}}_S - \dot{\mathbf{X}}_D) = \mathbf{F} \tag{B.1}$$

$$\mathbf{M}_D\ddot{\mathbf{X}}_D + \mathbf{K}_D\mathbf{X}_D + \mathbf{C}_D\dot{\mathbf{X}}_D - \mathbf{K}(\mathbf{X}_S - \mathbf{X}_D) - \mathbf{C}(\dot{\mathbf{X}}_S - \dot{\mathbf{X}}_D) = \bar{\mathbf{0}} \tag{B.2}$$

where:

$$\mathbf{M} = \begin{bmatrix} M & 0 \\ 0 & M \end{bmatrix},\ \mathbf{K} = \begin{bmatrix} K_{xx} & K_{xy} \\ K_{yx} & K_{yy} \end{bmatrix},\ \mathbf{C} = \begin{bmatrix} C_{xx} & C_{xy} \\ C_{yx} & C_{yy} \end{bmatrix} \tag{B.3a}$$

$$\mathbf{M}_D = \begin{bmatrix} m & 0 \\ 0 & m \end{bmatrix},\ \mathbf{K}_D = \begin{bmatrix} K_x & 0 \\ 0 & K_y \end{bmatrix},\ \mathbf{C}_D = \begin{bmatrix} C_x & 0 \\ 0 & C_y \end{bmatrix},\ \mathbf{X}_S = \begin{bmatrix} x_s \\ y_s \end{bmatrix},\ \mathbf{X}_D = \begin{bmatrix} x_d \\ y_d \end{bmatrix} \tag{B.3b}$$

and

$$\mathbf{F} = \begin{bmatrix} F_o \\ -jF_o \end{bmatrix} e^{j\omega t},\ F_o = cte,\ \bar{\mathbf{0}} = \begin{bmatrix} 0 \\ 0 \end{bmatrix} \tag{B.3c}$$

Assume a harmonic solution of the form:

$$\mathbf{X}_S = \chi_S\, e^{j\omega t} \text{ and } \mathbf{X}_D = \chi_D\, e^{j\omega t} \tag{B.4}$$

and define the bearing and damper impedance functions as:

$$\mathbf{Z}_B = \mathbf{K} + j\omega\mathbf{C} \tag{B.5a}$$

$$\mathbf{Z}_D = (\mathbf{K}_D - \omega^2\mathbf{M}_D) + j\omega\mathbf{C}_D \tag{B.5c}$$

Combining equations (B.1) and (B.2), the equivalent bearing impedance is given by:

$$\mathbf{Z}_{eq} = \left[\mathbf{Z}_B - \mathbf{Z}_B(\mathbf{Z}_B + \mathbf{Z}_D)^{-1}\mathbf{Z}_B\right] \tag{B.7}$$

$\mathbf{Z}_{eq}$ is a 2x2 square matrix whose entries are the equivalent bearing impedances:

$$\mathbf{Z}_{eq} = \begin{bmatrix} Z_{eq_{xx}} & Z_{eq_{xy}} \\ Z_{eq_{yx}} & Z_{eq_{yy}} \end{bmatrix} \tag{B.8}$$

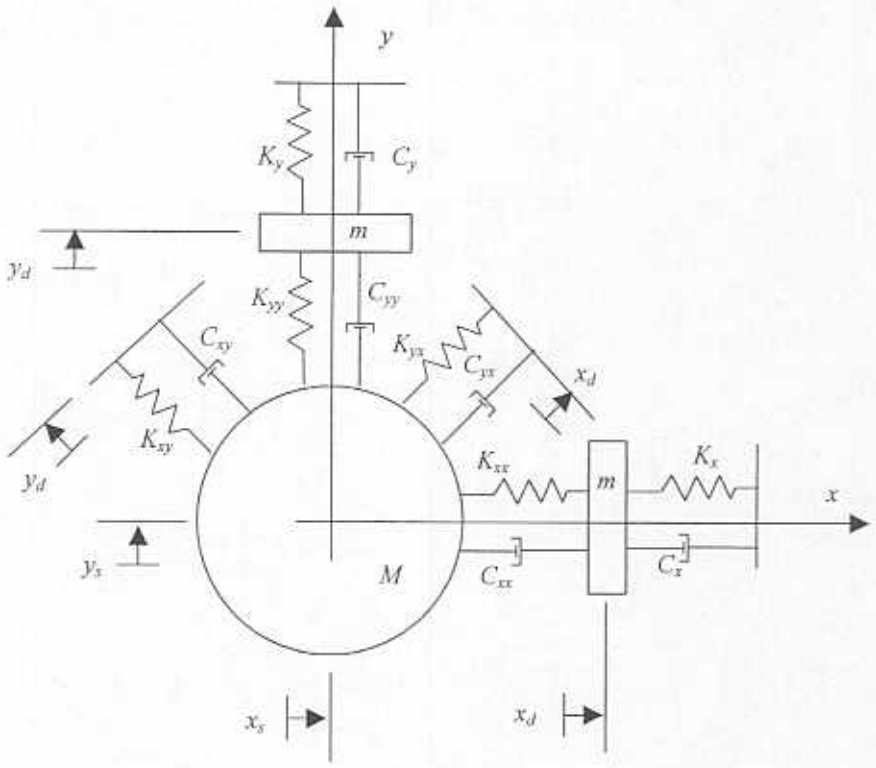

Figure B1. Representation of a point mass rotor supported on a series combination of a fluid film bearing (eight rotordynamic force coefficients) and a squeeze film damper (four dynamic force coefficients). Attachment mass included.